Development of MXenes-based Electrodes for Flexible Energy Storage Applications

PhD Thesis

Submitted By: Muniba Ahmad

Registration No. 18-FET-PhDEE/F18

Supervisor: Prof. Dr. Ahmed Shuja Syed

A dissertation submitted to I.I.U. in partial fulfillment of the requirements for the degree of

DOCTOR OF PHILOSOPHY

Department of Electrical and Computer Engineering

Faculty of Engineering and Technology

International Islamic University,

Islamabad

2025

CERTIFICATE OF APPROVAL

Title of Thesis: Development of MXenes-based Electrodes for Flexible Energy Storage Applications

Name of Student: Muniba Ahmad

Registration No: 18-FET-PhDEE/F18

Accepted by the Department of Electrical and Computer Engineering, Faculty of Engineering and Technology, International Islamic University (IIU), Islamabad, in partial fulfillment of the requirements for the Doctor of Philosophy degree in Electrical Engineering.

Viva voce committee:

Prof. Dr. Ahmed Shuja Syed (Supervisor)

Professor, DECE, FET, IIUI.
VP R & E/Founding Executive Director CAEPE

Dr. Gul Hassan (Internal)

Associate Professor, DECE, CAEPE, FET, IIUI

Dr. Hafiz Muhammad Faisal Zafar (External-I)

Deputy Chief Scientist, PAEC, Islamabad

Dr. Muhammad Osama Ali (External-II)

Assistant Professor, College of E&ME, NUST, Islamabad.

Dr. Ihsan-ul-Haq (Chairman, DECE)

Associate Professor, DECE, FET, IIU Islamabad.

Prof. Dr. Muhammad Amir (Dean, FET)

Professor, DECE, FET, IIU Islamabad.

This thesis is dedicated to my beloved family and esteemed teachers.

Abstract

MXene-based materials show great potential as electrodes for next-generation energy storage devices, owing to their excellent conductivity, high surface area, and tunable surface chemistry. In this study, we focus on the design and fabrication of a diverse range of electrodes by systematically changing the composition of MXenes, including pure MXenes, MXene-based composites, and electrodes with controlled levels of MXene impurities. This strategic variation enables a comprehensive investigation of how material composition influences the electrochemical performance of energy storage systems. Through extensive structural, morphological, and electrochemical analysis, we evaluate the impact of MXene composition on charge storage capacity, cyclic stability, and rate capability. Electrodes with varying Titanium Carbide (MXene-enabled Impurity) content were synthesized, and symmetric supercapacitors were fabricated using three innovative gel-based electrolytes: Acrylamide, *N, N′*-Dimethylacrylamide, and 2-Hydroxyethyl methacrylate. X-ray diffraction (XRD) analyzed the structural properties of the electrodes, while cyclic voltammetry (CV) assessed their electrochemical performance within a -1 V to 1 V range at varying scan rates. Electrochemical impedance spectroscopy (EIS) was conducted to analyze the Randles circuit and determine the series resistance (Rs), providing insight into the active surface area contributing to charge storage. Additional tests, including open- and short-circuit evaluations performed after charging at 1V for 2 minutes, confirmed the compatibility of the electrodes with different electrolytes. Notably, the maximum specific capacitances of 50 F/g and 79 F/g were achieved with *N*, *N′*-Dimethylacrylamide and 2-Hydroxyethyl methacrylate, respectively. To enhance supercapacitor performance, binary and ternary composites of MXenes with conducting polymers were developed for flexible asymmetric configurations. MXene, MXene-PANI,

and MXene-PANI-PEDOT: PSS acted as cathodes, with pBOA serving as the anode. Supercapacitors based on MXene-PANI-PEDOT: PSS demonstrated enhanced electrochemical performance, achieving a specific capacitance of 279 F/g at a scan rate of 5 mV/s, surpassing the specific capacitances of MXene-PANI (153 F/g) and pristine MXene (68 F/g). Building upon these advancements, a novel quaternary composite of MXene (MXene-pBOA-NiO-rGO) was also developed and deposited onto conductive fiber yarn to fabricate a symmetric supercapacitor with variations in the electrode distance. Electrochemical testing using a two-electrode system revealed exceptional supercapacitive behavior, yielding a specific capacitance of 338.4 F/g and an energy density of 16.9 Wh/kg in an Acrylamide-based gel electrolyte. These results demonstrate the potential of MXene-based electrodes for flexible, high-performance supercapacitors in wearable and self-powered systems.

List of Publications

The research work presented in this dissertation is based on the following publications.

1 Muniba Ahmad, Ahmed Shuja, Muhammad Ali, Fatima Sajid, Saba Ashraf (2024). Development of MXene-enabled Titanium Carbide (TiC) Impurity-Based Electrodes for the Fabrication and Circuit-Level Testing of Gel-Based Supercapacitors. **International Journal of Energy Research**. Volume 2024, Issue 1 https://doi.org/10.1155/2024/9229089

2 Muniba Ahmad, Ahmed Shuja, Imran Murtaza, Shah Fahad, Muhammad Shahid Khan. Synergistic Integration of MXenes with Conducting Polymers to Enhance the Specific Capacitance of Asymmetric Supercapacitors. **Journal of Materials Science: Materials in Electronics** vol. 36, no. 18, pp. 1–16, Jun. 2025, doi: 10.1007/S10854-025-15164-5/METRICS.

3 Muniba Ahmad, Ahmed Shuja, Imran Murtaza, Shah Fahad, Muhammad Shahid Khan. Elevating Wearable Tech by Exploring MXene-NiO-pBOA-rGO: A Quaternary Composite for Enhanced Energy Storage in Symmetric Supercapacitors. **International Journal of Ionics – The Science and Technology of Ionic Motion**. Vol. 36, No. 18, pp. 1–16, Jun. 2025, doi: 10.1007/S10854-025-15164-5/METRICS.

ACKNOWLEDGMENTS

In the name of Allah, the Most Gracious and Most Merciful. I am sincerely thankful to Allah for providing me with the strength and determination to complete this research. May peace and blessings be upon the Last Prophet, Muhammad (PBUH), and his companions, who dedicated their lives to spreading the message of Islam and the quest for knowledge.

I am deeply grateful to my supervisor, Prof. Dr. Ahmed Shuja Syed, whose inspiration, ideas, and relentless efforts have allowed me to pursue and complete my higher education. His strong commitment to teaching, research, and personal integrity is a remarkable example for me and many others. I also want to sincerely thank Research Associates Shah Fahad, Muhammad Ali, Shoaib Alam, and the entire support staff at the Centre of Advanced Electronics and Photovoltaics Engineering for their consistent support and insightful discussions over the years. Additionally, I am very thankful to the International Islamic University Islamabad, Pakistan, for providing me with a full tuition waiver throughout my PhD journey.

I am truly grateful to my parents for their ongoing prayers and support. Words cannot fully express my appreciation for the exceptional care and encouragement from my spouse and children. Their support has enabled me to pursue and achieve my dreams of earning a PhD.

Engr Muniba Ahmad

TABLE OF CONTENTS

List of Figures

List of Tables

List of Abbreviations

C	Capacitance
SC	Supercapacitor
EDLCs	Electrode Double-Layer Capacitance
CPs	Conducting Polymers
EIS	Electrochemical Impedance Spectroscopy
PEDOT: PSS	Poly (3, 4-ethylene dioxythiophene) polystyrene sulfonate
Ppy	Popolypyrrole
SSC	Symmetric supercapacitor
ASC	Asymmetric supercapacitor
CV	Cyclic voltammetry
GCD	Galvanostatic Charge -Discharge
rGO	Reduced Graphene Oxide
NiO	Nickel Oxide
2D	Two Dimensional
SEM	Scanning Electron Microscopy
XRD	X-ray Diffraction
TiC	Titanium Carbide
NMP	N-methyl pyrrolidone
PVA	polyvinyl alcohol
pBOA	Poly (benzoxazole aniline)

Chapter 1 Introduction

This section introduces core concepts of energy storage technologies. It highlights progress in analyzing MXene-based supercapacitors, which are regarded as a potential leading candidate for advanced energy storage solutions.

1.1 Energy Storage Systems

Energy serves as the cornerstone of economic growth, social advancement, and ecological protection. Developed and developing nations depend on energy to power their industries, transportation systems, healthcare systems, and daily household activities. Its availability and efficient utilization influence the quality of life, productivity, and environmental sustainability. Energy storage systems are essential in energy infrastructure, as they optimize power generated from diverse sources, especially renewable energy resources [1-4]. Energy storage systems, which include various technologies such as fuel cells, batteries, and capacitors, have been developing due to ongoing research and innovation [5-8]. The sustainable management of energy resources, together with advancements in state-of-the-art energy storage technologies, is essential for maintaining ecological balance, promoting social development, and securing long-term economic stability [9-12]. Figure 1.1 presents a structured organogram that categorizes various energy storage technologies into five primary groups: mechanical-based energy storage techniques, electrochemical energy storage systems, chemical energy storage technologies, electrical energy storage devices, and thermal-based energy storage methods. Each category includes different storage methods based on their working principles and applications.

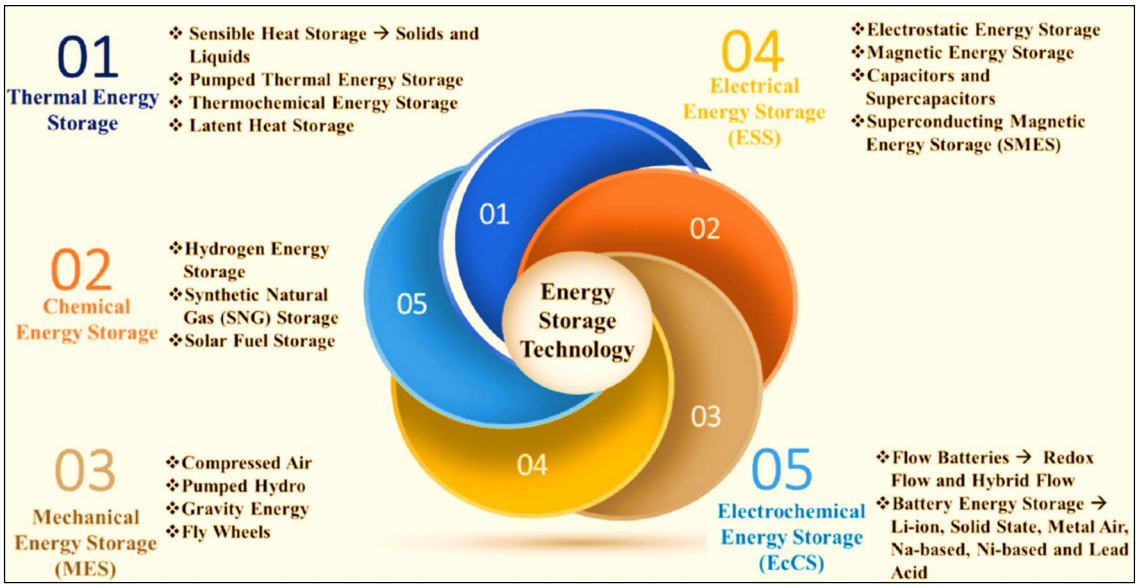

Figure 1.1 Organogram of energy storage technologies [13]

Energy conversion devices, such as fuel cells and solar cells, are on the rise, converting energy into electricity. Meanwhile, innovative energy storage devices, such as batteries and capacitors, are improving to efficiently store and deliver electricity. These advancements are laying the groundwork for cutting-edge energy systems that drive the global transition to sustainability and efficiency. Fuel cells are electrochemical devices that convert the chemical energy of a fuel (typically hydrogen) and an oxidizing agent (usually oxygen) directly into electricity, water, and heat. Solar cells, also known as photovoltaic (PV) cells, convert sunlight directly into electricity using semiconductor materials [14]. Batteries and capacitors are energy storage devices with different operating principles and applications. Batteries are often chosen for applications that need high energy density and long-term energy supply, but they are limited by low power output. In contrast, capacitors are suitable for quick energy discharge at high power. No individual technology is capable of delivering both high energy and power density simultaneously. This limitation has led to extensive research into advanced energy storage solutions, especially electrochemical capacitors,

known as supercapacitors [15]. Figure 1.2 illustrates a Ragone plot that compares different energy storage systems by inspecting their energy and power density characteristics [16]. The graph highlights the relationship between energy density and power density for various energy storage technologies. Figure 1.3 shows a comparison of the key properties of batteries and supercapacitors, highlighting their differences due to energy storage mechanisms.

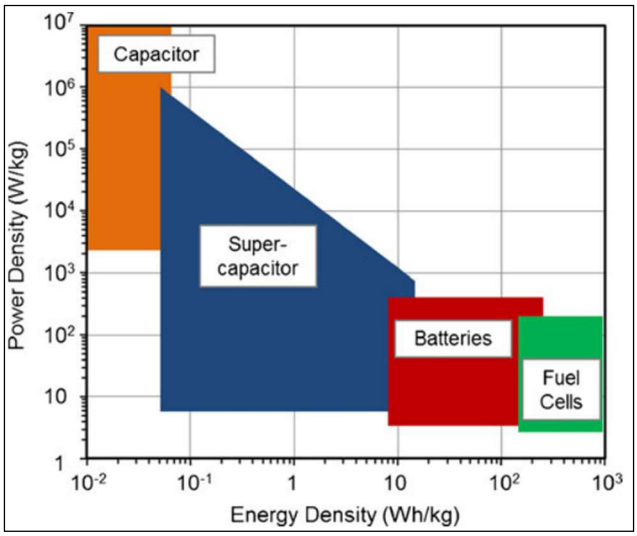

Figure 1.2 Comparison of different energy storage technologies using a Ragone chart [16]

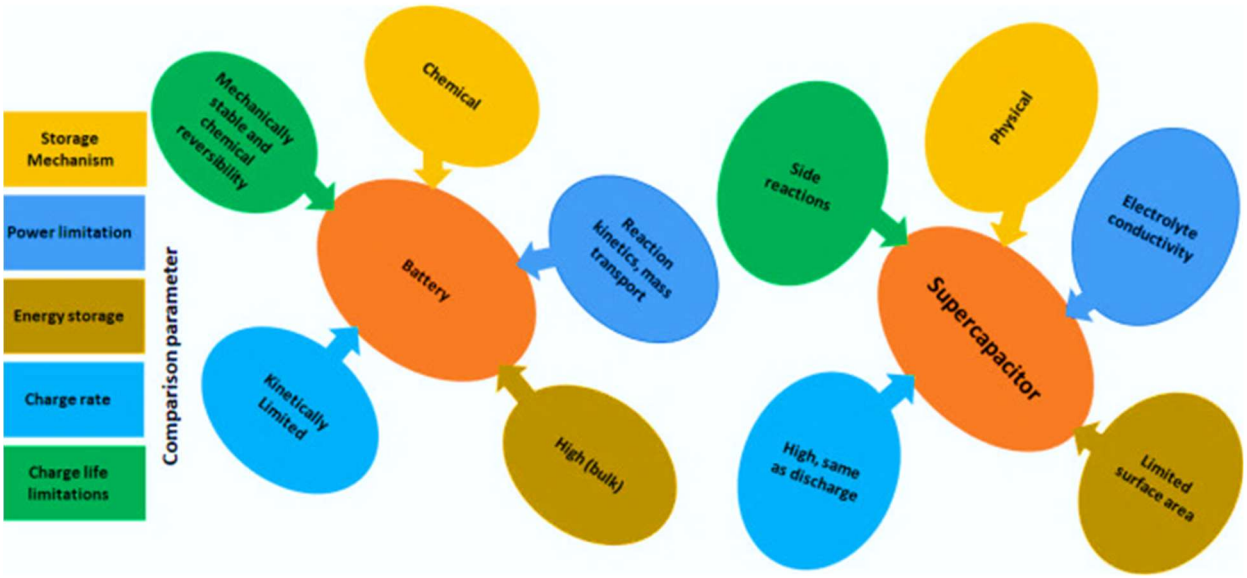

Figure 1.3 Comparison of Batteries and Supercapacitors [17,18]

1.2 Supercapacitors

Supercapacitors, also called ultracapacitors, show a significant advancement in energy storage technologies, addressing the growing global energy demands [19]. Unlike traditional batteries that generate energy via chemical reactions, supercapacitors store and release energy through electrostatic charge separation between the interface of electrodes and electrolytes [20]. This key difference permits them to charge and discharge much faster and withstand significantly more charge-discharge cycles. Supercapacitors are used in scenarios requiring fast energy charging and discharging, due to their distinct properties. They are being used more frequently in renewable energy systems, electric vehicles, public transportation, and transportable electronic devices, establishing them as an essential part of modern energy solutions [21,22].

While supercapacitors have notable advantages, they show lower energy density as compared to that of conventional batteries. Scientists are continually exploring advanced materials, including graphene and other nanostructured substances, to increase energy storage capability while preserving the primary features of supercapacitors. As global energy systems shift toward more sustainable and efficient technologies, supercapacitors emerge as a promising solution. Their ability to address critical issues such as energy efficiency, reliability, and sustainability underscores their importance in meeting the energy needs of the future [23,24].

Supercapacitors are remarkable in the field of electronics due to their versatility and fast charging and discharging capabilities with exceptional cyclability. These properties make supercapacitors well-suited for a range of applications in energy storage and power transmission [25, 26]. Furthermore, studies on cutting-edge materials such as graphene, carbon nanotubes, and hybrid nanostructures are focused on enhancing supercapacitor

performance to approach the energy density of batteries [27-30]. The development of nanostructured electrode materials has emerged as a method to improve the efficiency of supercapacitors. The characteristics of nanomaterials, including excellent electrical conductivity, extensive surface area, and extraordinary electrochemical stability, have greatly improved the advancement in energy storage technologies [31].

With the goal of optimizing supercapacitors' electrochemical properties, researchers utilize numerous nanostructures, including one-dimensional (1D), two-dimensional (2D), and three-dimensional (3D) designs. Nanostructure modifications enhance electrochemical performance along with power density, making supercapacitors more effective for high-performance applications [32-34]. In supercapacitors, low energy density is still challenging and decreases the efficiency of supercapacitors.

Two-dimensional (2D) materials have become emerging materials for use in supercapacitors as electrodes because of their excellent physical, chemical, and electrochemical properties. These materials, characterized by their ultrathin layered structures, offer several advantages in supercapacitor applications. Their use as electrodes can potentially improve the performance and efficiency of supercapacitors [35]. 2-D materials have become an emerging research area with the discovery of Graphene. Most of their unique features relate to the energy band structure as the material approaches a single atomic layer. The variety of 2D materials is broad, including most elements listed in the periodic table. [36]. Two-dimensional (2-D) materials have gained importance in energy storage applications because of ion intercalation, less weight, chemical stability, good electrical conductivity, and high flexibility [37]. The two-dimensional nature and good aspect ratio make direct integration of 2-D devices easy with most of the planar devices

and increase the sustainability of harsh operating conditions, such as volumetric changes [38].

Two-dimensional materials have certain limitations, such as narrow interlayer spacing and hydrophobicity. The exploration of these drawbacks has contributed to the emergence of novel 2D materials called MXenes [39]. MXenes are two-dimensional structures that mainly consist of carbides and nitrides from early transition metals. Their name ends with "ene" because, like graphene, they have a layered, sheet-like structure. These layers are typically only a few atoms thick, improving surface area and surface chemistry. MXenes exhibit outstanding electrical conductivity, allowing fast electron transport. Their chemical composition can be tuned for specific applications, enhancing performance. Common applications include metal-ion batteries and supercapacitors, where they improve energy density and cycle stability [40,41].

In 2011, Naguib et al initially reported the MXenes. The generic formula used for MXenes is $M_{n+1}X_nT_x$, where M stands for an early transition metal, (n+1) indicates the number of M layers, and n denotes the number of X layers. Surface functionalization of MXenes commonly involves termination groups, such as F, O, OH, and Cl, collectively denoted as T_x. Four distinct MXene compositions, M_2XT_x, $M_3X_2T_x$, $M_4X_3T_x$, and $M_5X_4T_x$, have been successfully developed [42]. $Ti_3C_2T_x$ was first reported and widely used as MXene, and it has a $M_3X_2T_x$ structure [43]. After that, M_2XT_x and $M_4X_3T_x$ were discovered in 2012 by synthesizing Ti_2CT_x and $Ti_4C_3T_x$. Mo_4VC_4 was the first $M_5X_4T_x$ MXene synthesized in 2020 with five atomic layers of transition metal. Up till now, twenty different MXenes have been synthesized, and many are under work and consideration, as shown in Figure 1.4 [42].

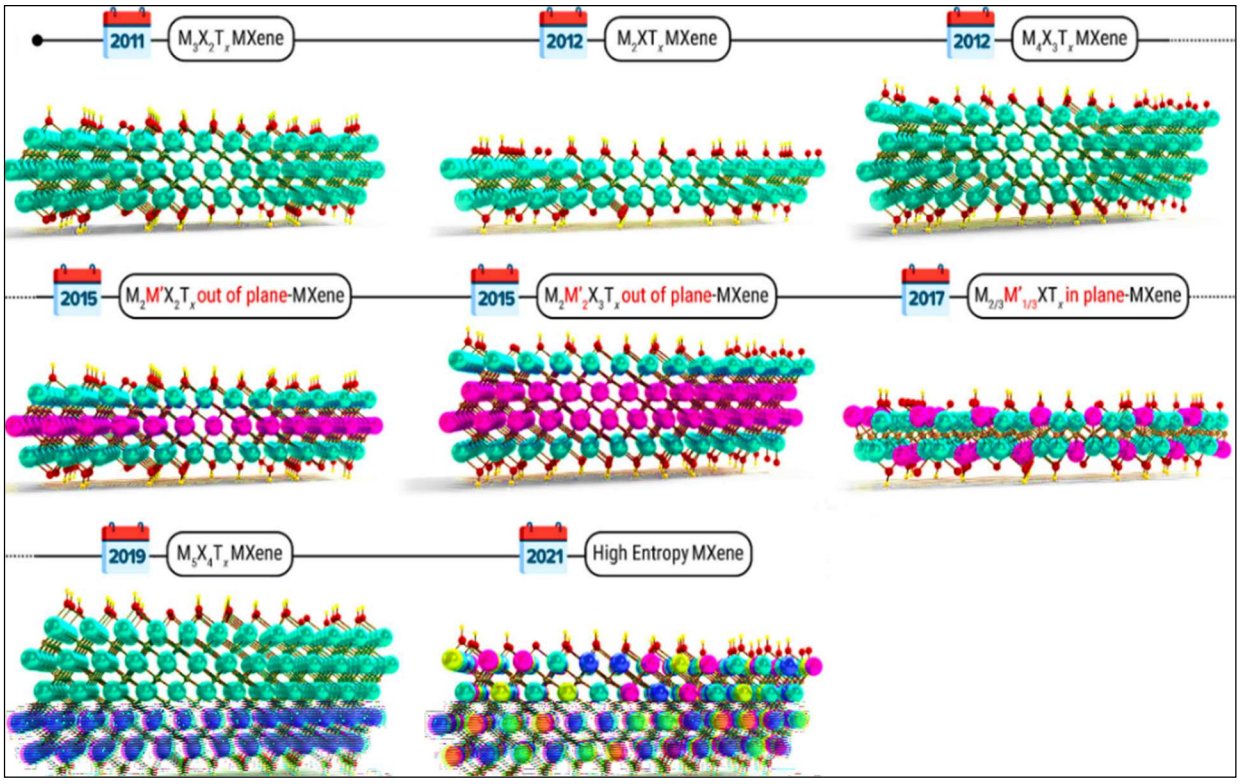

Figure 1.4 Evolution of MXenes [42]

In 2011, the MXene ($Ti_3C_2T_x$) was fabricated by etching aluminum from the MAX phase (Ti_3AlC_2), and HF was used as an etchant [43]. Up till now, 70% of research on MXene depends upon the first discovered MXene, and that discovery was so emerging that some researchers called $Ti_3C_2T_x$ instead of MXenes [44]. Then, other acidic solutions were proposed in addition to HF, such as HCl, LiF, HCL with NaF, and ammonium hydrochloride in organic polar solvents [45]. In 2013, Gogotsi and his colleagues demonstrated the successful incorporation of a wide range of cations into $Ti_3C_2T_x$ MXene electrodes. MXene has rapidly gained attention as a growing research area because of its exceptional properties and wide range of applications. Figure 1.5 presents a detailed overview of its key characteristics and versatile uses, underscoring its importance across various fields [46].

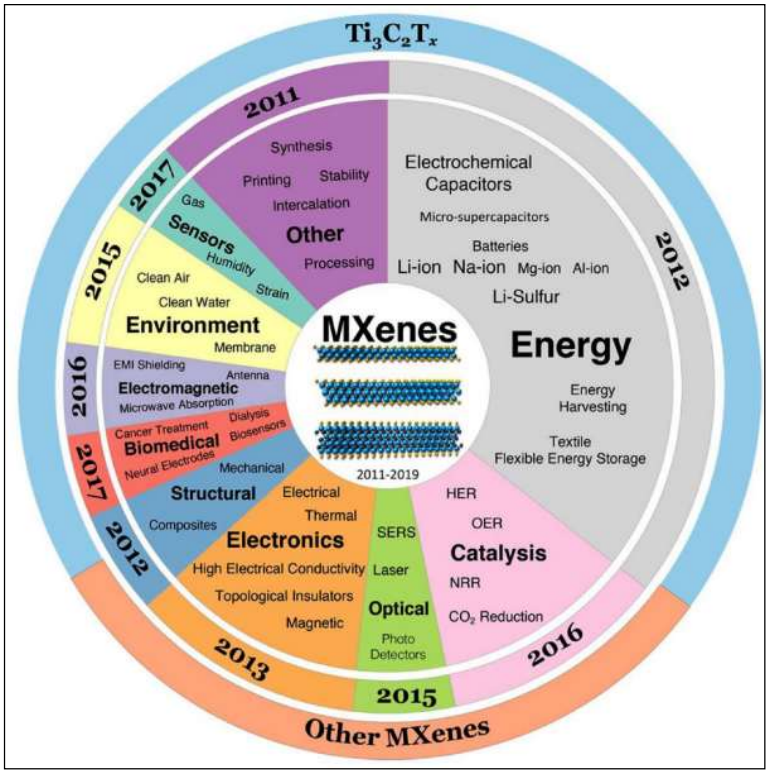

Figure 1.5 Properties and applications of MXenes [46]

Recent research has highlighted key limitations of two-dimensional (2D) materials in supercapacitor applications, including poor cycling stability and limited volumetric capacitance. For example, studies on MXenes reveal rapid capacity loss due to surface oxidation, prompting the development of surface passivation techniques. Graphene-based electrodes face restacking problems, leading researchers to explore spacer materials like carbon nanotubes to maintain interlayer spacing [36]. Additionally, efforts are underway to dope 2D materials with heteroatoms (e.g., N, B) to improve conductivity and redox activity. These investigations show that while 2D materials have potential, issues with structural stability, conductivity retention, and scalable synthesis remain important research challenges [39,40].

1.3 Supercapacitors Applications

Supercapacitors, with their ability to handle high power and fast energy exchange over a long lifespan, are applied extensively in various modern technologies and industries. In transportation, supercapacitors are increasingly integrated into regenerative braking systems for electric and hybrid vehicles. In renewable energy systems, supercapacitors play a critical role in smoothing out power fluctuations from renewable energy sources such as solar panels and wind turbines. This helps ensure stable and reliable power delivery. They are commonly integrated into consumer electronics, including smartphones, wearable technology, and digital cameras, where their rapid charging capability enhances user convenience.

Additionally, supercapacitors are integral to uninterruptible power supplies (UPS). They provide backup energy during power outages. This ensures the uninterrupted functioning of critical systems, including data centres, telecommunications networks, and medical equipment. In military and aerospace applications, supercapacitors are employed in advanced radar systems, satellites, and guided missiles, where high power output is required [47]. Emerging applications include the Internet of Things (IoT), where supercapacitors power sensors and devices that require compact, lightweight, and energy-efficient storage solutions.

Furthermore, research into hybrid supercapacitors is growing rapidly. These devices combine the best features of batteries and traditional supercapacitors. This advancement is expanding their potential applications in electric grids, robotics, and portable medical devices. These diverse applications underscore the transformative impact of supercapacitors across sectors and their pivotal role in supporting the shift toward renewable energy systems [33].

1.4 Gap Analysis and Issues

Despite the rapid advancements in supercapacitor technologies, critical research gaps remain, especially in the advancement of flexible supercapacitors utilizing MXene materials. MXenes have attracted considerable interest due to their excellent electrical conductivity, tunable surface chemistry, and layered structure. However, challenges remain in ensuring long-term electrochemical stability and mechanical durability. Existing studies have largely focused on enhancing capacitance, often neglecting the influence of structural flexibility on device performance. Limited work has been done to integrate MXenes with flexible substrates suitable for wearable applications. Additionally, most reported studies are conducted under ideal laboratory conditions, lacking real-world testing. MXene-based composites have shown promising electrochemical characteristics as an active electrode material used in the electrodes of energy storage devices, but their compatibility and long-term operational behavior are underexplored. Therefore, it is important to conduct detailed studies that go beyond just the synthesis of MXene-based composites. These investigations should also focus on their durability, performance at the device level, and effective design strategies. Evaluating them under realistic operating conditions is essential to ensure practical and reliable performance in applications.

1.5 Problem Statement

Energy harvesting and storage are both integral parts of modern wearable technologies. Technology-ready solutions are required to opt for them for commercial applications. Two-dimensional materials like Graphene and MXenes are tried in energy storage applications due to their low-dimensional structure, high flexibility, and excellent conductivity. The main problem yet to be addressed is the viability of the MXene structure as well as its performance at the circuit level for a wearable energy storage application (specifically in

the supercapacitor domain). To overcome this hurdle, “electrode engineering” may prove to be a sustainable and efficient solution. Symmetrical and asymmetrical configurations of MXenes-based electrodes will be developed, evaluated, integrated, and optimized in this work to qualify their performance viability in commercial energy storage devices. These engineered electrodes may provide a larger extent of surface area with high conductivity magnitude, which are the essential parameters for flexible supercapacitor applications.

1.6 Objectives

The main objectives of this work are as follows:

- To review the technology gaps and design a MXenes-based process architecture by utilizing the electrode engineering approach, which may improve the stability and performance of the flexible supercapacitor devices at the circuit level;
- To fabricate and characterize the devices based on the designed process architecture;
- To optimize the device structure by achieving high gravimetric capacitance, volumetric capacitance, and power density to integrate the devices with commercial applications to provide a technology-ready solution.

1.7 Significance

Supercapacitors are modern electrochemical storage devices, and their progress is in the initial stage. The efficiency of supercapacitors increases in hybrid electrodes, and now inorganic-organic hybrids bring a change in the direction of research. The attractive properties of MXene/organic hybrids have an impact on flexible electronic devices. If MXenes and organic molecules integrate properly, we can utilize the properties of both MXenes and organic molecules for next-generation flexible devices. Supercapacitors have been studied and evolved in the last few decades and are now used for commercial

applications. Flexible supercapacitors have recently evolved and are used in wearable electronics due to their small size and use of liquid electrolytes. Now, the use of supercapacitors is extended to many smart devices such as smartphones, smartwatches, and sensors. Researchers are developing advanced “smart” supercapacitors that can repair themselves (self-healing) and return to their original form after deformation (shape memory). Such innovations could lead to more durable and versatile electronics in the future.

1.8 Thesis Structure

The thesis is organized into six systematically structured chapters.

Chapter 1 presents a fundamental introduction, essential for understanding the foundation of fabricating and assessing flexible materials incorporating MXenes for applications in energy storage.

Chapter 2 gives details of the key ideas that will be necessary for understanding the approach to the problem and further development of its thesis.

Chapter 3 enlists and reviews research and studies taken up in the fabrication and characterization of MXene-based supercapacitors for energy Systems applications.

Chapter 4 provides details about the materials and methodologies used in the study, including experimental setups and data analysis techniques.

Chapter 5 discusses the results and discussion, interpreting the findings and their implications. It shows different approaches used to conduct a systematic study of the problem.

Chapter 6 summarizes the thesis through key takeaways, notable contributions, and recommendations for further research.

1.9 Summary

As fossil fuels diminish and global energy demand continues to grow, the need for reliable, green, effective, low-cost, and sustainable energy storage is a key challenge facing us every day. Batteries and capacitors are the most commonly used energy storage devices. Batteries offer high energy density and long-term storage but have a low power output, while capacitors deliver high power density but have a limited energy storage capacity. Supercapacitors (SCs) bridge this gap between batteries and supercapacitors by offering high specific capacitance, quick charge-discharge capability, and excellent cyclic stability. Extensive research is being conducted to enhance supercapacitor performance, bringing them closer to replacing traditional energy storage solutions. This study focuses on developing innovative MXene-based electrodes for supercapacitors to attain the power requirements of next-generation energy storage applications.

Chapter 2 Background Theory

This section introduces key concepts for understanding the basics of fabricating and characterizing flexible supercapacitors for energy system applications. It also examines the internal structure and working principles of different supercapacitor types, with a particular emphasis on MXene-based supercapacitors for flexible energy storage. Additionally, it explores electrochemical energy conversion and the principles of energy storage.

2.1 Historical Perspective of Supercapacitors

Supercapacitors have become a rapidly evolving and prominent research area over time due to their exceptional characteristics. Researchers are working to improve the efficiency of supercapacitors because modern technologies demand better energy storage solutions. [48].

In 1853, Hermann von Helmholtz was the first scientist who introduce the basic concept of double-layer capacitance. In 1957, Becker received the first patent for the design of a double-layer capacitor from General Electric Corporation [49]. In 1962, the Standard Oil Company of Cleveland, Ohio (SOHIO) was granted a patent for making energy storage devices using the electrode of porous carbon. SOHIO had granted another patent by 1970 for a disc-shaped capacitor.

The firm licensed its double-layer capacitor technology to Nippon Electric Company (NEC) in 1971. In the 1980s, NEC pioneered the commercial release of the first double-layer capacitor, which is today commonly referred to as a "supercapacitor." [50]. In 1975, capacitors were developed using ruthenium oxide films based on the pseudo-capacitive mechanism [51,52].

Then, the industrialization period of supercapacitors began, driven by developments in key technologies such as electrode materials, electrolytes, and manufacturing processes. In 1978, Panasonic developed a type of supercapacitor known as the "Gold capacitor". In 1982, Pinnacle Research Institute(PRI) established the first high-power double-layer capacitor, known as the "PRI Ultracapacitor." [50]. Figure 2.1 shows further development in supercapacitors.

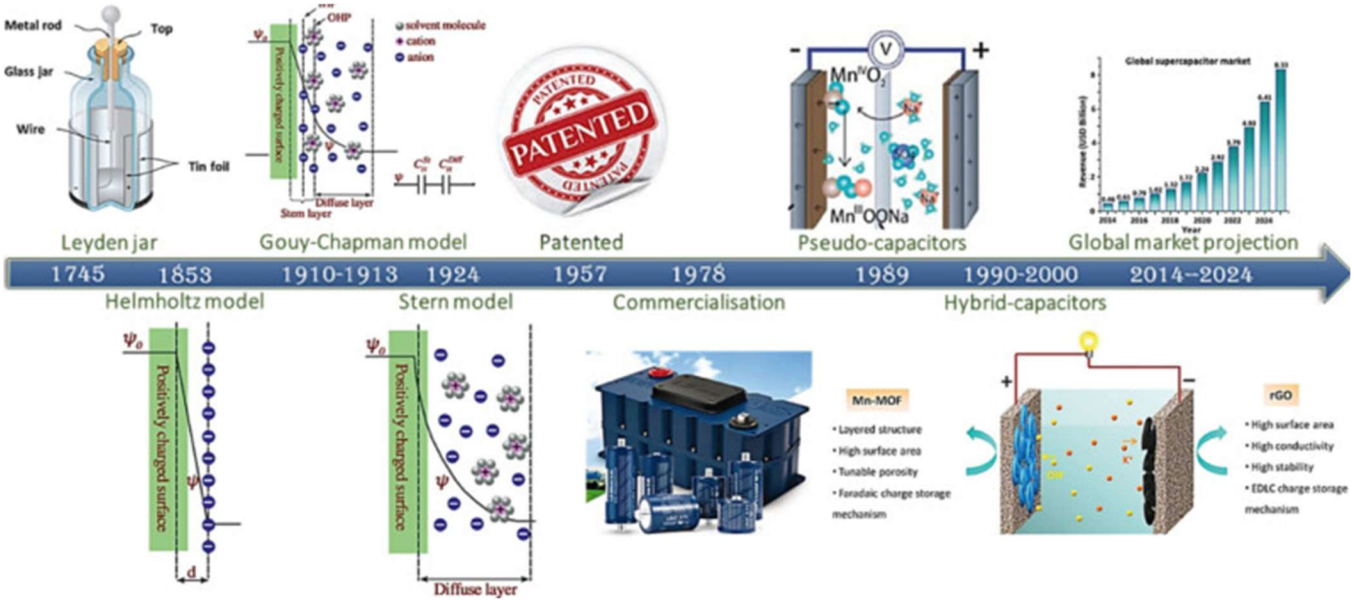

Figure 2.1 Evolution of supercapacitor [25]

Currently, commercial supercapacitors are crucial in many applications because of their long lifespan, fast charging and discharging abilities, and high energy density. They serve as reliable power sources in various devices and technologies, providing efficient and dependable energy solutions for many different needs [53]. The main research areas of SCs are shown in Figure 2.2.

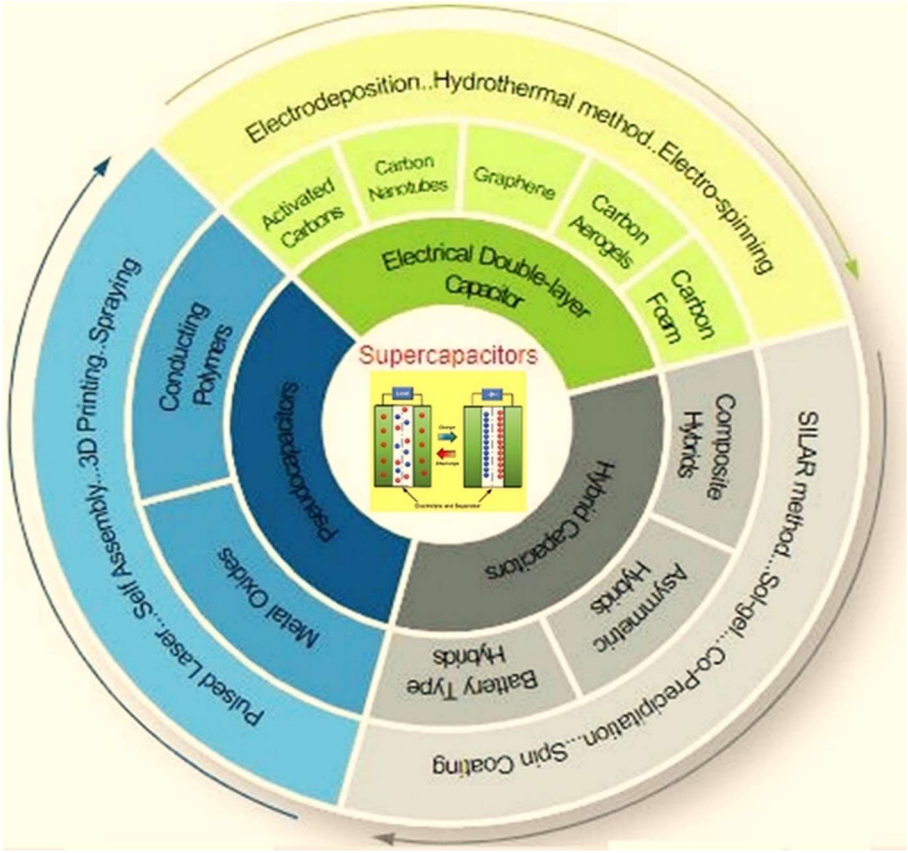

Figure 2.2 Research areas of supercapacitors [53]

2.2 Working Principles of Supercapacitors

Supercapacitors operate primarily on electrostatic principles, specifically the phenomenon of capacitance. Understanding basic capacitance is crucial for grasping the core concepts of supercapacitors. Capacitance is the property of a system that enables it to store electrical charge when a voltage is applied across its terminals. It shows the capacity of the system to collect and store electrical energy in the form of an electric field. The fundamental formula for capacitance in capacitors is shown in Equation 2.1.

$$C = \varepsilon_0 \times \varepsilon_r \times A/d \quad (2.1)$$

This equation for capacitance plays a significant part in the design and operation of supercapacitors because it directly relates the device's capacitance to its physical properties. Each term in the equation represents a specific physical property that influences the supercapacitor's ability to store charge.

In equation 2.1, A denotes the electrode surface area, ε_0 shows the permittivity of free space, ε_r indicates the relative permittivity of the dielectric material, and d represents the distance between two oppositely charged electrodes. This relationship underscores the significance of using electrode materials with a large surface area and fine-tuning electrolyte characteristics to improve the capacitance of supercapacitors [54].

2.3 Supercapacitor Components

A supercapacitor consists of five key components, each with a distinct role in facilitating efficient energy storage and transfer. These include a positive electrode, a negative electrode, a current collector for each electrode, an electrolyte, and a separator. The selection of these components shows variations in the operating voltage of the device and energy density, allowing customization for specific applications [55]. The electrodes are placed in a common electrolyte solution, which enables either electrostatic charge storage or redox reactions.

Various types of electrolytes, such as aqueous and non-aqueous media, have been explored as they determine the supercapacitor's potential stability range and influence its maximum energy storage capacity. To prevent a short circuit, a separator that is ionically conductive but electrically insulating is positioned between the electrodes [56]. Figure 2.3 shows the basic assembly of a supercapacitor.

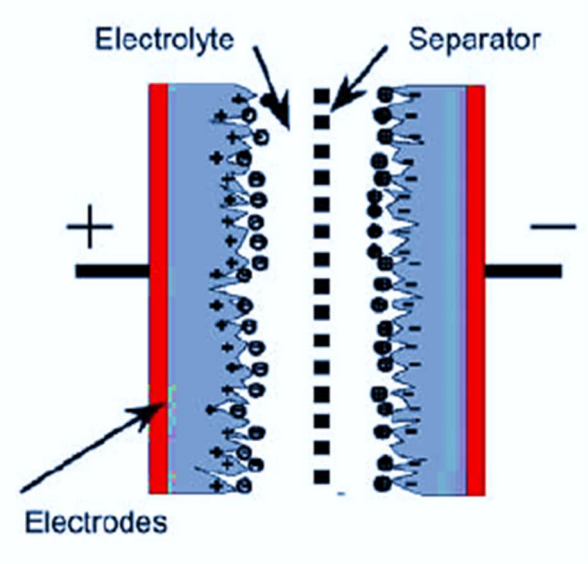

Figure 2.3 Structure of a supercapacitor [55,57]

2.4 Classification of Supercapacitors

Supercapacitors are classified into three primary types according to their charge storage mechanisms: electrochemical double-layer capacitors (EDLCs), pseudocapacitors, and hybrid capacitors.

2.4.1 Electrochemical Double-Layer Capacitors (EDLCs)

An EDLC features carbon-based electrodes separated by a membrane and immersed in an electrolyte. In these devices, charge storage occurs either electrostatically or through a non-Faradaic process, without any charge transfer between the electrodes and the electrolyte [58]. Energy storage in EDLCs relies on the electrochemical double-layer mechanism. When a voltage is applied to a supercapacitor, an electric field is generated, causing a charge accumulation on the surface of the electrodes. This voltage produces a potential difference between the electrodes, attracting oppositely charged particles. This causes ions in the electrolyte to travel across the separator in the direction of the oppositely charged electrode. This process occurs as ions travel through the porous structure of the electrodes

and accumulate on their surface. To inhibit the ion recombination at the electrodes, charge separation takes place, which forms a double-layer structure. This layer consists of ions adsorbed on the surface of the electrode and a layer of opposite ions from the electrolyte, keeping a balanced structure. This arrangement helps prevent ion recombination, which releases stored energy. The energy storage capacity largely depends on the surface area of the material used as an electrode. A greater surface area enables more ion accumulation, thereby enhancing the energy density [59,60]. The mechanism of charge storage of an EDLC is illustrated in Figure 2.4.

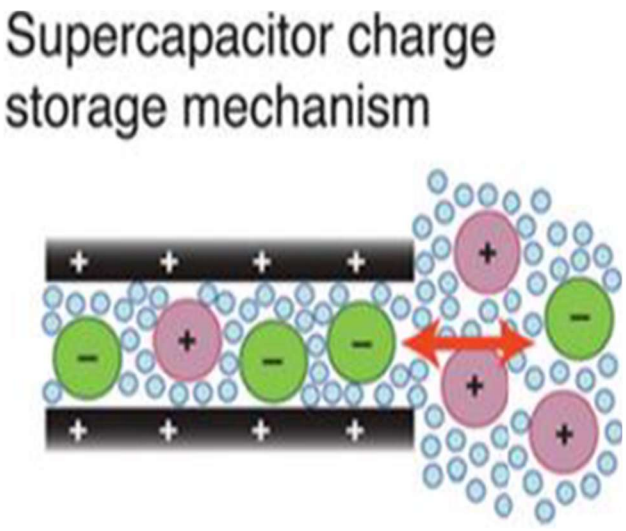

Figure 2.4 Charge Storage Mechanism of EDLC [61]

2.4.2 Pseudocapacitors

In pseudocapacitors, energy storage is governed by Faradaic charge transfer across the electrode–electrolyte interface. In contrast, EDLCs store charge electrostatically at the interface of the electrode and electrolyte without chemical reactions. In pseudocapacitors, the redox (reduction-oxidation) reaction is the key mechanism for charge storage. During this process, the electrode material undergoes a reversible chemical change, either gaining or losing electrons, and stores energy in the process. This allows for higher energy storage

compared to traditional capacitors [62]. Common materials include RuO_2 and MnO_2, which exhibit relatively stable capacitance values within the potential window [63]. Figure 2.5 illustrates the charge storage mechanism of pseudocapacitors.

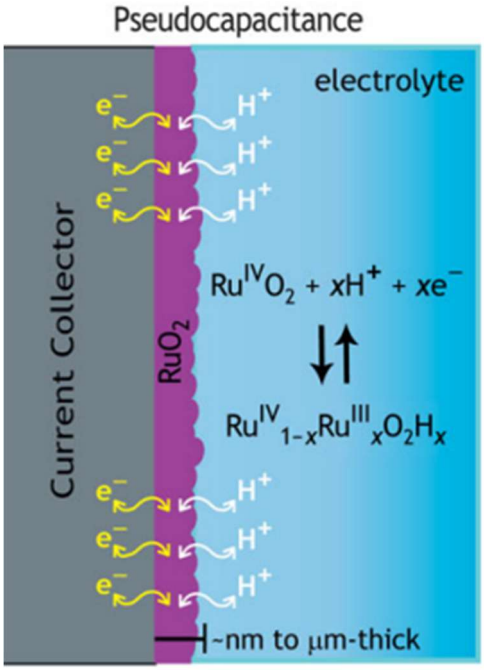

Figure 2.5 Charge Storage Mechanism of Pseudocapacitor [64]

2.4.3 Hybrid Supercapacitors

In a hybrid supercapacitor, charge storage occurs through the grouping of a capacitive carbon electrode and a pseudocapacitive electrode. The hybrid supercapacitors are designed to incorporate the capabilities of EDLC as well as pseudocapacitors. Hybrid supercapacitors combine Faradaic and non-Faradaic mechanisms to deliver greater energy and power densities than EDLCs [60]. Figure 2.6 illustrates hybrid supercapacitor charge storage.

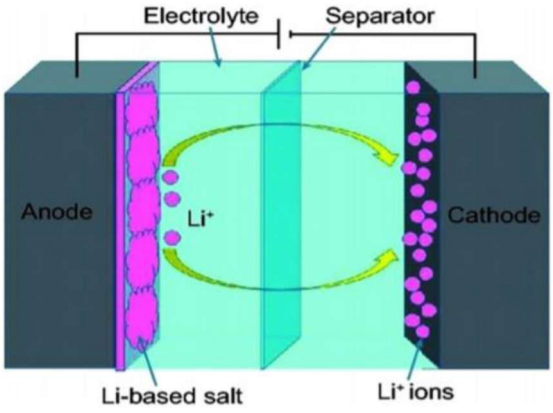

Figure 2.6 Charge Storage mechanism of a hybrid supercapacitor [65]

Figure 2.6 displays that the hybrid SC has two electrodes: one carbon-based and the other lithium-based. Hybrid supercapacitors exhibit superior performance when two different material electrodes are combined compared to using individual electrodes alone. Figure 2.7 presents a comprehensive overview of the different categories and classifications of supercapacitors.

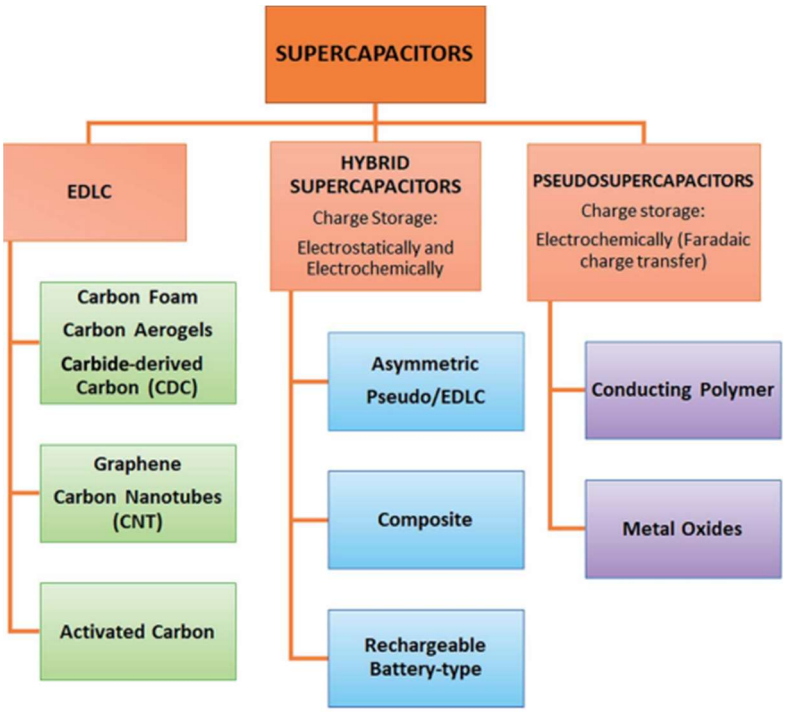

Figure 2.7 Overview of types and classification of supercapacitors [66]

2.5 Electrode Materials in Supercapacitor

Electrode material choice is crucial to supercapacitor performance [67,68]. The first step of supercapacitor fabrication is to select the optimal electrode material with suitable properties. Supercapacitor performance is governed by the interaction at the electrode–electrolyte interface [69,70]. Supercapacitors are classified into symmetric and asymmetric supercapacitors, subject to the arrangement of the electrodes. When two identical electrodes are used in a supercapacitor, it is termed a symmetric supercapacitor [71]. If the electrodes in a supercapacitor are different, it is referred to as an asymmetric supercapacitor [72].

2.5.1 Carbon Materials

Carbon-based materials are generally used as electrode materials due to their numerous advantages. They are non-toxic and abundant, making them environmentally friendly and readily available. Carbon also has excellent electronic conductivity, which ensures efficient charge transfer. Their large specific surface area enables better charge storage, while their wide operating temperature range and high chemical stability make them reliable under various conditions. The combination of properties makes carbon materials ideal for use in applications like supercapacitors [73]. Each type of carbon material offers distinct advantages and challenges, and ongoing research focuses on optimizing these materials to improve power density, energy density, and cyclability. The use of advanced fabrication techniques and hybridization with other materials continues to expand the utilization of carbon-based electrodes in modern supercapacitors. Recent studies have explored a diverse range of carbon-derived substances, such as activated carbon, carbon fiber cloth, carbon nanotubes, hierarchically porous carbon structures, carbon aerogels, and carbon xerogels as prospective electrode materials in electric double-layer capacitors (EDLCs). Porous

activated carbons provide a capacitance changing from 100 to 200 F/g. With a specific surface area of approximately 2000 m^2/g, they function as effective electrode materials [74] . Enhancing the specific surface area facilitates greater charge accumulation on the boundary between the electrode and the electrolyte. Carbon-based materials can be utilized as electrodes if they have three basic properties: (a) surface area of more than 1000 m^2/g, (b) High conductivity, and (c) extraordinary electrolyte compatibility to the intra-pore space of carbon-based electrode materials [75]. Carbon nanotubes (CNTs), commonly found as single-walled (SWCNTs) or multi-walled (MWCNTs) structures, are cylindrical nanostructures recognized for their outstanding electronic properties. They are highly effective as electrodes in SCs due to their exceptional electrical conductivity and expansive surface area. Furthermore, their mesoporous architecture facilitates effective electrolyte ion diffusion. However, due to their high production costs, CNTs are often integrated with other materials to enhance cost-effectiveness and performance [76].

2.5.2 Metal Oxides

Metal oxides show higher specific capacitance than carbon-based electrode materials. Metal oxides like MnO_2, NiO, Co_3O_4, RuO_2, and V_2O_5 serve as potential electrode materials in supercapacitor devices due to their pseudocapacitive behavior, high capacitance, and compatibility with various carbon-based materials [77]. Nickel oxide (NiO) stands out as a promising material because of its widespread availability and remarkable theoretical capacitance, which can reach up to 2584 F/g. It works efficiently in alkaline electrolytes and shows good electrochemical stability. The challenges include low conductivity and mechanical degradation during cycling [78]. Co_3O_4 features a spinel assembly with a large surface area, aiding effective electron and ion transport. It has been widely studied for its synergistic redox reactions. However, similar to NiO, its performance is limited by poor

conductivity and structural instability [79]. Fe_3O_4 is an abundant and cost-effective material with moderate capacitance. It is often used in composite systems to enhance conductivity and stability. The cyclic stability of Fe_3O_4 is a challenge due to its structural degradation [79].

2.5.3 Conducting Polymers

Conducting polymer-based pseudocapacitors have achieved considerable success in flexible and portable supercapacitor applications due to several key advantages. These materials exhibit excellent electrical conductivity, enabling efficient charge transfer. They show redox-active capacitance, which means they can store and release charge through reversible electrochemical reactions. Their flexible nature makes them a perfect choice for technologies needing lightweight, bendable, and compact energy storage solutions, such as wearable devices and flexible electronics [80]. Conducting polymers such as polyaniline (PANI), poly(3,4-ethylenedioxythiophene): polystyrene sulfonate (PEDOT: PSS), and polypyrrole (Ppy) are widely utilized due to their outstanding electrical conductivity and improved electrochemical properties. Recently, these polymers have been widely used because of their reversibility, high charge storage capacity, and significantly lower cost compared to metal oxides [81]. PANI is a highly promising supercapacitor electrode material due to its exceptional electrochemical properties, such as high conductivity, facile synthesis, and reversible redox behavior. PANI exhibits elevated conductivity because of the delocalized electrons in its resonance-stabilized double bond structure [82]. PEDOT: PSS is widely favored as an electrode material due to its exceptional properties. It exhibits strong environmental and thermal stability, ensuring reliable performance in various conditions. Its low redox potential contributes to efficient charge transfer during

electrochemical reactions. PEDOT: PSS offers extraordinary conductivity, which enhances its performance in energy storage applications [83,84].

2.5.4 Graphene

Graphene is a material just one atom thick with a two-dimensional structure. It has become recognized as an exceptional carbon material with significant potential for application in energy storage devices [85, 86]. Graphene, as an electrode material, provides outstanding features including a large surface area, strong chemical stability, and superior electrical conductivity [87,88]. Graphene is used as an electrode material in advanced energy storage devices, especially supercapacitors, due to its specific surface area of 2600 m^2/g, excellent charge mobility of ~230,000 $cm^2/V \cdot s$, and high thermal conductivity of ~3000 W/mK [89].

2.5.5 MXenes

MXenes are emerging two-dimensional (2D) materials that have gained significant attention for use as electrode materials in energy storage devices, due to their tunable interlayer spacing, minimal diffusion resistance, and excellent metallic conductivity. Their exceptional combination of properties makes them suitable for supercapacitor applications, offering improved charge storage and transport capabilities [90, 91].

Two important parameters of supercapacitors are high capacitance and life cycle. Fast intercalation occurs due to the 2-D structure of increased access to active sites of MXenes for high pseudocapacitive charge storage behavior [92]. High gravimetric capacitance and high density give rise to ultrahigh volumetric capacitance and are necessary to improve device efficiency [93]. Electrical conductivity plays a significant role in efficiency improvement. Bare MXenes generally exhibit metallic characteristics similar to their precursor materials. However, their electronic conductivity can be altered by the presence

of surface termination groups [44]. The high electronic conductivity of MXenes results in rapid electron transfer, an adequate increase in the availability of the surface area, and stabilizes the structure of the active material [92]. MXenes nanosheets can be used in combination with graphene as electrodes in a flexible supercapacitor [94]. MXene shows a semiconductive nature with a small bandgap. The band gap of most of the MXenes is indirect, excluding $Sc_2C(OH)_2$, which is a MXene with a direct bandgap [95]. The oxidation state of simple M elements is less than the oxidation state of their respective oxides in MXenes, based on Bader charge analysis [96]. Termination groups mainly decide the oxidation states of MXene. Full degradation of MXene ($Ti_3C_2T_x$) solutions occurs in the atmosphere in 15 days and develops TiO_2 [97]. In Figure 2.8, several properties of MXenes are highlighted as electrode material in energy storage devices [92].

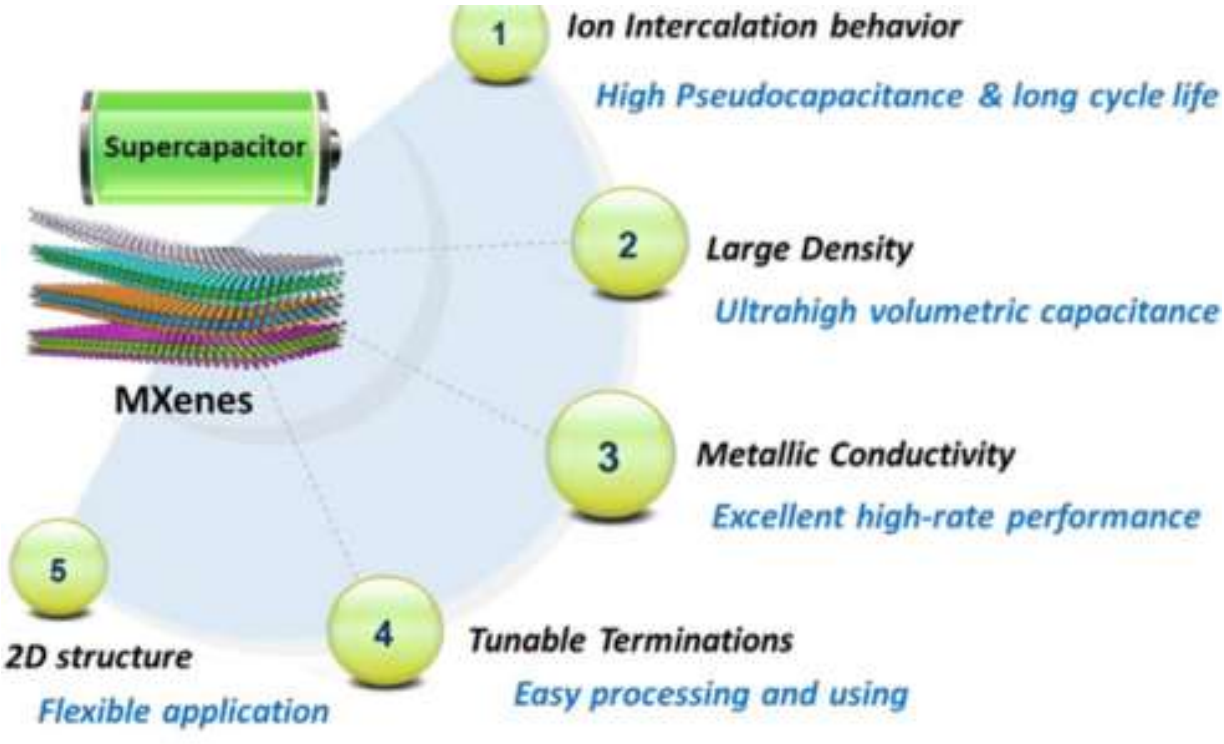

Figure 2.8 Properties of MXenes for supercapacitors [92]

MXenes are categorized based on the transition metal components into Mono-transition-metal MXenes (Mono-M) and Double-transition-metal MXenes (DTM) [98, 99]. In Mono-M MXenes, M layers consist of single types of transition metals such as Ti_2CT_x, V_2CT_x, $Ti_3C_2T_x$, and $Nb_4C_3T_x$. Double transition-metal MXenes (DTM MXenes) consist of two distinct transition metals within their structure. This metal combination enables a wider series of variable properties, including improved electrical conductivity, mechanical strength, and chemical stability [100]. MXenes are synthesized by carefully etching A-group elements from MAX phase precursors. The MAX phase is generally characterized by the formula $M_{n+1}AX_n$, where n can be 1, 2, 3, or 4. In this formulation, M denotes an early transition metal, A signifies an A-group element, and X indicates a carbide or nitride [101]. MAX phases are hexagonal, layered ternary carbides or carbonitrides of transition metals. The elements that form MAX phases or their precursors from the periodic table are illustrated in Figure 2.9 [102].

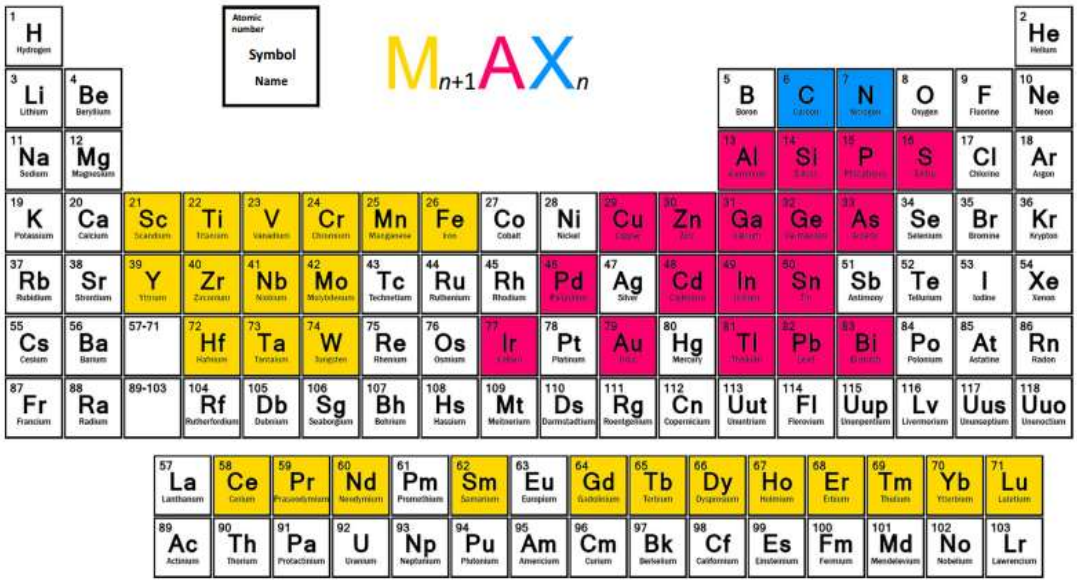

Figure 2.9 Elements constituting MAX phases [102]

The schematic diagram of MAX phases and resulting MXenes obtained from MAX phases is shown in Figure 2.10. TiC is used as a raw material in the preparation of the MAX phase and remains present in MXene as an "impurity" after the etching [103,104]. The 'M,' 'A,' and 'X' sites in MAX phases can be modified through doping or alloying with other elements. Diversity in MAX phases is the main point of concern. The other major point of concern in their versatility is that their chemistry can be changed while keeping their structure the same. Mainly, MXenes are typically produced by etching aluminum (Al) from MAX phases, with a few exceptions, such as Mo_2C was synthesized from Mo_2Ga_2C [105]. This was a complex and unique example of MXene, where molybdenum (Mo) is used as the M element. This example opens a new pathway for synthesizing MXenes from challenging MAX phases [106].

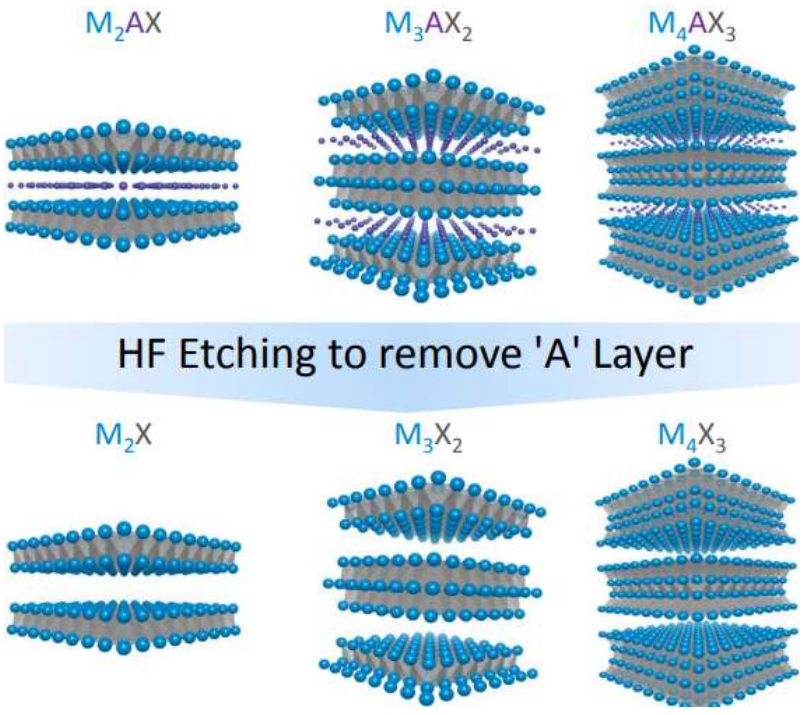

Figure 2.10 Schematic illustration of MAX phases [38]

Recently, researchers have focused on modifying the synthesis of new MAX phases, as these changes impact MXene production. The purity of the MAX phase is crucial in defining the quality of the synthesized MXene [107,108]. MXene fabrication starts with the etching of A elements from precursor materials using any etchants, such as HF.

2.5.5.1 Preparation of MXenes

The preparation of most MXenes includes three steps.

2.5.5.1.1 Etching of MAX Phases

In MAX phases, the chemical bond arrangement is distinctive. In MAX phases, MX bonds (covalent and ionic) are strong, whereas MA bonds are relatively weaker metallic bonds. [109]. It is difficult to directly break the MA bonds, so the first etching is performed by an etchant like HF. The reactions of the HF solutions with the first discovered MXenes, Ti_3AlC_2, include [37]:

$$2Ti_3AlC_2 + 6HF \longrightarrow 2AlF_3 + 3H_2 + 2Ti_3C_2$$

$$Ti_3C_2 + 2H_2O \longrightarrow Ti_3C_2(OH)_2 + H_2$$

$$Ti_3C_2 + 2HF \longrightarrow Ti_3C_2F_2 + H$$

These equations describe the elimination of Al atoms in Reaction 1, followed by the termination of MXene with hydroxyl groups and fluorine atoms in Reactions 2 and 3, respectively. Furthermore, oxygen terminations were later observed in MXenes [110].

2.5.5.1.2 Intercalation

MXenes can intercalate various ions and molecules between their layers. Intercalation is an optional step, but sometimes it is necessary to enhance surface properties. Intercalation can be done in MXenes by many molecules, for example, urea and hydrazine, along with

different cations, for example, Na^{+}, K^{+}, $Rb^{+,}$ and Mg^{+2}. Intercalants can increase the device's resistance [111].

2.5.5.1.3 Exfoliation

Exfoliation is used to obtain a single-layer or a few-layer MXenes colloidal suspension. Water is used many times to wash MXenes, or it may be pre-washed with acid for dissolving by-products of salts, e.g., AlF_3 or LiF. Exfoliation can be done after washing to make a mono-layer or a few-layer MXene. Methods of doing exfoliation are mainly determined by MXene composition and by the methods of etching used. All steps of MXene preparation are shown in Figure 2.11 [112].

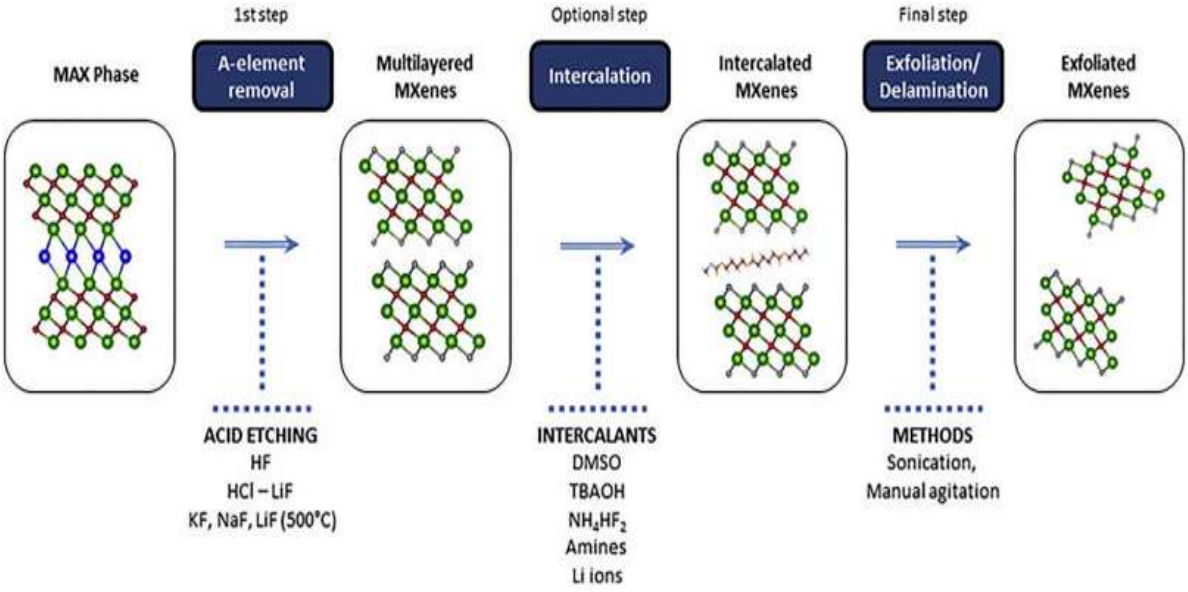

Figure 2.11 Steps of MXenes Preparation [112]

2.5.5.2 Fabrication Methods of MXenes

Different methods are used to fabricate MXene films, such as vacuum-assisted filtration (VAF), electrospinning or spraying, hot pressing, and spin coating.

2.5.5.2.1 Vacuum-Assisted Filtration

MXenes can be fabricated through Vacuum-assisted filtration to make interlayer hydrogen-bonded hybrid films [113,114]. In Vacuum-assisted filtration, the application of high pressure to films leads to the removal of water-soluble polymers from the molecules. It will affect the original composition of MXenes and change the relationship between results and composition.

2.5.5.2.2 Spin Coating

Spin coating is a fast and efficient way to make uniform MXene films. First, by stirring or ultrasound, a homogeneous solution is prepared consisting of a colloidal solution of MXenes with the required additives. The prepared homogeneous solution is then spread over the clean substrate to permit solvent evaporation under centrifugal force, under high vacuum, and temperature. Then, the composite of MXene is separated from the substrate. [115].

2.5.5.2.3 Hot Pressing

Composite MXene-polymer films can be produced via hot pressing at temperatures above the polymer's melting point but below MXenes' degradation temperature, since MXenes are more thermally stable than polymers [116].

2.5.5.2.4 Electrospinning/Spraying

Electrospinning/spraying is used to manufacture fibrous films and nanofibers with enhanced flexibility. It is used to make MXene/PVA nanofiber films by adding material of the PVA matrix to nanosheet suspensions of $Ti_3C_2T_x$. [117].

A summary of several fabrication techniques of MXenes and different methods of preparation of MXene films is given in Tables 2.1 and 2.2, respectively.

Table 2.1 Fabrication Techniques of MXenes

Technique	**Advantage**	**Application**	**Ref**
Vacuum Assisted Filtration	Simple	Supercapacitors	[118]
Spin coating	Well-defined composition and rapid film-forming	Photodetectors	[115]
Hot press	Flexible and solvent-free	Coating	[119]
Electrospinning	Structural tunability	Oil-water separation	[117]

Table 2.2 Methods of preparation of MXene films

Material	**Electrodes**	**MAX phase**	**Method**	**Ref**
$Ti_3C_2T_x$	Macro porous MXene	Ti_3AlC_2 Mo_2Ga_2C	Vacuum-assisted filtration	[93]
$Ti_3C_2T_x$	(MNFs)/CNT	------	Spin coating	[120]
MnO_x/ $Ti_3C_2T_x$	MnO_x-Ti_3C_2	4g Ti_3AlC_2	Vacuum-assisted filtration	[121]
$Ti_3C_2T_x$/ rGO	Sandwich-like $Ti_3C_2T_x$ /rGO	Ti_3AlC_2	Vacuum-assisted filtration	[118]
Ti_3C_2/Ppy	Ppy/ $Ti_3C_2T_x$	Ti_3AlC_2	Vacuum-assisted filtration	[122]

2.6 Electrolytes

Electrolytes are considered the most essential component of supercapacitors, as their performance is significantly affected by them. Electrolytes facilitate ion conductivity and enable charge compensation at the electrodes of supercapacitors. They are composed of dissolved chemicals and solvents that generate positive and negative ions, thereby ensuring

conductivity [123]. Electrolytes are vital in shaping the essential characteristics of supercapacitors, such as rate performance, cycle life, internal resistance, power density, energy density, toxicity, and self-discharge [124].

The key features of an ideal electrolyte include (a) high ion conductivity, (b) a broad voltage range, (c) stability, (d) compatibility with electrodes, (e) environmental safety, (f) affordability, (g) low volatility, and (h) low flammability. Figure 2.12 illustrates the factors affecting electrolyte properties in supercapacitors.

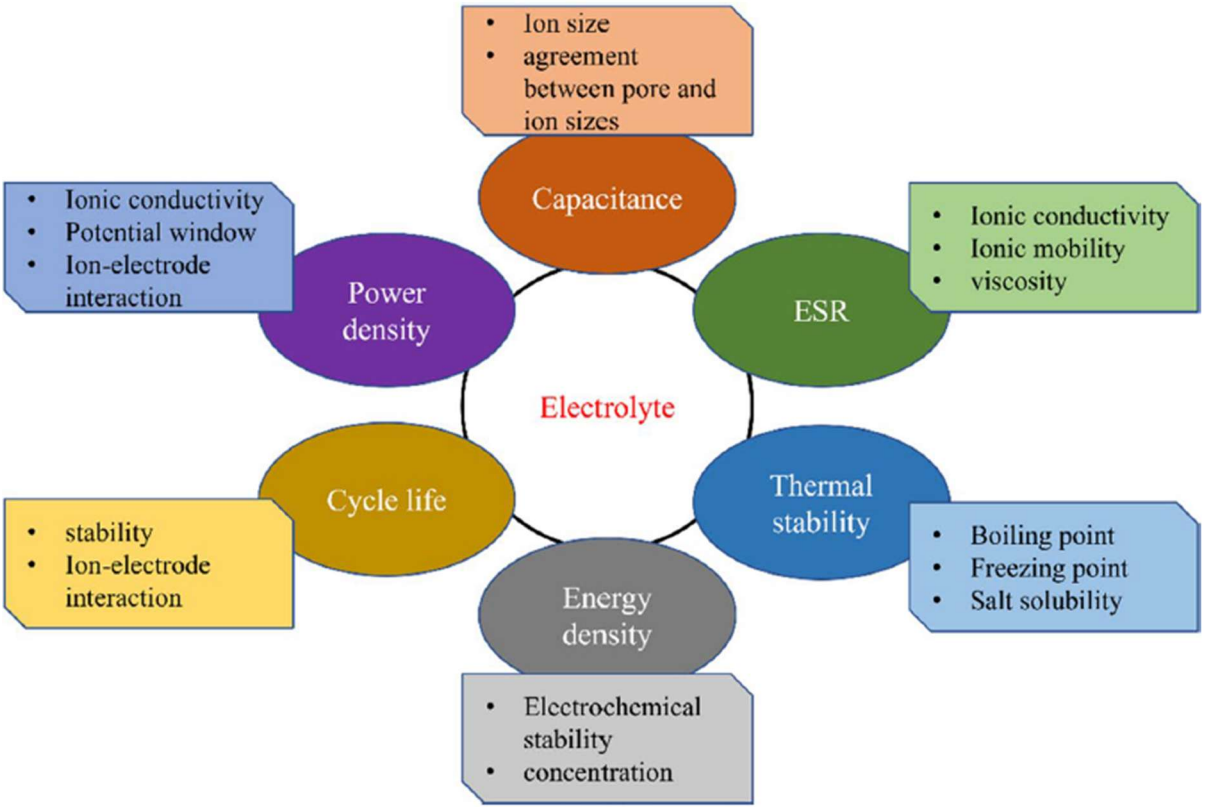

Figure 2.12 Factors Affecting Electrolyte Properties [98]

Supercapacitors utilize various types of electrolytes, including liquid-state, solid-state, and redox-active electrolytes, as illustrated in Figure 2.13. Each electrolyte plays a distinct role in determining conductivity, stability, and energy density.

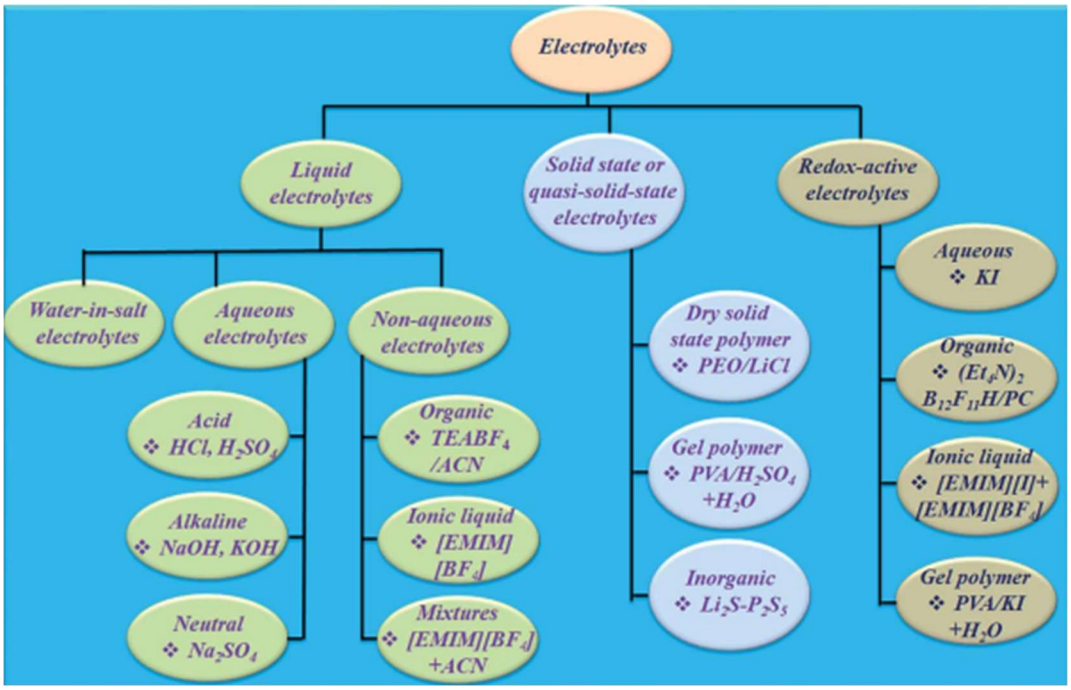

Figure 2.13 Classification of electrolytes for electrochemical supercapacitors [125]

The long-term stability and performance of supercapacitors are significantly influenced by the type of electrolyte used, each presenting distinct challenges [98]. Aqueous electrolytes, while offering high ionic conductivity, suffer from a narrow electrochemical stability window, limiting energy density and causing faster electrode degradation due to water decomposition. Organic electrolytes extend the voltage window, but their flammability, toxicity, and lower ionic mobility raise safety and efficiency concerns over extended use. Ionic liquids provide excellent thermal and electrochemical stability, yet their high viscosity and cost hinder ion transport and commercial scalability. Moreover, solid-state electrolytes, though safe and compact, often exhibit poor interfacial contact and limited ionic conductivity. Overcoming these limitations through the development of advanced formulations, the incorporation of suitable additives, or the use of hybrid electrolytes is crucial for improving device performance and extending operational lifespan [125]

2.7 Summary

Supercapacitors, a type of electrochemical capacitor, offer remarkable advantages over traditional capacitors. They have a long cycle life, allowing them to operate effectively through hundreds of thousands of charge–discharge cycles with minimal performance degradation. They deliver superior power and energy densities, making them suitable for applications demanding rapid charging and high-power output, and reliable long-term performance. Their performance is affected by how the electrode interacts with the electrolyte materials. Strong and well-optimized interactions facilitate efficient charge transfer and enhance ion accessibility within the electrode structure. Recent research has highlighted the potential of MXene materials as suitable candidates for electrodes in supercapacitors. There are three primary classifications of supercapacitors. The most basic and widely available type of supercapacitor is the Electrostatic double-layer capacitor, which stores charge electrostatically. Electrochemical pseudocapacitors have higher energy densities due to surface-level redox reactions during charging and discharging. Hybrid supercapacitors show high capacitance and energy storage properties in the combination of EDLC and pseudocapacitor properties.

Chapter 3 Literature Review

This section of the thesis covers research and investigations into the fabrication and analysis of MXene-based supercapacitors for energy storage applications. MXenes, as promising electrode materials, are gaining increasing attention in the energy storage field.

3.1 Parameters for Development in MXene-based Electrodes

In supercapacitors, MXenes can serve as electrodes with either 1D or 2D substrates. Future progress should focus on enhancing specific capacity and power density while also improving capacitance, cost-effectiveness, and stability. Scientists are improving MXenes-based electrodes for energy storage devices, mainly supercapacitors, by considering some parameters [126,127].

3.1.1 Composition

After discovering the first MXene, new MXenes are found for use in supercapacitors as electrode materials in addition to $Ti_3C_2T_x$. MAX phases of more than 100 different MXenes consist of various transition metals, their alloys with carbon and nitrogen, and surface terminations. Their properties are largely influenced by the intrinsic characteristics of the elements used and the nature of surface terminations [92].

3.1.2 Chemical Modification of MXenes

Heteroatom doping increases the efficiency of electrodes in supercapacitors. To improve their properties, many different materials can be introduced into MXene nanosheets [126]. MXenes are prepared by etching the MAX phase with different surface terminations (–O, –OH, and –F). These terminations influence factors such as electronic conductivity, interlayer spacing, and ion adsorption [92]. Oxygen-containing terminations can increase hydrophilicity, which improves pseudocapacitive behavior [128].

3.1.3 Structure and Morphology Control

The open structure and morphology customization are crucial factors in enhancing the electrochemically accessible surface area of MXenes. Their structure is highly adaptable, offering significant variability. Several strategies have been suggested in the literature, including controlling flake size, adjusting interlayer spacing, optimizing molecular stacking, and implementing vertical alignments. These approaches aim to achieve higher volumetric capacitance, more active sites, a high specific surface area, and improved power density [126]. Table 3.1 shows techniques to improve the stability of MXene-based supercapacitors.

Table 3.1 Techniques to improve stability

MXene	**Etchant**	**Precursor**	**Treatment to enhance stability**	**Stability time**	**Reference**
SA-$Ti_3C_2T_x$	LiF–HCl	Ti_3AlC_2	Sodium ascorbate capping	80 days	[129]
Ti_3C_2	HF–HCl	Al-Ti_3AlC_2	Modified synthesis of Ti_3AlC_2 to produce a more stoichiometric MAX phase Al-Ti_3AlC_2	300 days	[107]
r-$Ti_3C_2T_x$	HF	Ti_3AlC_2	L-ascorbic acid	28 days	[130]
$Ti_3C_2T_x$	LiF–HCl	Ti_3AlC_2	- 20 °C freeze storage	650 days	[131]

3.2 MXene-Enabled Impurities (TiC)-based Electrodes

Transition metal carbides are excellent electrode materials for supercapacitors due to their notable properties, high electrical conductivity, and improved chemical stability. Among various transition metal carbides, Titanium carbide (TiC) is notable for its exceptional resistance to corrosion, high thermal stability, and strong oxidation resistance. [132,133]. TiC (MXene-enabled impurities) has low density (4.93 g/cm^3), high microhardness (28 GPa), high Young's modulus (450 GPa), and electrical conductivity (up to 10^5Sm^{-1}) [134,135]. Titanium carbide (TiC), known for its exceptional properties, serves as a raw material in the preparation of the MAX phase, remaining as an "impurity" in the MXene following the etching process. A comparison of various supercapacitors with Titanium carbide-based electrodes is presented in Table 3.2.

Table 3.2 Comparison of the Capacitance of various TiC-based supercapacitors

Device	**Electrolyte**	**Specific Capacitance**	**Scan rate**	**Ref.**
TiC/C//TiN/C	Na_2SO_4	103 F/g	0.5 A/g	[136]
TiC nanotube arrays	PVA–Na_2SO_4	4.05 mF/ cm^2	0.05 mA/cm^2	[137]
TiC nanotube arrays	PVA–KOH	27.6 mF/ cm^2	0.4 mA/cm^2	[137]
TiC nanotube arrays	PVA-H_3PO_4	53.3 mF/ cm^2	0.2 mA/cm^2	[138]

3.3 MXene-based Electrodes for Supercapacitors

MXenes serve as electrode materials in batteries (such as lithium-ion and sodium-ion) and supercapacitors due to their outstanding electrochemical characteristics, including rapid ion diffusion and excellent conductivity [139,140]. MXenes can serve as conductive frameworks to support active materials in hybrid electrode designs, enhancing the overall

performance by providing mechanical stability and improved charge transport [141-144]. Various MXenes-based composites for supercapacitors are discussed in Figure 3.1. The application of different types of MXenes in energy storage has been growing rapidly, especially as electrode materials for batteries and supercapacitors [145]. Recently, researchers have worked on enhancing the electrochemical properties of MXenes by modifying the surfaces with conducting polymers.

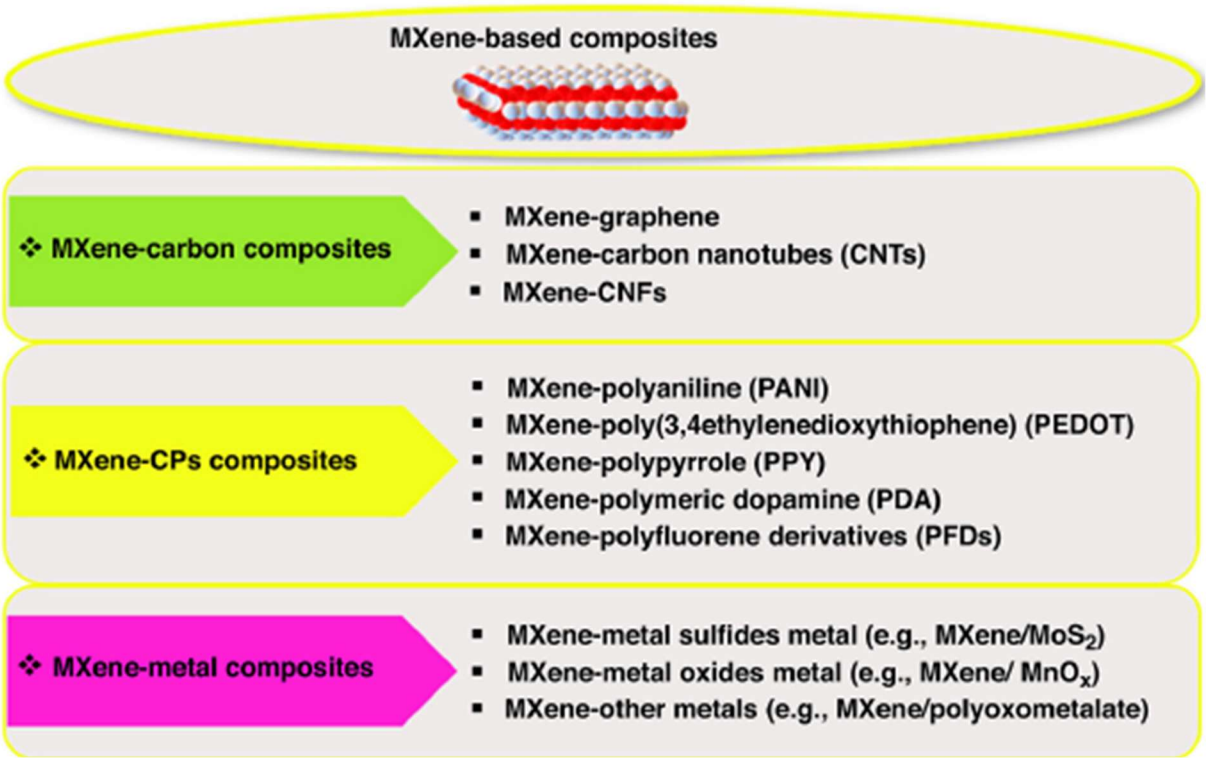

Figure 3.1 MXene-based composites for supercapacitor electrodes [144]

To overcome this challenge, researchers employ a synergistic intercalation approach by incorporating various materials into the polymer matrix. By using this approach, charge storage is increased, cyclic stability is strengthened, and rate performance is optimized [146,147]. A common approach to enhance the electrochemical performance of MXene-based electrodes is to form composites that combine MXenes with different conducting

polymers, such as polypyrrole (PPY), polyaniline (PANI), and PEDOT: PSS [148,149]. When combined with conducting polymers, MXenes offer exceptional properties because of the integration of surface terminal groups in the conducting polymers (CPs). This enhancement is mainly attributed to the advantageous qualities of conducting polymers, such as high electrical conductivity, lightweight, flexibility, and affordability [150]. PANI is regarded as an emerging electrode material that improves the electrochemical properties of MXenes [151]. PEDOT: PSS is used as an exceptional electrode material due to its low redox potential, outstanding electrical conductivity, and doping capability. When integrated with MXene, PEDOT: PSS boosts its electrical conductivity, which in turn accelerates the electron–ion transport rate in $Ti_3C_2T_x$ [152].

Integrating MXenes with conductive polymers could greatly improve energy storage and sensing devices, but there are several challenges remain to be resolved. A key issue is the mechanical instability of conducting polymers, which undergo significant expansion and contraction during charge–discharge cycles. This leads to the formation of cracks and structural degradation over time, reducing device lifespan. Additionally, achieving a uniform and well-adhered polymer coating on the MXene surface is difficult. An uneven polymer distribution can negatively impact the composite's conductivity, electrochemical performance, and structural stability electrode. These factors together undermine the long-term stability and efficiency of the supercapacitor system. While researchers are actively exploring strategies like surface modification and composite engineering to tackle these issues, developing scalable and reproducible synthesis methods continues to be a challenge, posing a significant barrier to real-world applications [144,149].

3.3.1 MXene-based Symmetric Supercapacitors

Symmetric supercapacitors (SSC) have the same electrodes and no charge imbalance. Charge imbalance causes disturbance in electron kinetics between two electrodes, and mass ratio determination also becomes difficult [153].

Xia et al. utilized the highly representative $Ti_3C_2T_x$ MXene material to fabricate symmetric $Ti_3C_2T_x$ supercapacitors using an unconventional electrolyte made from seawater. At a current density of 0.25 A/g, the symmetric supercapacitor demonstrated a volumetric capacitance of 27.4 F/cm³. Even at a higher current density of 3A/g, it showed an outstanding volumetric capacitance of 12.6 F/cm³ while demonstrating excellent cyclic stability. When tested at 10 A/g, the device maintained 96.6% of its capacitance after 5000 charge-discharge cycles[154].

A flexible and dense MXene film ($Ti_3C_2T_x$) was fabricated by Yang et al by compressing traditional MXene films, thereby eliminating the need for binders. This advanced technique resulted in a freestanding electrode with exceptional density, making it well-suited for supercapacitor applications. Experiments proved that the volumetric capacitance of supercapacitors constructed from MXene films increases with greater mechanical pressure. A symmetric supercapacitor (SSC) with $Ti_3C_2T_x$ film compressed at 40 MPa in 1 M Li_2SO_4 achieved a high volumetric capacitance of 633 F/cm³ at a scan rate of 2 mV/s [155].

Wu et al. Successfully fabricated Ti_3C_2/PANI nanotubes (Ti_3C_2/PANI-NT) composites with a well-defined hierarchical structure. In this composite, Ti_3C_2 MXene nanosheets improve the material's mechanical strength and electrical conductivity. The integration of PANI-Nanotubes successfully reduces the self-stacking tendency of Ti_3C_2 nanosheets, resulting in greater interlayer spacing and an enhanced surface area. These structural developments result in superior electrochemical performance.

Using a three-electrode configuration with 1 M H_2SO_4 as the electrolyte, the Ti_3C_2/PANI nanotube (Ti_3C_2/PANI-NT) composite exhibited a high specific capacitance of 596.6 F/g at a current density of 0.1 A/g. It also demonstrated excellent cyclic stability, retaining 94.7% of its initial capacitance after 5000 charge-discharge cycles. Using these findings, a symmetric supercapacitor (SSC) assembled with Ti_3C_2/PANI-NT electrodes also showed notable energy storage capabilities. The SSC delivered 25.6 Wh/kg energy and 153.2 W/kg power density, demonstrating its importance for practical use in high-performance supercapacitors [156].

Zhou et al. created i-PANI@$Ti_3C_2T_x$ composites and manufactured Lig@$Ti_3C_2T_x$ and Lig@$Ti_3C_2T_x$/i-PANI@$Ti_3C_2T_x$ films for use in flexible supercapacitors (SSCs). Using a PVA/H_2SO_4 electrolyte, the SSCs based on these materials achieved specific capacitances of 310 F/g (~1001 F/cm³) for i-PANI@$Ti_3C_2T_x$, 271 F/g (~881 F/cm³) for Lig@$Ti_3C_2T_x$, and 295 F/g (~959 F/cm³) for their hybrid Lig@$Ti_3C_2T_x$/i-PANI@$Ti_3C_2T_x$ at a current density of 1 A/g. Importantly, the Lig@$Ti_3C_2T_x$/i-PANI@$Ti_3C_2T_x$-based device demonstrated excellent mechanical durability, highlighting its strong potential for flexible energy storage solutions [157].

Table 3.3 provides a detailed comparison of the capacitance values obtained from various MXene-based symmetric supercapacitors, highlighting variations in performance due to differences in electrode material composition and electrolyte type. This comparison helps identify which MXene modifications or composite structures yield superior energy storage capabilities.

Table 3.3 Capacitance of various MXene-based symmetric supercapacitors

Electrode	Electrolyte	Capacitance	Ref
$Ti_3C_2T_x$/RGO	PVA- H_2SO_4	90 F/cm^3	[158]
$Ti_3C_2T_x$/PEDOT: PSS	1 M H_2SO_4	90F/cm^3	[159]
$Ti_3C_2T_x$ /CNF	H_2SO_4	90 F/g	[160]
$Ti_3C_2T_x$ /Fe_3O_4/$Ti_3C_2T_x$	1M Li_2SO_4	6.6 mF/cm^2	[161]
α-Fe_2O_3/MXene aerogel	H_2SO_4	182 F/g	[162]
MXene /Graphdiyne nanotube	PVA-H_2SO_4 gel	337.4 F/g	[162]
$Ti_3C_2T_x$/carbon nanofibers/RuO_x	PVA-H_2SO_4 gel	279.4 F/g	[163]
Ti_3C_2/graphite/carbon black/chitin	Biopolymer	100 F/g	[164]
Ti_3C_2Tx MXene/polyaniline	PVA/H_2SO_4	272.5 F/g	[165]
Nb_2C/Ti_3C_2	1M PVA/H_2SO_4 gel	53 F/g	[21]

3.3.2 MXene-based Asymmetric Supercapacitors

Asymmetric supercapacitors have wide voltage windows as compared to SSC [166]. Now, in recent research, MXene-based hybrid materials are used as electrodes, and to avail the properties of both organic and inorganic materials, inorganic-organic hybrids are a good choice [167,168].

Recently, researchers have investigated the design of asymmetric supercapacitors (ASCs), which combine a negative MXene electrode with a positive electrode. Such designs aim to overcome the limitations of symmetric configurations. ASCs offer the benefit of an extended voltage window, resulting from the voltage difference between the two electrode materials. This wider voltage range increases the device's energy density because energy

density is proportional to the square of the voltage window [169,170]. However, finding ideal flexible, positive electrodes compatible with Mxene cathode remains a challenge. To address this, researchers have explored various flexible, positive electrodes.

Xia et al. developed NiO-decorated MXene ($Ti_3C_2T_x$) nanocomposites, referred to as Ni-dMXNC, as illustrated in Figure 3.2(a). The successful deposition of NiO nanosheets onto the surface of MXene layers is evident in Figure 3.2(b). This nanocomposite's NiO benefits from high surface area and reactivity, enhancing capacitance when combined with $Ti_3C_2T_x$ MXene as the negative electrode.

As depicted in Figure 3.2(c), an asymmetric supercapacitor (ASC) was fabricated with Ni-dMXNC used as the positive electrode and $Ti_3C_2T_x$ as the negative electrode. This ASC reached an energy density of 1.04×10^{-2} Wh/cm³ and a power density of 0.22 W/cm³, outperforming symmetric supercapacitors made from $Ti_3C_2T_x$ MXene. The GCD profiles of the Ni-dMXNC//$Ti_3C_2T_x$ ASC at different current densities are shown in Figure 3.2(d). Moreover, Figure 3.2(e) indicates that the device maintained stable cyclic performance over a voltage range of 0 to 1.8 V at 1 A/g, retaining 72.1% of its capacitance after 5000 cycles. These results emphasize the potential of Ni-dMXNC composites for advancing high-performance applications in ASCs, offering enhanced energy and power densities in addition to excellent cyclic stability. [171].

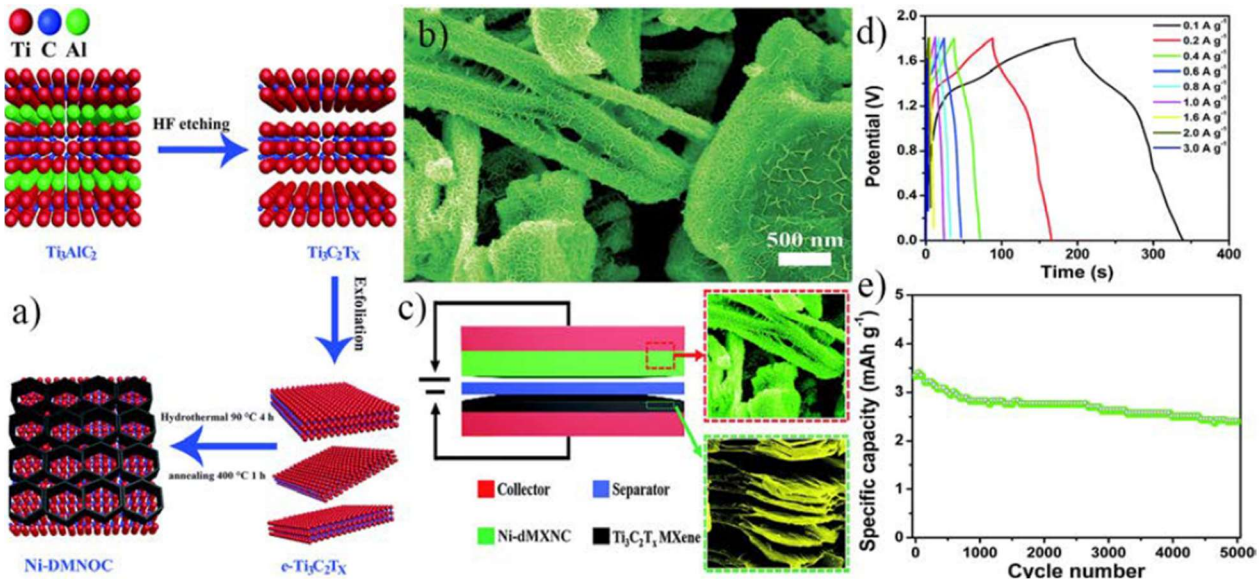

Figure 3.2 (a) Hydrothermal synthesis route of Ni-dMXNC; (b) SEM image of Ni-dMXNC; (c) Schematic of Ni-dMXNC//$Ti_3C_2T_x$ ASC; (d) GCD curves at varying current densities; (e) Cycling performance at 1 A/g.[148]

As depicted in Figure 3.3(a), Fu et al. developed a Ti_2C_x MXene @PANI (GMP) structure encapsulated with graphene. SEM images in Figure 3.3(b)–(d) demonstrate that the inclusion of chemically stable graphene significantly enhances the mechanical integrity of the MXene matrix by providing structural reinforcement. Additionally, the incorporation of conductive polyaniline (PANI) contributes to improved electrochemical performance by introducing additional active sites.

Figures 3.3(e) and 3.3(f) compare the CV and GCD curves for MXene, Ti_2C_x MXene @PANI (MP), and GMP electrodes at a sweep rate of 5 mV/s in 1 M H_2SO_4. The GMP electrode achieved a high specific capacitance of 635 F/g at a current density of 1 A/g and retained 97.54% of its capacitance after 10,000 charge-discharge cycles (Figure 3.3(g)).

Also, an asymmetric supercapacitor (ASC) was fabricated with GMP as the anode and graphene as the cathode, reaching an energy density of 42.3 Wh/kg at a power density of

950 W/kg, while maintaining 94.25% of its capacitance after 10,000 cycles at 10 A/ g [172].

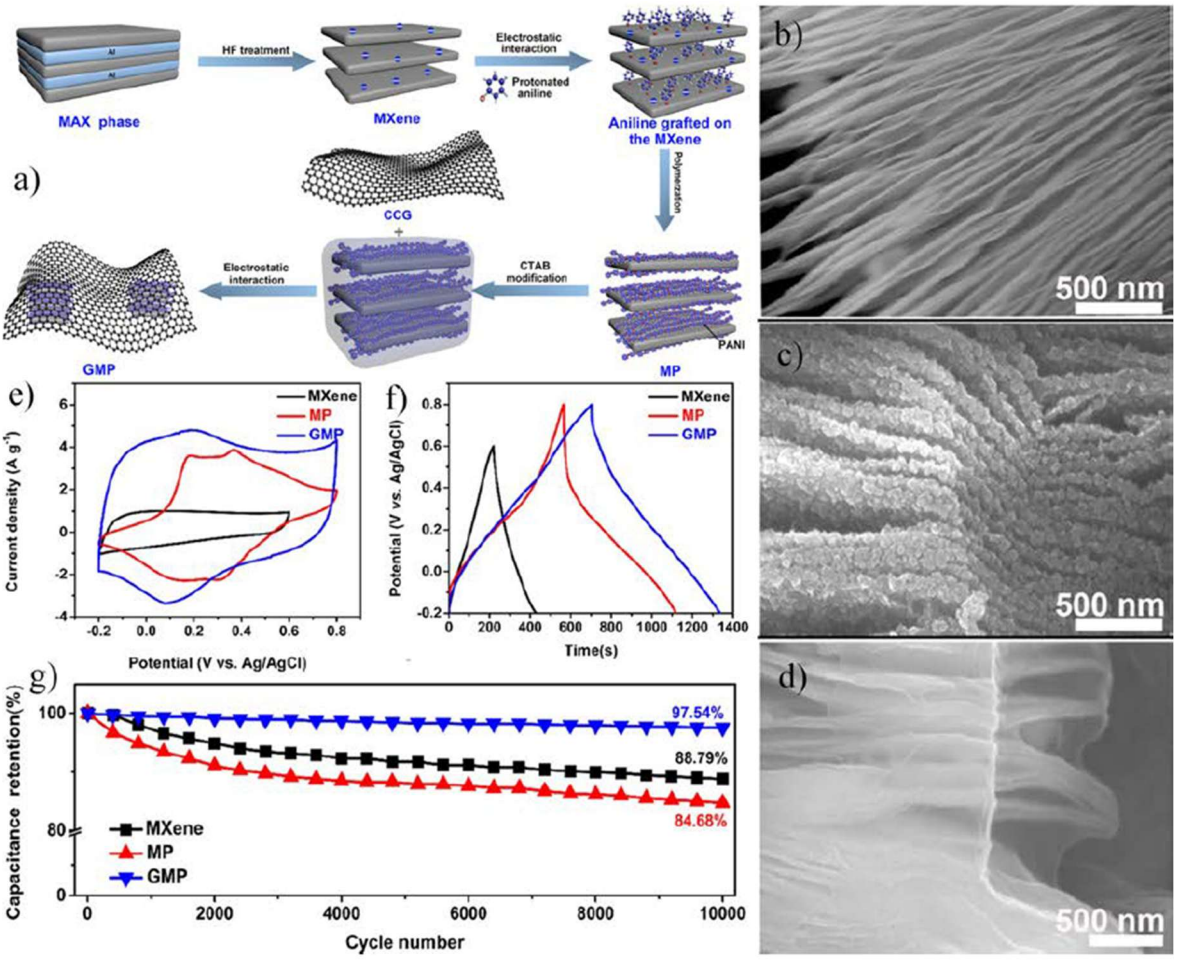

Figure 3.3 (a) Process of fabricating the GMP composite electrode. (b)-(d) SEM images of MXene (e) CV curve of GMP electrode at 5 mV/s in 1 M H_2SO_4; (f) GCD curve at 1 A/g in 1 M H_2SO_4; (g) Cycling stability after 10,000 cycles at 10 A/g[148]

Wang et al [169] prepared self-supporting PANI/MXene films as shown in Figure 3.4(a). The incorporation of polyaniline (PANI) particles into the MXene substrate plays an important role in improving the overall electrochemical performance of the composite material. The nanoscale dimensions of the PANI particles facilitate a highly uniform and

intimate contact with the MXene surface, which maximizes the interaction between the two materials. The nanoscale PANI structure promotes a higher surface area, enabling rapid ion diffusion and charge transfer during electrochemical processes. These synergistic effects contribute to achieving optimal pseudocapacitance, as demonstrated in Figure 3.4(b), which highlights the structural and electrochemical benefits derived from this nanoscale engineering approach. PANI/MXene composite film has a peak volumetric capacitance of 1167 F/cm³ at 5 mV/s scan rate in 1 M H_2SO_4 as shown in Figure 3.4(c). The incorporation of PANI significantly improves the electrochemical performance of the composite electrode, allowing for an extended operating voltage window of up to 0.8 V, as shown in Figure 3.4(d). A fully pseudocapacitive asymmetric supercapacitor (ASC) device was fabricated, using MXene as the negative electrode and a PANI/MXene composite as the positive electrode. The fabricated ASC device had an energy density and power density of 65.6 Wh/L and 1687.3 W/L, respectively. Figure 3.4(e) presents the CV curves comparing the MXene electrode, the MXene/PANI composite electrode, and the MXene//MXene/PANI asymmetric supercapacitor (ASC) at a scan rate of 10 mV/s.

Li et al. [173] developed a $Ti_3C_2T_x$/PEDOT: PSS composite film that demonstrated excellent performance. Three-electrode test results indicated that the composite achieved a volumetric capacitance of 1065 F/cm³ at 2 mV/s in a 1 M H_2SO_4 electrolyte. Figure 3.4(f) shows the CV profiles of the $Ti_3C_2T_x$/P-100-H electrode recorded at various scan rates. An ASC with $Ti_3C_2T_x$/P-100-H//rGO was assembled, using rGO as the positive and $Ti_3C_2T_x$/PEDOT: PSS composite as the negative electrode. This ASC delivers an energy density of 23 mW/cm³ and a high-power density of 7659 mW /cm³. Capable of achieving a voltage of 1.2 V, a single ASC can be connected in series with others to power devices such as light-emitting bracelets, as illustrated in Figure 3.4(g).

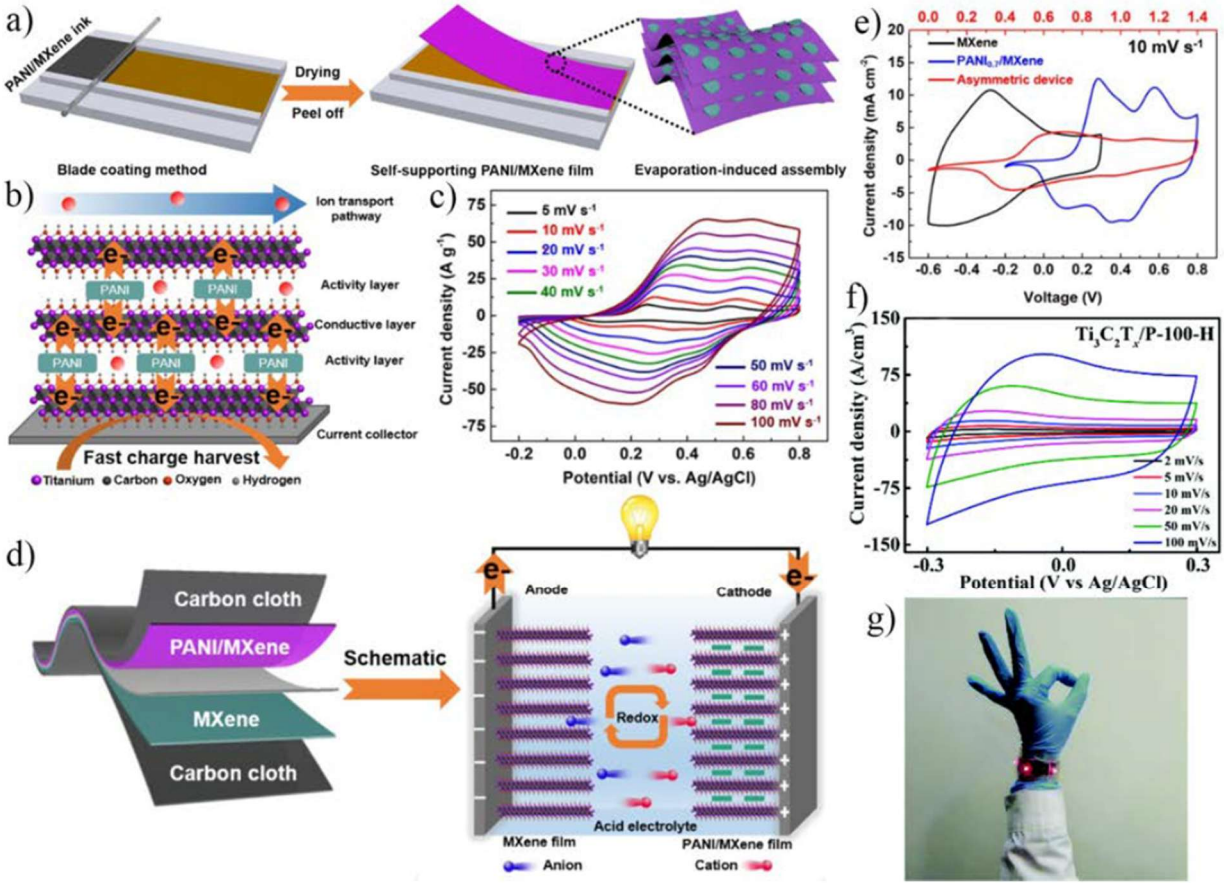

Figure 3.4 (a) Diagram of the MXene/PANI film. (b) Illustration depicting the pathways for ion and electron transport. (c) CV curves for the MXene/PANI electrode captured at various scan rates. (d) Illustration of the MXene//MXene/PANI asymmetric supercapacitor (e) CV curves of MXene, MXene/PANI electrodes, and MXene//MXene/PANI ASC at 10 mV/s, (f) CV profiles of $Ti_3C_2T_x$/P-100-H electrode at different scan rates, (g) Optical image of a wearable bracelet assembled from multiple device components. [148].

Table 3.4 presents a comparative overview of the capacitance values reported for various MXene-based asymmetric supercapacitors, highlighting differences in performance based on electrode composition and configuration.

Table 3.4 Capacitance of various MXene-based asymmetric supercapacitors

Device	Specific Capacitance	Reference
MXene//MnO_2	20.5 F/g at 1.5 A/g	[174]
PANI-MnO_2 // MXene	21.1 F/g at 0.5 A/g	[175]
NiO@MX// copper oxide	73.3 F/g at 10 mA /cm^2	[176]
MXene//CFP	20 F/g	[177]
80 wt% MXene/CNT composite film	50 F/g	[178]
MXene //MoS_2@MXene	29 F/g at 50 mA/g	[179]
CeO_2//$Ti_3C_2T_x$ MXene	122.27 F/g at 1 A/g	[180]
$Ti_3C_2T_x$ // GO/CNT/PANI	117 F F/g at 10 mV/s	[181]
MXene/PANI//AC	262 F/g	[182]
M-$Ti_3C_2T_x$//PANI@M-$Ti_3C_2T_x$	87.3 F/g	[183]
rGO/MXene@$NiCoO_2$// GO/MXene	128.5 F/g at 0.5 A /g	[184]
PANIC//Co-MXene	95.71F/g at 1 A /g	[185]
AC//CoB-V-MX	88.75 F/g at 1 A/g	[186]
CC/MnO_2//CC/MXene-Ppy	75.3 F/g at 10 mV/s	[187]

3.4 Summary

With their high electrical conductivity, layered structure, and adjustable surface chemistry, MXenes are increasingly seen as excellent electrode materials for energy storage. Their versatility makes them suitable for both symmetric and asymmetric supercapacitor configurations. In symmetric supercapacitors, MXenes are employed as both positive and negative electrodes, benefiting from their fast charge/discharge capabilities and stable

cycling performance. In contrast, in asymmetric supercapacitors, MXenes are often combined with complementary electrode materials, such as metal oxides or conducting polymers, to increase the operating voltage window and improve energy density. The investigation focuses on understanding how MXenes perform in these configurations, optimizing their electrochemical properties, and evaluating their practical potential in next-generation energy storage systems.

Chapter 4 Methodology

This section outlines the methods used for device fabrication, detailing each step involved in the experiments. It also highlights the key characterization techniques used to analyze device performance. These experimental methods form the foundation for investigating the research objectives.

4.1 Device Fabrication

In device fabrication, MXene-based efficient electrodes are fabricated for energy storage applications. Further, integrating these engineered electrodes with some compatible high-ionic-conductivity electrolytes would provide a larger extent of both capacitance and energy densities.

4.1.1 Fabrication of Electrodes

Carbon fibers are used as an ideal substrate for active material deposition due to their flexibility, conductivity, and ductility [188]. Before the deposition of electrode material, carbon fibers (CF) were treated in a mixed acid solution and rinsed thoroughly with ethanol and deionized water. The treated carbon fibers were dried in an oven. For deposition on supercapacitor electrodes, the active materials, Activated Carbon, and binder were weighed in a ratio of 8:1:1 and ground with a mortar and pestle to create a fine powder. This powder was mixed with NMP to create a uniform slurry. The slurry was then deposited on two carbon cloth fibers using dip coating and dried on a hot plate at 50°C for half an hour. The step-by-step procedure of the fabrication of electrodes for supercapacitor devices is shown in Figure 4.1.

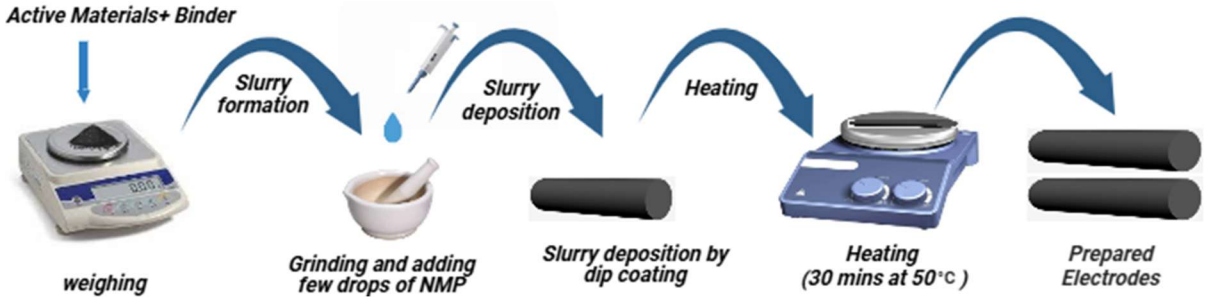

Figure 4.1 Preparation of the Electrode

4.1.2 Preparation of Electrolyte

To prepare an acrylamide-based electrolyte, dissolve 0.2 g of polyvinyl alcohol (PVA) powder in 6 mL of distilled water at 90°C for 1 hour. Mix the resulting PVA solution with 1 mL of glycerol and stir for 10 minutes. Subsequently, 0.0662 g of Irgacure, 1.36 mg of MBA, 1.775 g of acrylamide, and 0.525 g of AMPS are added to the PVA/glycerol mixture. After thorough stirring, the solution is poured into a mold and exposed to UV light to form a gel. The rigid PVA chains aggregated into clusters through crystalline domain interactions, forming the physically crosslinked primary network of the hydrogel. The flexible P(AM-AMPS) chains created the elastic secondary network via chemical crosslinking. Glycerol (Gly) functioned as a bridging crosslinker within the hydrogel matrix, reinforcing the physical crosslinking of the network. Glycerol helps in increasing ionic mobility within the polymer matrix by reducing crystallinity and enhancing amorphous content. AMPS is an ionically active component and a key ionic conductivity enhancer [189]. The step-by-step procedure for the preparation of the electrolyte for supercapacitor devices is shown in Figure 4.2.

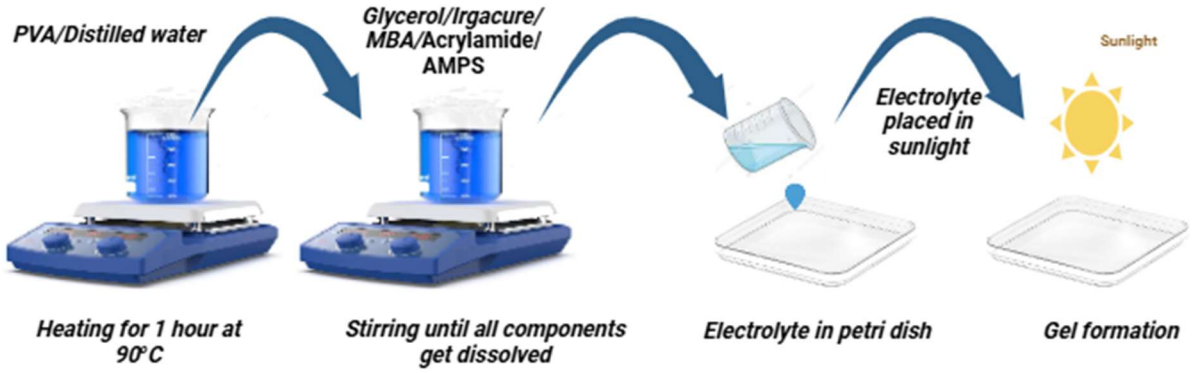

Figure 4.2 Preparation of Electrolyte

4.1.3 Assembly of a Flexible Supercapacitor

Prepared electrodes are placed appropriately and dried on the electrolyte gel. More electrolyte is poured and kept in sunlight until gel formation. Figure 4.3 illustrates the prepared device.

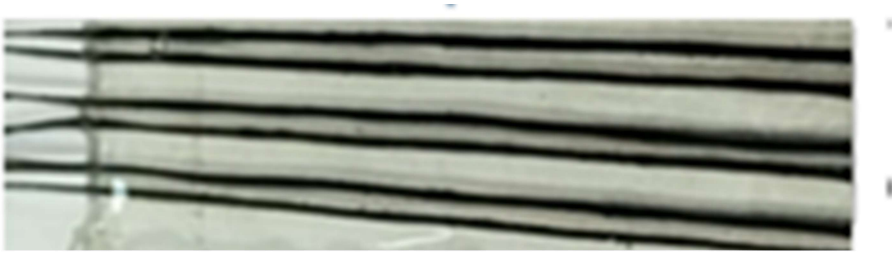

Figure 4.3 Fabricated Supercapacitor

4.2 Testing and Characterization of the Fabricated Devices

The devices can also be tested and characterized using various techniques. Electrochemical analysis and structural and morphological tests can be employed as methods. Structural and morphological features can be obtained from SEM and XRD. Different techniques, including cyclic voltammetry (CV), electrochemical impedance spectroscopy (EIS), and galvanostatic charge-discharge (GCD), are used to assess electrochemical properties.

4.2.1 X-ray Diffraction

X-ray diffraction (XRD) effectively analyzes the crystallographic structure of materials, determines distinct phases, and assesses various structural features. It operates on the principle of X-ray scattering, which occurs when X-rays interact with a material. X-rays are a type of electromagnetic radiation with wavelengths typically between 0.01 and 10 nanometers. These wavelengths are perfectly suited to interact with the spacing between atoms in a crystal lattice, making XRD an essential method for studying the structure of solid materials [190]. Figure 4.4 shows the schematic of the XRD instrument.

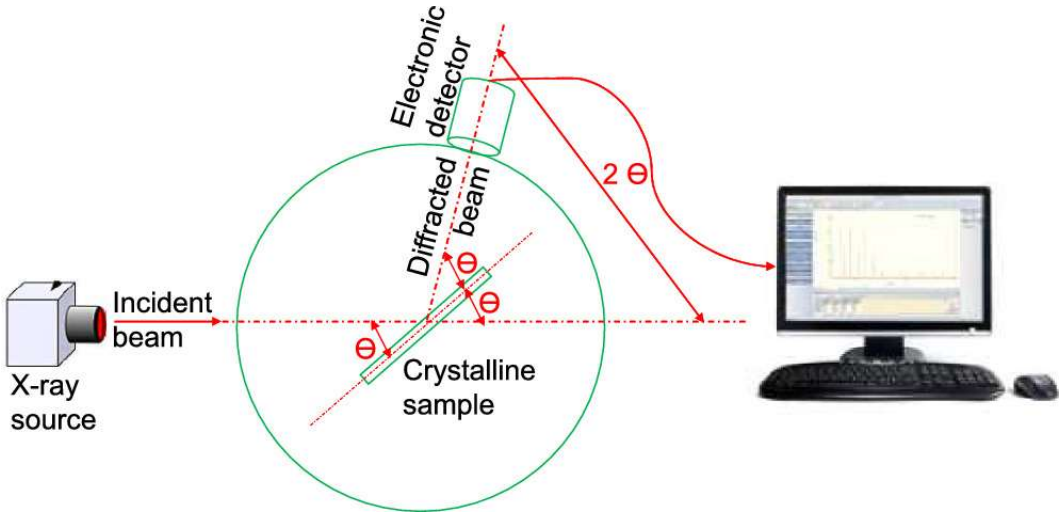

Figure 4.4 XRD instrument schematic[191]

This technique is utilized in fields of material science, chemistry, and engineering to characterize crystalline materials, detect impurities, and determine crystallite size, making it essential for research and industrial applications.

4.2.2 Scanning Electron Microscopy (SEM)

Scanning electron microscopy (SEM) is one of the most essential tools used for examining and analyzing a sample's chemical composition and microstructure morphology [192]. By focusing electron beams on a sample, SEM generates detailed surface images. When electron beams interact with a sample, they emit signals that offer crucial insights into the

surface's composition and texture. SEM is an effective tool for the analysis of organic and inorganic materials at micrometer and nanometer scales. Modern SEM systems offer magnification capabilities of up to 300,000x or more. The machine utilizes a high-energy electron beam as a probe to analyze surface morphology. Inside the electron gun, a tungsten filament functions as the cathode, facilitating thermionic emission to produce a high-energy electron beam (30 keV, ~3 A) within a vacuum chamber. The SEM system consists of an electron gun, electromagnetic lenses, scan coils for beam deflection, electron detectors, a sample chamber, and a computer system with a display and keyboard for controlling the electron beam. Figure 4.5 illustrates the design and operation of the SEM.

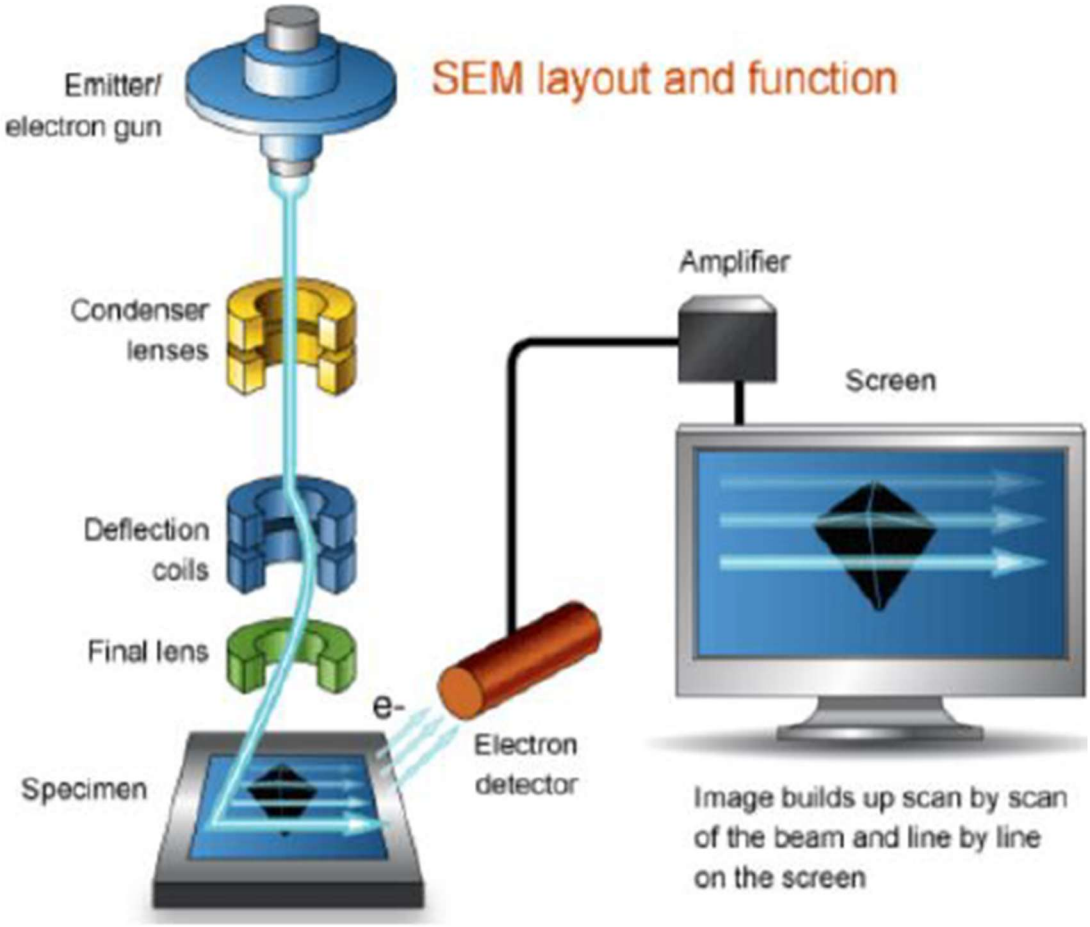

Figure 4.5 SEM Layout [193]

4.2.3 ASMEC Electro-Physical Characterization System

ASMEC is a powerful tool that is used for current-voltage analysis. Current-voltage analysis is performed to accurately map the characterization and efficiency of supercapacitors. This helps in assessing the quality of the supercapacitor material and film [194]. It is also important to see the impact of the contacts and the device assembly on the performance. The current-voltage analysis relationship is given by Equation 4.1.

$$\mathbf{I} = \boldsymbol{V}/\boldsymbol{R} \qquad \textbf{(4.1)}$$

Where **I** stands for current, **V** represents voltage, and **R** corresponds to resistance.

4.2.4 Cyclic Voltammetry (CV)

Cyclic voltammetry (CV) is an electrochemical technique used to analyze the charge storage characteristics, specific capacitance, and durability of flexible supercapacitors. During CV, the potential (voltage) applied to the supercapacitor is varied linearly over time between two defined values, called preset limits. This sweep can occur in both the forward and reverse directions, creating a cyclic pattern. The scan rate, typically measured in volts per second (V/s), determines how quickly the voltage is varied. A slow scan rate allows more time for ion diffusion, while a faster scan rate is useful for studying capacitive behavior. Common scan rates in CV experiments for supercapacitors range from 5 to 200 mV/s, depending on the used material and system being studied. As the voltage is varied, the system's current response is measured. The resulting current-versus-voltage (I-V) plot is the required CV curve, which provides insight into the electrochemical properties of the supercapacitor. Capacitance can be calculated by integrating the area under the CV curve [195- 197]. Figure 4.6 illustrates a typical cyclic voltammetry (CV) curve.

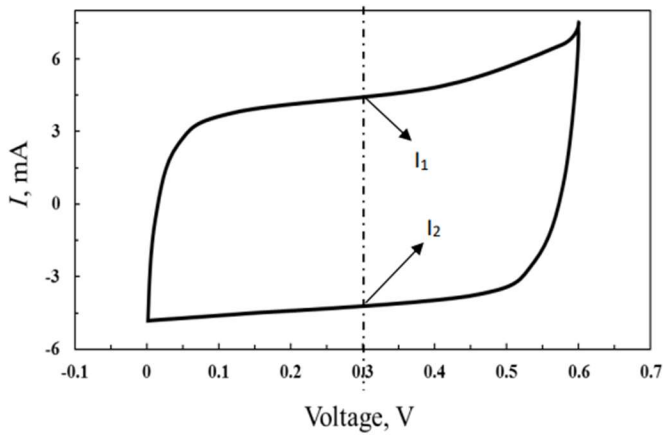

Figure 4.6 Typical CV curve [198]

4.2.5 Galvanostatic Charge-Discharge (GCD)

The Galvanostatic Charge Discharge (GCD) rate is a principal electrochemical technique to evaluate supercapacitors. Secondly, this method is to provide a constant current to the supercapacitor and to measure the variation of voltage with time. The GCD curve gives the measurement of capacitance, internal resistance, cyclic stability, and the efficiency of the supercapacitor device. The charging process starts by applying a predetermined potential. Subsequently, the current is inverted to initiate the discharge phase. At the moment of current reversal, a distinct voltage drop, known as the IR drop, is observed, arising from the inherent internal resistance, as shown in Figure 4.7. In our work, GCD curves were used for charge and discharge time estimation. The stability performance of supercapacitor devices is also measured from hundreds of GCD cycles. GCD measurements under several current densities are used to evaluate the supercapacitor's ability to be charged and discharged quickly. The decrease in specific capacitance of the supercapacitor with the increase in current density indicates limitations in ion transport and electrode material

properties. If the profile of GCD is close to the same for different numbers of cycles, it means that it has good cyclic stability and is highly necessary for practical applications.

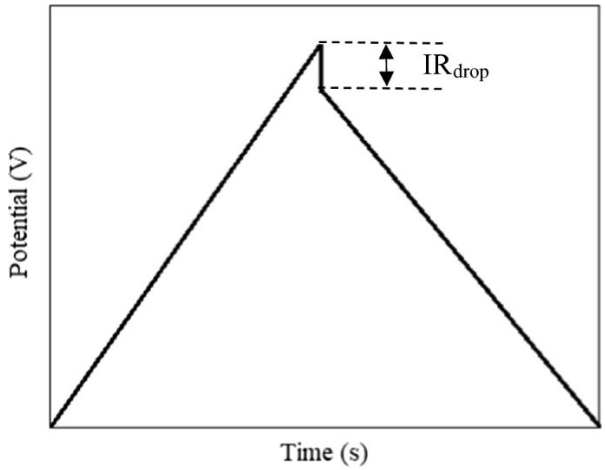

Figure 4.7 Typical GCD curve[199]

4.2.6 Electrochemical Impedance Spectroscopy

Electrochemical impedance spectroscopy (EIS) is an electrochemical technique used to determine key parameters and characteristics of different electrical circuit components. [200-203]. In EIS, an AC-sinusoidal signal with a small potential in a broad frequency band is used, and the current response is measured. EIS is a non-destructive technique used to investigate an electrochemical system. The potential magnitude applied is small enough that it does not disturb the equilibrium state of the system during measurement. EIS-based Nyquist and Bode plots will be regarded as key metrics for characterizing the internal electrical parameters of supercapacitors [204]. The Nyquist plot displays the real part of impedance (ZRe) on the x-axis and the negative imaginary part (-ZIm) on the y-axis. In a standard EDLC supercapacitor, this plot usually shows a semicircle at high frequencies, a sloped line at mid-range frequencies, and an almost vertical line at low frequencies, as shown in Figure 4.8.

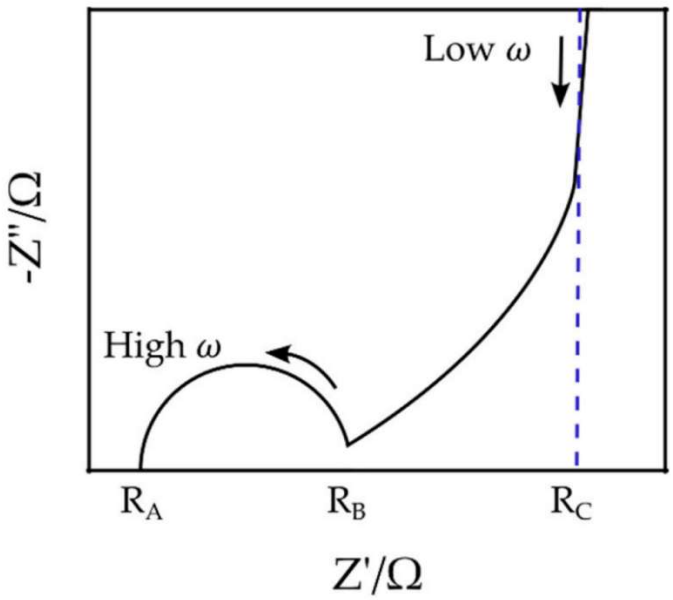

Figure 4.8 Schematic of a typical Nyquist plot for EDLC supercapacitors [205]

The Nyquist plot does not explicitly display frequency information, which can sometimes be useful. To address this issue, a Bode plot is used. An impedance-based Bode plot is between the frequency and impedance(Z) [206]. This plot illustrates how the overall impedance trend varies with frequency. In a phase difference-based Bode plot, the x-axis represents frequency, and the y-axis displays the phase angle. The phase difference between voltage and current represents the magnitude of the phase angle. The derivation of capacitance from EIS depends on the conventional method of deriving capacitance from the imaginary component of impedance (ImZ), as shown in Equation 4.2 [201], where f is the frequency.

$$\boldsymbol{C = -\frac{1}{2\pi f\, Im(Z)}} \qquad \textbf{(4.2)}$$

4.3 Summary

In our work, we fabricate electrodes for flexible supercapacitor devices by applying slurry to carbon cloth and then immersing the electrodes in a gel-based electrolyte. After the fabrication process, we utilize various testing and characterization techniques, including cyclic voltammetry (CV), galvanostatic charge-discharge (GCD), and electrochemical impedance spectroscopy (EIS), to assess their performance in terms of charge storage capacity, stability, and overall efficiency.

Chapter 5 Experiments, Results, and Discussion

This study focuses on designing and fabricating a range of electrodes by modifying the composition of MXenes, including pure MXenes, MXene composites, and electrodes with varying levels of MXene impurities. This careful adjustment of tailored electrodes allows us to investigate how material composition affects electrochemical performance in energy storage applications. We fabricate and assemble symmetric and asymmetric supercapacitors by utilizing these specialized electrodes. In symmetric devices, both electrodes comprise the same MXene-based materials, whereas asymmetric devices employ distinct electrode materials for the anode and cathode.

To evaluate the performance of fabricated devices, we employ multiple characterization techniques.

- **Cyclic voltammetry (CV):** Determines specific capacitance and energy density.
- **Galvanostatic charge-discharge (GCD):** Analyzes the charge-discharge time profiles and evaluates the cyclic stability of the system.
- **Electrochemical impedance spectroscopy (EIS):** Calculate series resistance and charge transfer resistance.
- **Structural analysis:** Methods such as X-ray diffraction (XRD) and scanning electron microscopy (SEM) evaluate material morphology and crystallinity.

Figure 5.1 presents a flowchart illustrating the fabrication and evaluation process of the supercapacitors developed in this study.

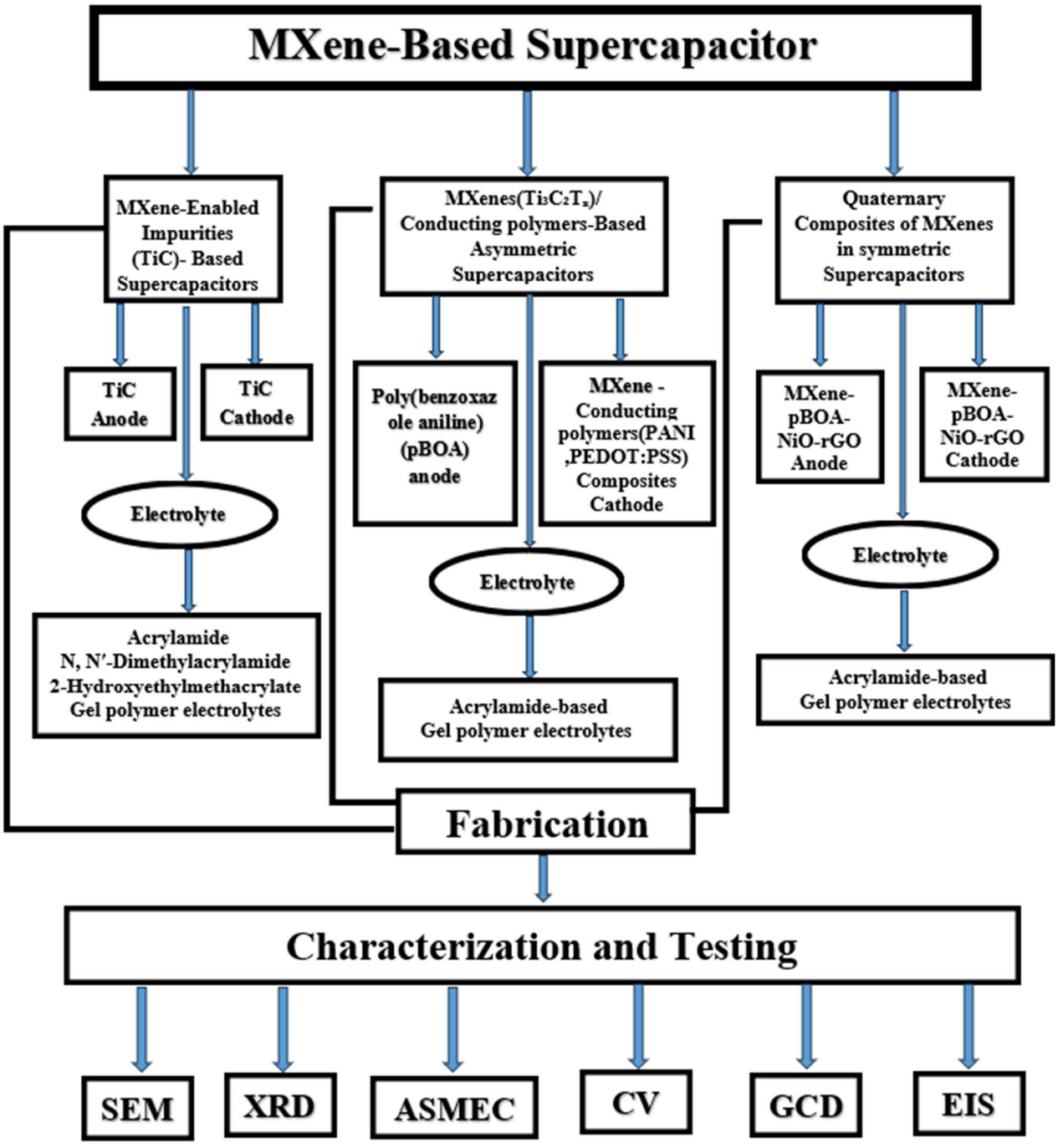

Figure 5.1 Flowchart of the fabrication and testing of supercapacitors designed in our work

5.1 MXene-Enabled Impurities (TiC) -based Supercapacitors

Five different electrodes are prepared with varying TiC (MXene-Enabled Impurities) content, and symmetric supercapacitors are fabricated using three electrolytes: acrylamide, N, N′-Dimethylacrylamide, and 2-hydroxyethyl methacrylate, to achieve flexibility and improved energy storage. Before the electrode fabrication, all samples are tested using X-ray diffraction (XRD) analysis. In this study, TiC-based electrodes are incorporated into an acrylamide-based electrolyte. [189]. Two novel electrolytes are developed by replacing Acrylamide with N, N′-Dimethylacrylamide and 2-Hydroxyethyl methacrylate. TiC-based electrodes show excellent specific capacitance, greater flexibility, and superior energy storage performance when paired with these advanced electrolytes.

5.1.1 Experimental Details

To prepare the acrylamide-based electrolyte, dissolve 0.2 g of PVA in 6 mL of distilled water at 90°C for 1 hour, then mix with 1 mL of glycerol and stir for 10 minutes. Add 0.0662 g Irgacure, 1.36 mg MBA, 1.775 g acrylamide, and 0.525 g AMPS, and stir until fully dissolved. Pour the solution into a mold and cure under UV light to form the gel [189]. Then, two novel electrolytes were prepared by replacing Acrylamide with *N*, *N′*-Dimethylacrylamide and 2-Hydroxyethyl methacrylate. Polyvinylidene Fluoride (PVDF) particles, activated carbon, and N-methyl pyrrolidone (NMP) solvent were purchased from Sigma Aldrich, while TiC was obtained from Shanghai Alladin Biochemical. To prepare the supercapacitor electrodes, TiC, activated carbon, and PVDF were weighed and then ground using a pestle and mortar into a fine powder. NMP was added to the powder to create a homogeneous slurry, which was then applied to two carbon cloth fibers via dip coating. The coated fibers were dried for half an hour on a hot plate. After proper placement

and drying, additional electrolyte was poured onto the fibers and exposed to sunlight until gel formation occurred. Once the electrolytes were dried, the supercapacitors were sealed with a polymer sheet. Carbon cloth-based supercapacitors are cost-effective, highly conductive, and mechanically robust, enhancing device flexibility [207-209].

Five pairs of electrodes were prepared using the same procedure with different contents of TiC and Activated Carbon, as shown in Table 5.1.

Table 5.1 Electrode configuration

Sr. No	**Samples**	**Activated Carbon(g)** *AC*	**TiC (g)** *MXene-enabled impurities*	**PVDF(g)** *Binder*	**Net mass (g)**
1	S1	0	0.10813	0.00983	0.11796
2	S2	0.004915	0.103215	0.00983	0.11796
3	S3	0.00983	0.0983	0.00983	0.11796
4	S4	0.05895	0.04915	0.00983	0.11796
5	S5	0.10813	0	0.00983	0.11796

The Activated Carbon/TiC mixture with contents (in the ratio of x,0.10813-x) was named S1, S2, S3, S4, and S5, respectively. PVDF was used as a binder, and NMP was used as a solvent for slurry preparation. Then, electrodes with the same configuration were placed on as-fabricated electrolytes and labeled as E1, E2, and E3, respectively.

5.1.2 Results And Discussion:

5.1.2.1 X-Ray Diffraction Analysis (XRD)

The phase changes and crystallinity of the as-synthesized samples, as shown in Table 5.1, are analyzed using X-ray diffraction (XRD). The analysis is conducted at 2θ values ranging from 5° to 80°. From Figure 5.2, diffraction peaks observed at 35.912°, 41.707°, 60.454°, 72.360°, and 76.132° correspond to the characteristic reflections corresponding to the

(111), (200), (220), (311), and (222) crystal planes, respectively [135]. All samples show different intensities at specified angles due to the addition of activated carbon.

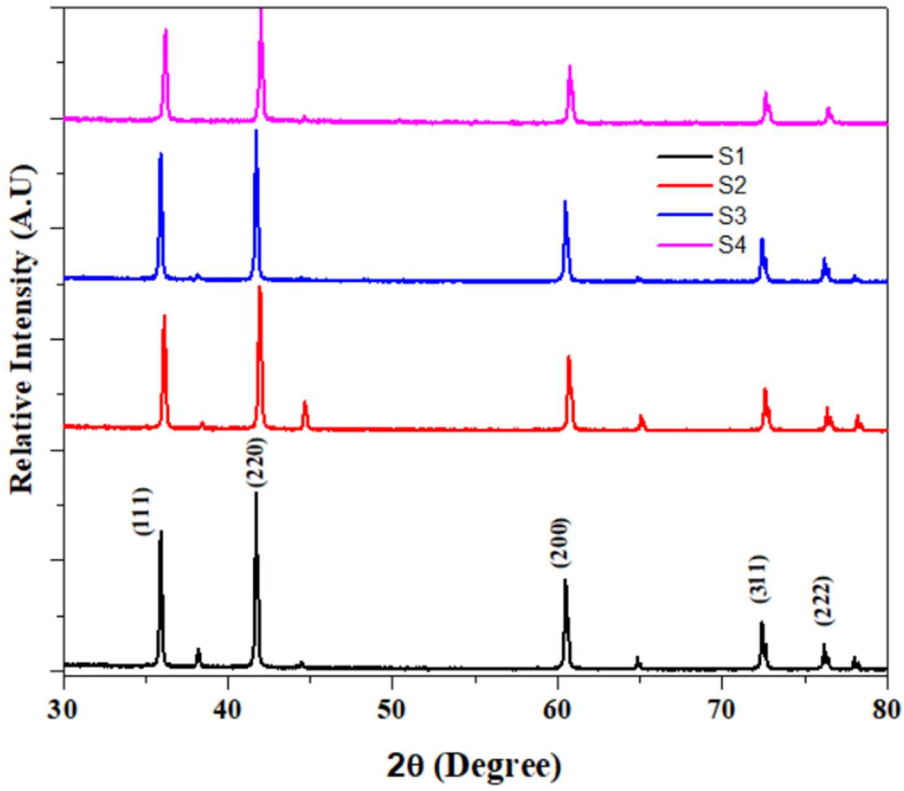

Figure 5.2 XRD pattern of MXene-enabled electrode material featuring TiC (titanium carbide) impurities

Electrochemical characteristics of the fabricated supercapacitors are analyzed using multiple techniques, including Electrochemical Impedance Spectroscopy (EIS), Cyclic Voltammetry (CV), and charge-discharge tests conducted under both open-circuit and short-circuit conditions. These methods enable the evaluation of critical parameters such as capacitance, internal resistance, and charge transfer behavior. By employing these analytical techniques, a comprehensive insight into the supercapacitor's overall performance, stability, and efficiency is obtained.

5.1.2.2 Cyclic Voltammetry

While performing a CV, a voltage-dependent current curve is generated by applying a potential (V) at a constant rate over time (t) [63]. The voltage window and starting point of CV curves are two key factors that influence specific capacitance and Faradic losses in supercapacitors. In our study, the fabricated supercapacitors (Table 5.1) are tested with a multimeter after fabrication. For a quick check to see if the supercapacitor has been properly fabricated, it is connected to a conventional ohmmeter for an initial inspection. During current-based transient analysis of any capacitor, the current magnitude decreases over time. As the current drops, the resistance value increases from a lower to a higher level. This indicates that if the supercapacitor is successfully fabricated, the resistance measured by the ohmmeter should gradually increase. While this early inspection provides a rapid assessment, it can also generate parasitic voltages on the electrodes, which may cause issues during CV measurements. To prevent problems caused by testing the supercapacitor with an ohmmeter (which involves an internal battery effect in the circuitry), it is essential to properly discharge the supercapacitor by shorting both electrodes before conducting CV [210]. It means that the voltage on the supercapacitor should be zero before performing CV to minimize losses while performing calculations of specific capacitance. In our work, CV is performed at three scan rates, i.e., 10mV/s, 50mV/s, and 100mV/s. As shown in Figure 5.3, the voltage-time curve exhibits a higher slope at a high scan rate than at lower scan rates. At a high scan rate, the voltage increases more rapidly, allowing the maximum voltage to be attained in a shorter time compared to a low scan rate. This occurs because, at higher scan rates, there is fast charge and discharge, limiting the time available for ion diffusion within the electrode material. Consequently,

the electrochemical reaction kinetics dominate the process, leading to a swift rise in voltage.

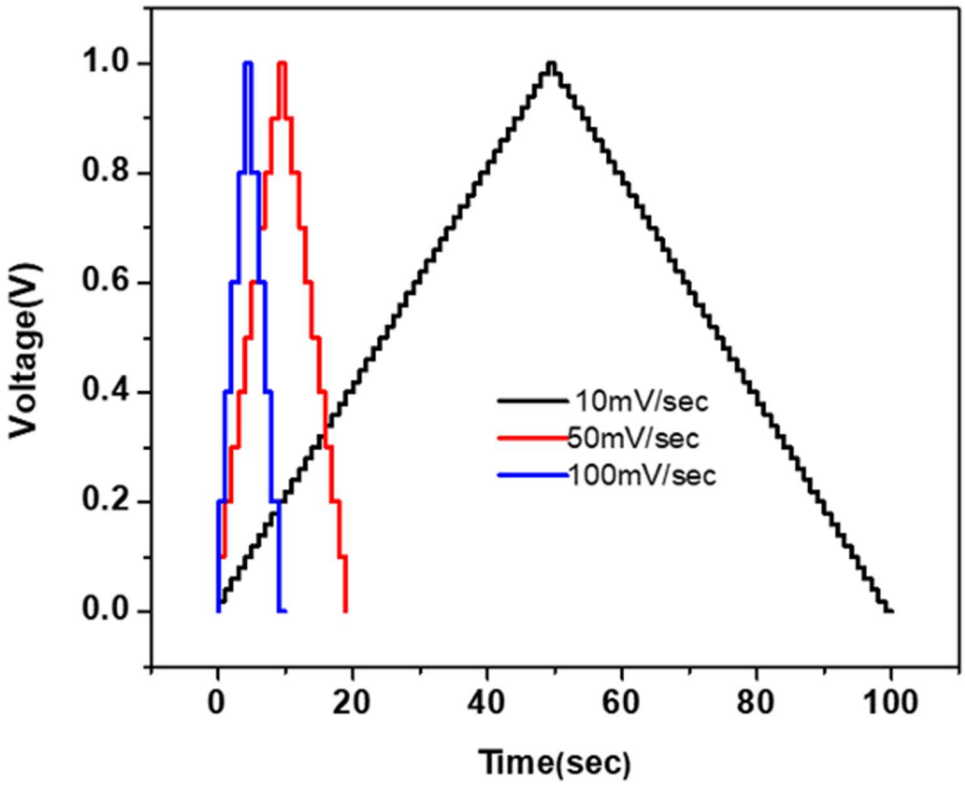

Figure 5.3 Conceptual framework of scan rates for Cyclic Voltammetry

Cyclic voltammetry is conducted within a potential window ranging from -1 V to 1 V. As reported in the literature, the specific capacitance (Cs) of symmetric supercapacitors can be calculated from the CV curve using the formula given in Equation 5.1 [211,212]. In this equation, *m* represents the active mass of material on both electrodes (40.8 mg), *v* denotes the scan rate (10 mV/s, 50 mV/s, and 100 mV/s), *Vi* shows the initial voltage (-1 V), *Vf* represents the final voltage (1 V), *I* corresponds to the current from *Vi* to *Vf*, and ΔV represents the potential window (2 V) [163,213].

$$\boldsymbol{Cs = 4 \times \int_{Vi}^{Vf} \frac{I}{mv\Delta V}\, dV} \qquad \textbf{(5.1)}$$

The energy density (E) can be determined using Equation 5.2, where Cs represents the specific capacitance.

$$\boldsymbol{E = \frac{0.5 \times Cs \times (\Delta V)^2}{3.6}} \qquad \textbf{(5.2)}$$

Figure 5.4 shows the CV curves from our study, measured within a potential window of -1V to 1V at scan rates of 10 mV/s, 50 mV/s, and 100 mV/s. These curves illustrate the supercapacitor's electrochemical behavior at different scan rates, helping to assess variations in current response and charge storage. The CV curves are used to calculate specific capacitance and energy density, as outlined in Equations 5.1 and 5.2.

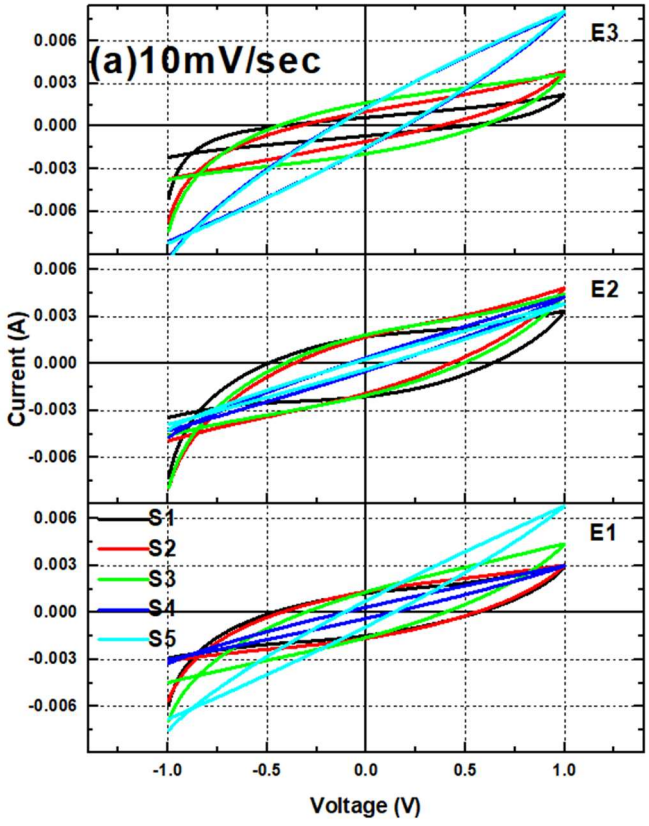

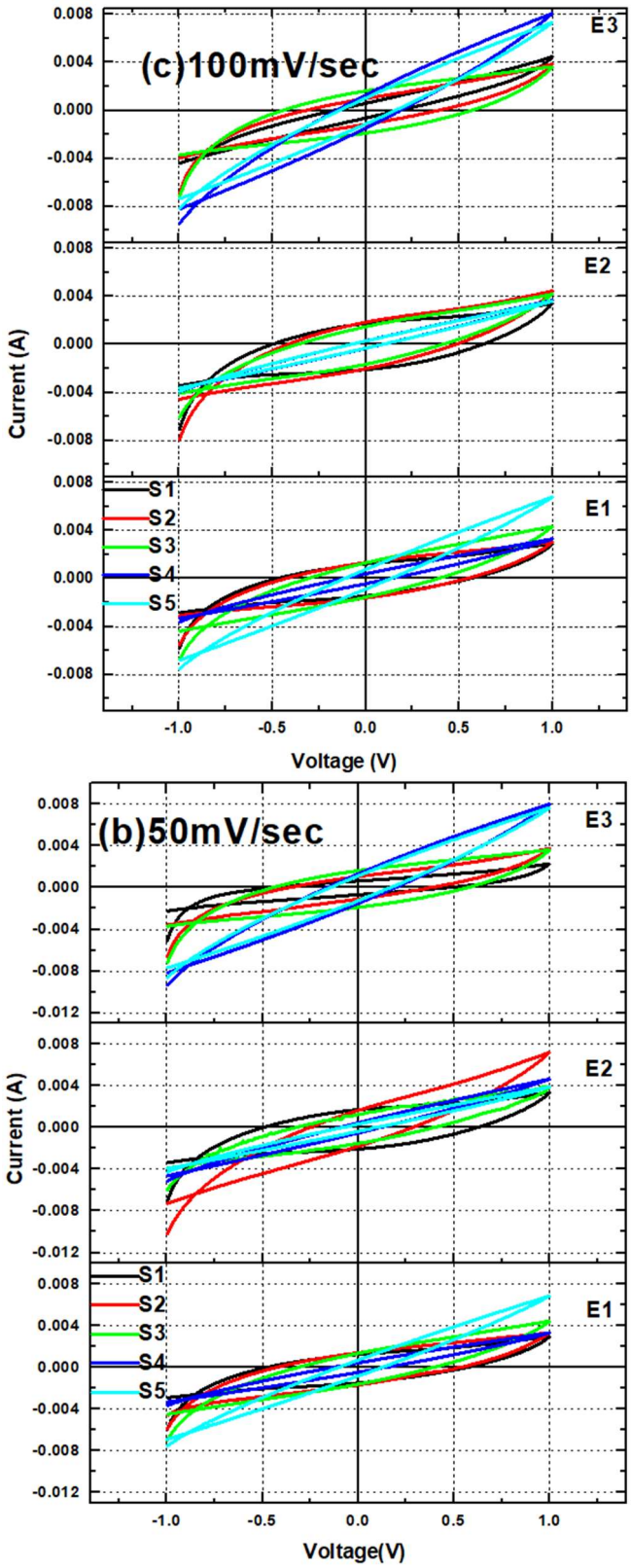

Figure 5.4 CV curves within a potential range of -1V to 1V at varying scan rates: (a) 10 mV/s, (b) 50 mV/s, and (c) 100 mV/s

The specific capacitance of a material decreases as the scan rate increases in electrochemical measurements. This inverse relationship arises due to variations in electrolyte penetration into the electrode material. At lower scan rates, electrolyte ions have sufficient time to diffuse deeply into the porous structure or nanosheets of the electrode, maximizing the utilization of the active surface area and facilitating more electrochemical reactions.

Consequently, this enhances the specific capacitance observed in CV curves. In contrast, at higher scan rates, the limited time for ion diffusion restricts electrolyte access to deeper regions of the electrode. As a result, the active material is not fully utilized, leading to a reduction in the measured specific capacitance [214]. Therefore, optimizing electrode porosity and ion transport pathways is essential for maintaining performance at high scan rates.

Figure 5.5 compares the specific capacitance and energy densities of all supercapacitors in three different electrolytes at different scan rates. The comparison is made for three different electrolyte types, showing how electrolyte choice impacts performance. The supercapacitor using 2-Hydroxyethyl methacrylate-based electrolyte (E3) shows a specific capacitance of 79 F/g for sample S4 at 10 mV/s. In contrast, the supercapacitor with an *N*-*N*′ Dimethylacrylamide-based electrolyte (E2) exhibits a specific capacitance of 50 F/g for sample S2 at the same scan rate.

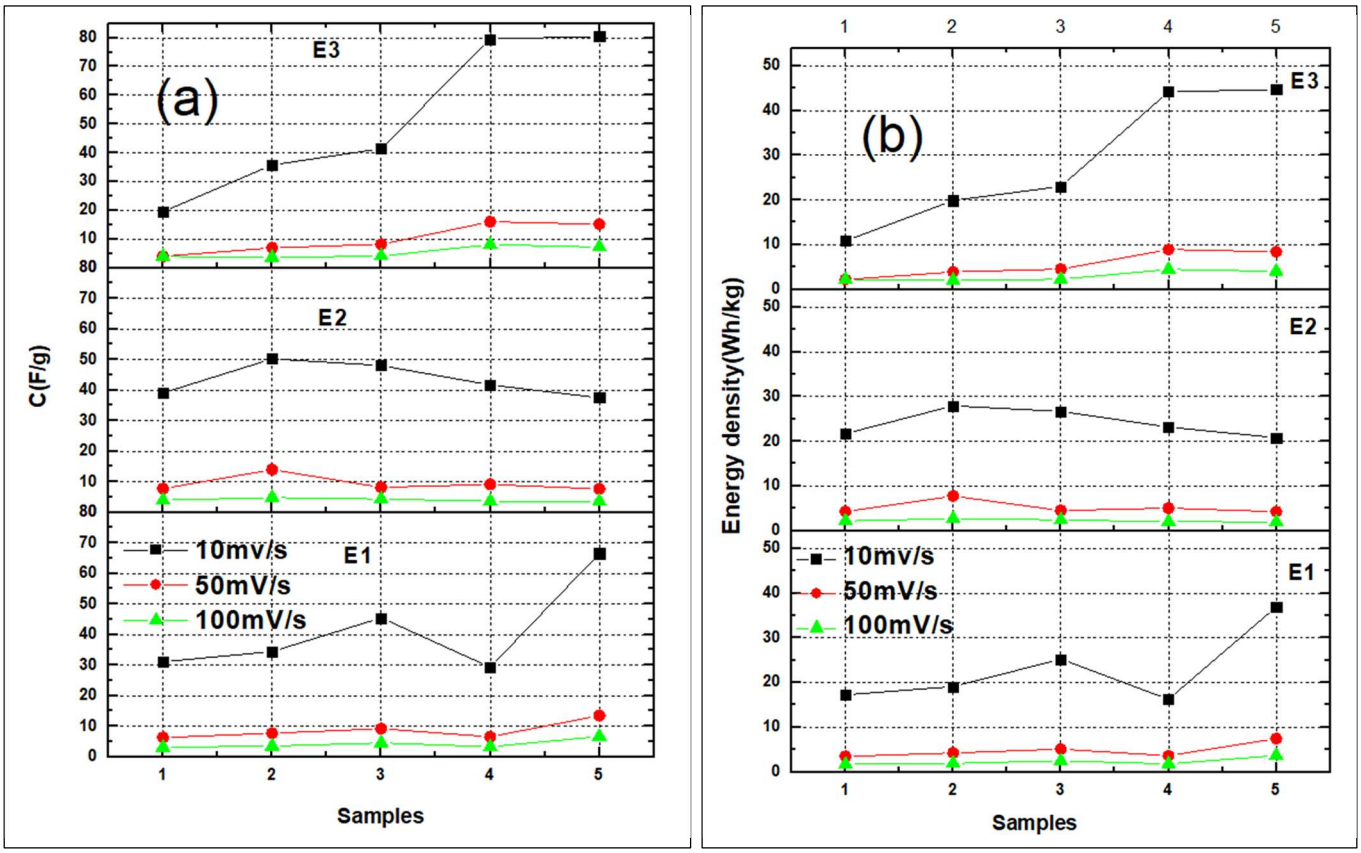

Figure 5.5 (a) Specific Capacitance (b)Energy density of fabricated supercapacitors at different scan rates

5.1.2.3 Electrochemical impedance spectroscopy (EIS)

Randles circuit shown in Figure 5.6 is evaluated in EIS analysis. This circuit model is represented by AC circuit elements, including resistors and capacitors. This model helps in understanding charge transfer kinetics, diffusion processes, and overall electrode–electrolyte interactions.

The Randles model incorporates Rs, Ret, and Cnf in a specific configuration. Here, Rs represents the series resistance, Ret denotes the electron transfer resistance at the interface of the electrode and electrolyte, and Cnf represents the non-Faradaic capacitance originating from the electrode surface.

In Figure 5.6(a), the circuit is evaluated with a non-Faradic process. In a non-Faradic process, all charge is accumulated on the non-Faradic capacitor. In Figure 5.6 (b), the circuit is with the faradic process in which capacitance offers infinite impedance, so all current passes through *Ret.* [200].

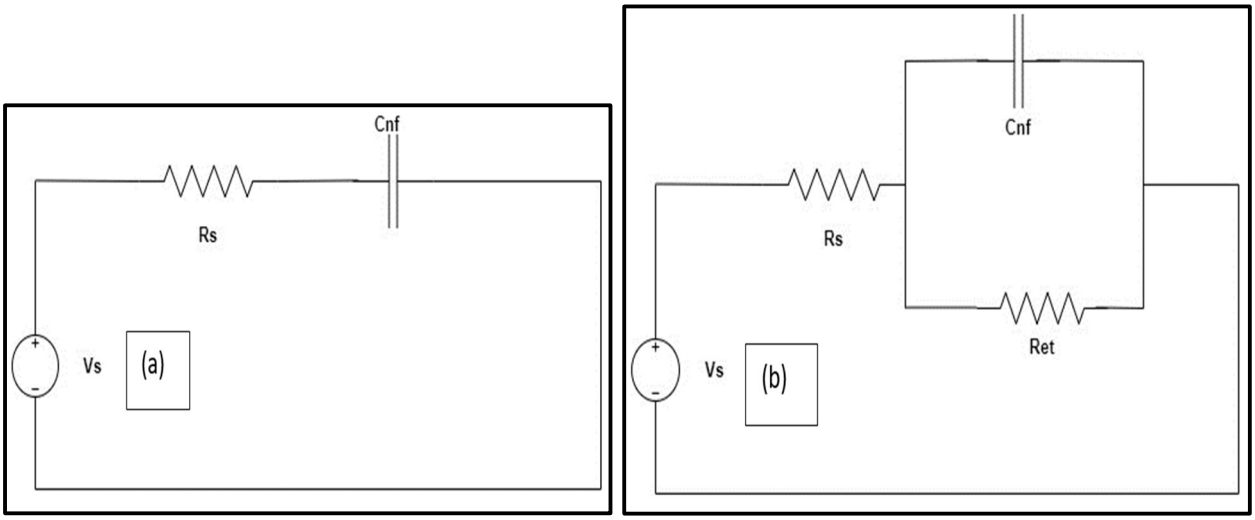

Figure 5.6 Randles circuit (a) Non-faradic process (b) Faradic process

EIS is used to examine the internal electrical parameters of supercapacitors through the two-probe method. The two-probe configuration measures the combined impedance of both electrodes and the electrolyte. In this method, the anode and cathode are connected during the analysis, and a small alternating current signal is applied over a range of frequencies. The initial operating conditions were maintained constant, with a pretreatment time of 5 seconds, an alternating current (AC) amplitude of 0.01 V (Vac), and a variable frequency from 0.1 Hz to 10 kHz at a charging voltage of 1 V DC. Nyquist and Bode plots (both impedance- and phase-based) are employed to determine the values of the circuit elements.

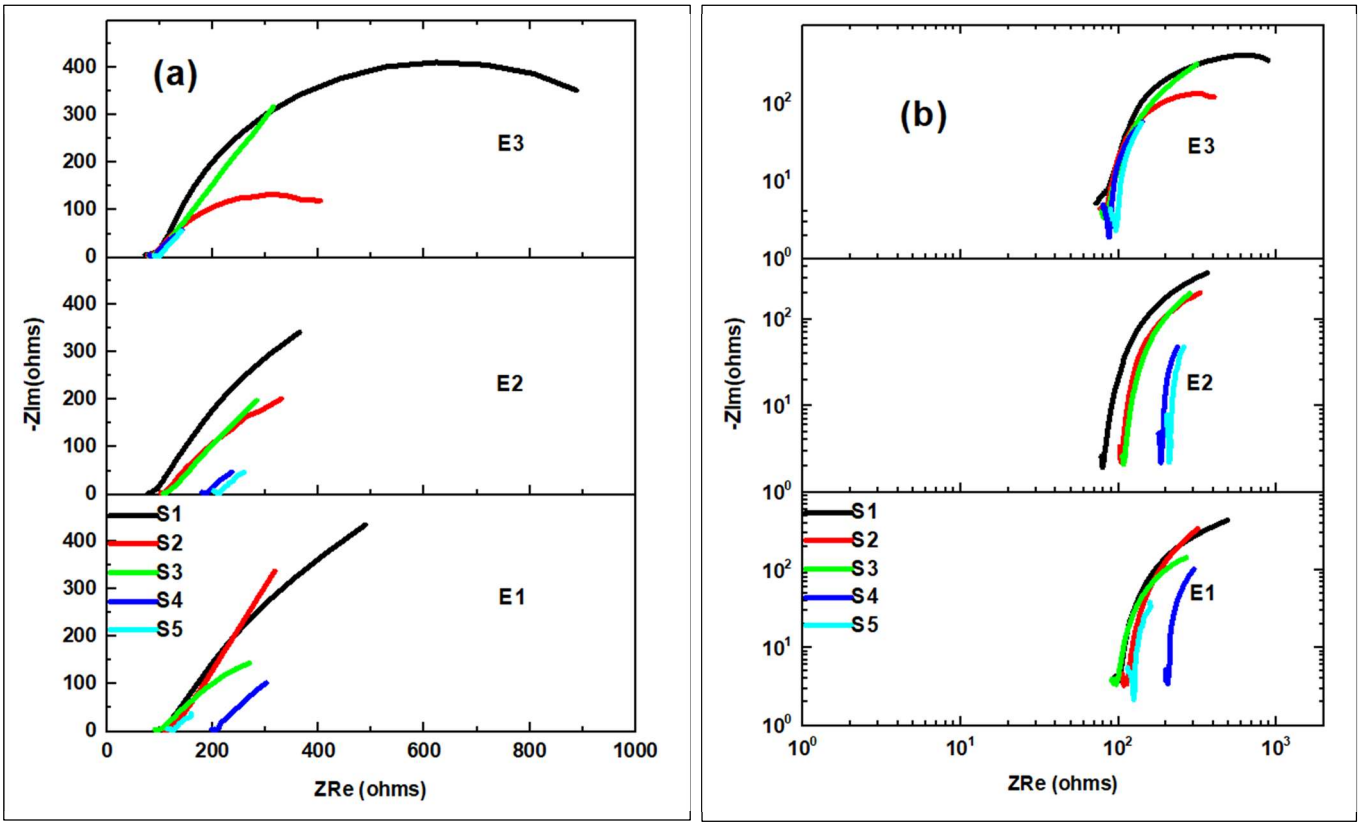

Figure 5.7 Nyquist plot at 1V (a) normalized scale (b) logarithmic scale

The Nyquist plot is a key parameter in Electrochemical Impedance Spectroscopy (EIS) analysis, providing critical insight into the electrochemical behavior of energy storage devices like supercapacitors. It graphically represents the complex impedance, plotting the real component (Z') on the x-axis and the imaginary component (Z'') on the y-axis. This plot helps distinguish various resistive and capacitive elements within the system. A Nyquist plot reveals information about internal resistance, electrode/electrolyte interface quality, and ion transport efficiency. Thus, the Nyquist plot is essential for diagnosing performance bottlenecks and guiding material or design improvements in supercapacitors.

The x-axis offers critical insights into the magnitudes of series resistance (Rs) and electron transfer resistance Ret (Rp) [215]. If we consider the supercapacitor as ideal, the series resistance (Rs) is assumed to be zero, while the electron transfer resistance (parallel resistance, Ret) is considered infinite. [216]. However, these considerations do not apply to real supercapacitors. Figure 5.7 shows the Nyquist plot in both normalized scale and logarithmic scale. Table 5.2 shows the Rs value for all supercapacitors at 1V, evaluated from the Nyquist plot. These results show positive and negative features of resistance for the better operation of supercapacitors. For optimal supercapacitor performance, the electron transfer resistance (Ret) should be as high as possible, while the series resistance (Rs) should be minimized to near zero [217]. In Figure 5.6 (a), the Nyquist plot indicates that the electron transfer resistance (Ret or Rp) is not observed within the frequency range used for the EIS measurements, as evidenced by the incomplete semicircle. This suggests that the selected frequency range is insufficient to capture the full electrochemical behavior of the system, particularly the characteristics associated with Ret. To thoroughly examine the EIS spectra and accurately evaluate Ret, a broader frequency range should be employed, extending both to lower and higher frequencies. This adjustment would ensure that the semicircle in the Nyquist plot is fully resolved, providing a more comprehensive understanding of the impedance characteristics of the supercapacitor. It is shown in Table 5.2 that in all electrolytes, Sample S1, made entirely of titanium carbide (TiC), shows the lowest series resistance (Rs), highlighting its superior conductivity and minimal resistive losses. Rs is a crucial figure of merit in electrochemical impedance spectroscopy (EIS) as it directly impacts the performance of supercapacitors, particularly their energy efficiency and power delivery. When the proportion of TiC in the sample is reduced and activated carbon (AC) is added to the composition, the Rs value increases despite the total mass of

the sample remaining constant. This variation can be linked to the intrinsic differences in the electrical conductivity of TiC and AC. TiC, being a highly conductive material, contributes to lower resistive losses, whereas AC, while beneficial for its high surface area and electrochemical activity, has comparatively lower electrical conductivity. Consequently, the introduction of AC reduces the overall conductivity of the electrode material, leading to an increase in Rs. This behavior highlights the trade-off between achieving high conductivity (low Rs) and incorporating materials like AC for enhanced surface area and capacitive performance. Optimizing the ratio of TiC to AC is, therefore, essential for balancing conductivity, capacitance, and overall device performance.

Table 5.2 Numerical Magnitudes of Series Resistance of supercapacitors at 1V

Electrolyte	**Rs (ohms)**				
	S1	**S2**	**S3**	**S4**	**S5**
E1	93.9	105.8	90.51	198.8	114.6
E2	77.98	101.8	106.1	180.1	202.2
E3	72.07	76.71	78.67	79.8	89.17

Bode plots are crucial in EIS (Electrochemical Impedance Spectroscopy) analysis because they show how the impedance magnitude and phase angle of a system change with frequency. This helps in identifying whether a supercapacitor behaves more like a capacitor, resistor, or inductor at different frequencies. For example, a phase angle near –90° indicates ideal capacitive behavior, while deviations point to resistive losses or inductive effects. By analyzing these trends, researchers can evaluate the charge storage efficiency, ion transport limitations, and overall performance of the supercapacitor.

Figure 5.8 (a) shows the impedance-based Bode plots of said supercapacitors. The impedance-based Bode plot is between frequency and impedance(Z). This plot describes the change in the trend of overall impedance with frequency. From Bode plot analysis, real and imaginary impedance responses of supercapacitors can be calculated. Real and imaginary impedances can be utilized to determine the real and imaginary capacitance characteristics of supercapacitors.

Figure 5.8(a) illustrates that the impedance decreases with increasing frequency and vice versa. Figure 5.8(b) shows the phase difference-based Bode plots for a charging voltage of 1V. In a Bode plot based on phase difference, frequency is represented on the x-axis, while the phase angle is shown on the y-axis. The phase difference between voltage and current is the phase angle magnitude. If the supercapacitor is considered ideal, then this phase difference is 90°, which means that the current leads the voltage by a 90° phase shift. Based on fundamental circuit theory, at higher frequencies, the capacitor's impedance is almost zero, while at lower frequencies, the impedance increases significantly, approaching infinity [216].

At high frequencies, the series resistance (Rs) in an electrochemical system allows charge to flow readily. This is because, at high frequencies, the impedance of capacitive elements becomes negligible, effectively short-circuiting them. In such conditions, the behavior of the system is dominated by resistive components like (Rs), where the phase difference between current and voltage is zero. This zero-phase difference indicates that the current and voltage are perfectly in phase, a characteristic of purely resistive behavior.

As the frequency decreases, the impedance of the capacitor increases, governed by the relationship $\mathbf{Zc = 1/j\omega C}$, where Zc represents the capacitive impedance, ω represents the angular frequency, and C represents the capacitance. The capacitive impedance becomes

significantly large, dominating the overall system response at very low frequencies. This causes the phase angle to approach its maximum value (close to -90°), reflecting the predominantly capacitive nature of the system. In the low-frequency region, the capacitor's behavior enables a more detailed analysis of its physical properties, especially the active surface area of the electrode that interacts with the electrolyte. This is because, at low frequencies, the capacitive elements have sufficient time to charge and discharge fully, allowing for the measurement of the system's maximum capacitance.

The capacitance is directly proportional to the physical area of the electrodes, as described by $\mathbf{C=\epsilon A/d}$, where C represents the capacitance, ϵ is the permittivity, A is the surface area, and d is the separation between electrodes. By analyzing the system's impedance and phase angle at both high and low frequencies, valuable insights into the capacitor's behavior can be gained. At high frequencies, the data helps identify resistive losses and the internal resistance of the system. At low frequencies, the analysis reveals information about the charge storage capability and diffusion processes. Together, these observations allow for a comprehensive evaluation of key electrical and physical properties, including the effective electrode area.

According to Figure 5.8 (b), sample S1, which is purely TiC, shows the highest value of phase difference with electrolytes E2 and E3, which means the maximum physical area is evaluated in the case of electrodes of pure TiC.

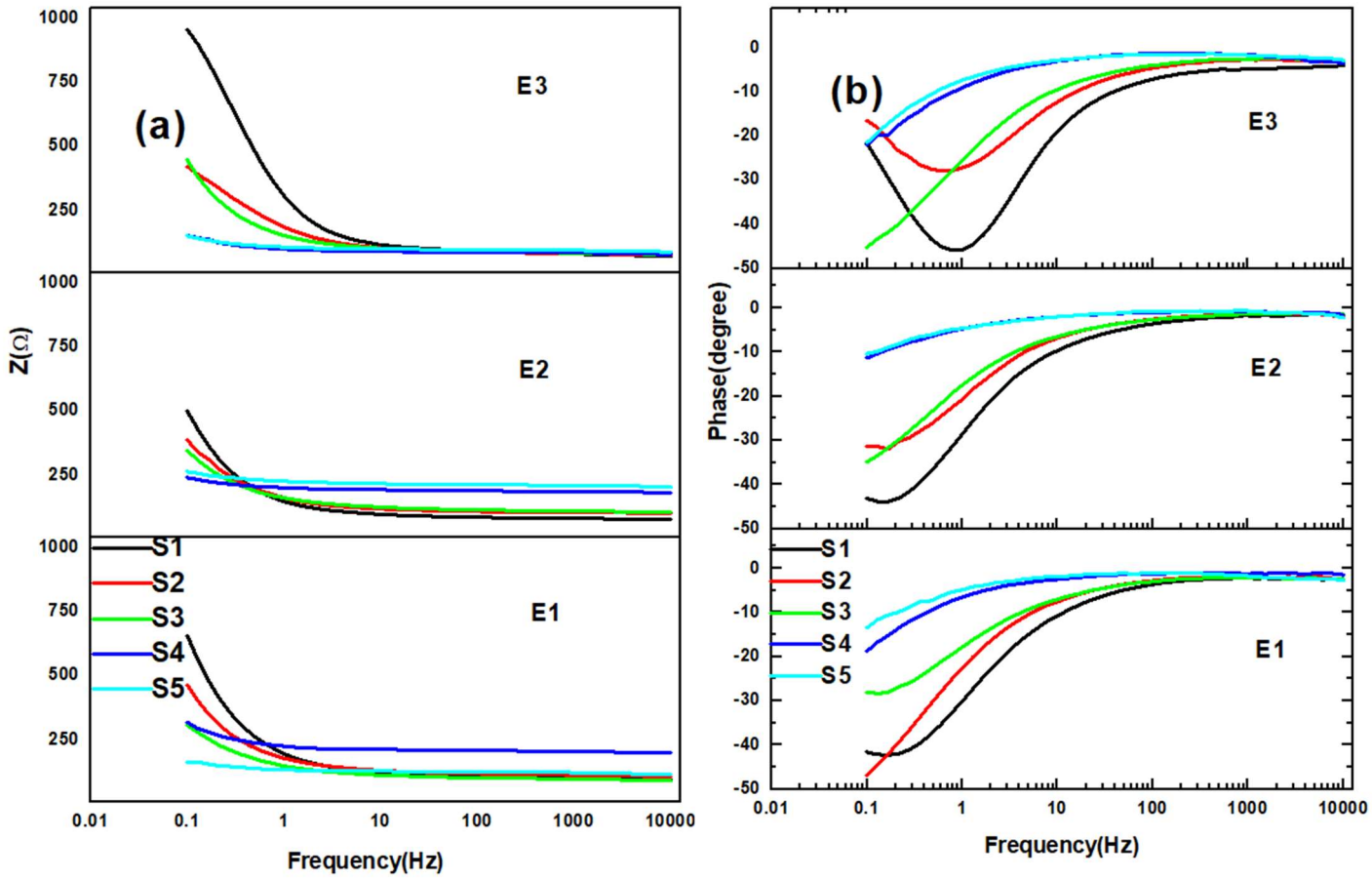

Figure 5.8 EIS-based Bode Plot, (a) Impedance-based Bode plots, (b) Phase-based Bode plots

5.1.2.4 Kinetics of Current

The kinetics of electric current at charging voltages of 1 V are also studied here. Figure 5.9 shows circuit schematics for charging and discharging supercapacitors. In charging and discharging the supercapacitor, a DC power supply, an ammeter, a supercapacitor, and a 328P Microchip are used. Charging of the supercapacitor occurs when switch S1 is closed and switch S2 is open. In discharging mode, the supercapacitor is tested by indirect loading, which means short-circuit analysis and open-circuit analysis.

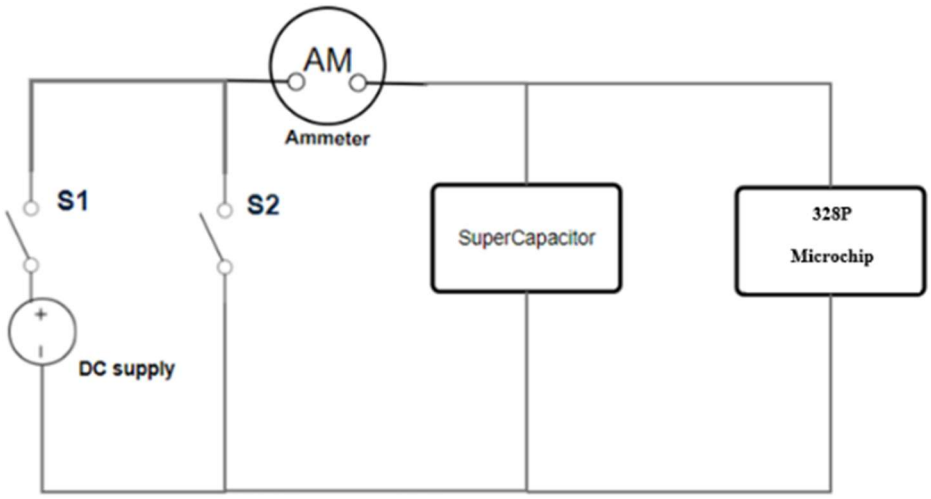

Figure 5.9 Charging and Discharging Schematics

While performing a short circuit test after charging, switch S1 is kept open, and switch S2 is closed. In the open circuit test, after charging, both switch S1 and switch S2 were kept open. During charging, the supercapacitor is charged at 1V for 120 seconds, and during this time, the current is measured by an ammeter.

The Kinetics of the current analysis is to study the detailed charging mechanism at 1V by using Equations 5.3 and 5.4, where **C** shows the capacitance, **I** represents the charging current, and *vt* is the charging voltage [42].

$$\boldsymbol{C = \frac{i}{\frac{dv}{dt}}} \qquad \textbf{(5.3)}$$

$$\boldsymbol{vt = \frac{1}{C}\int_0^{120} idt} \qquad \textbf{(5.4)}$$

The charging behavior of the supercapacitor can be analyzed at 1V. We can plot the transient behavior of charging current(mA), capacitance (F), and Voltage(V) to analyze the time-based charging mechanism. In Figure 5.10, the voltage versus time curve shows variation in the behavior of charging voltage from ground (0-1) V.

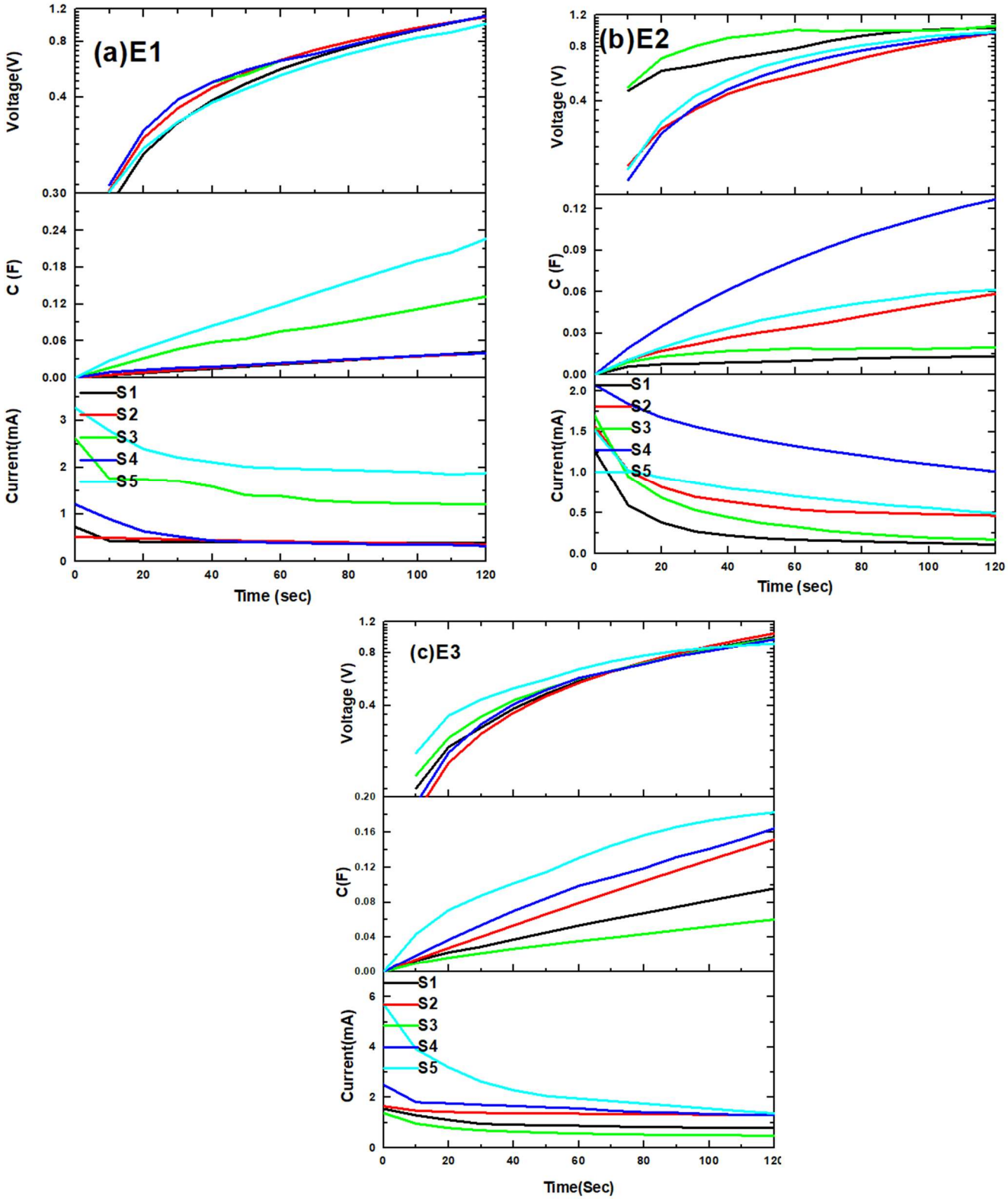

Figure 5.10 Charging characteristics of supercapacitors at 1V for different electrolytes

(a) E1 (b) E2 (c) E3

During the voltage variation period, capacitance increases as a function of the charging current in response to the applied voltage. By analyzing the current kinetics graph, we can effectively examine the charging behavior of a supercapacitor. When studying this behavior, the time required for a specific supercapacitor to fully charge at an applied charging bias of 1V can be calculated. Table 5.3 shows the currents and capacitance values of the supercapacitor during charging.

Table 5.3 Current and Capacitance values while charging

Electrolyte	**Current (mA)**				
	S1	**S2**	**S3**	**S4**	**S5**
E1	0.7	0.5	2.6	1.2	3.2
E2	1.26	1.56	1.69	2.07	1.52
E3	1.55	1.66	1.38	2.51	5.71
Electrolyte	**Capacitance (mF)**				
	S1	**S2**	**S3**	**S4**	**S5**
E1	42.3	39.9	132.1	39.51	226
E2	12.96	58.43	19.89	126.7	61.3
E3	95.72	151.5	60.3	164.2	182.61

In an open-circuit test, the circuit is open, meaning no direct load is attached to the system. In this case, the impedance of the load is at its maximum, resulting in no current flow. Since no current flows through the circuit in this state, the only measurable parameter is the discharging voltage magnitude. The voltage is measured across the capacitor without any current draw, reflecting the voltage behavior over time as the capacitor discharges.

In contrast, during a short-circuit test, the circuit is configured in a way that minimizes resistance. This is typically done by directly shorting the capacitor through an ammeter, where the ammeter itself provides a small amount of resistance. In this scenario, the short circuit condition provides the path with the lowest resistance for current flow, resulting in a maximum current reading. The ammeter records this current, allowing us to measure the capacitor's discharge current under near-zero resistance conditions. The resistance faced in this test is mainly the very small resistance of the ammeter itself, which is insignificant compared to other circuit components. During open-circuit and short-circuit tests, the discharging voltage and current are observed under controlled conditions. The absence of significant power loss is ensured by the lack of a direct external load, and these tests help us understand the discharge characteristics of the capacitor in idealized conditions.

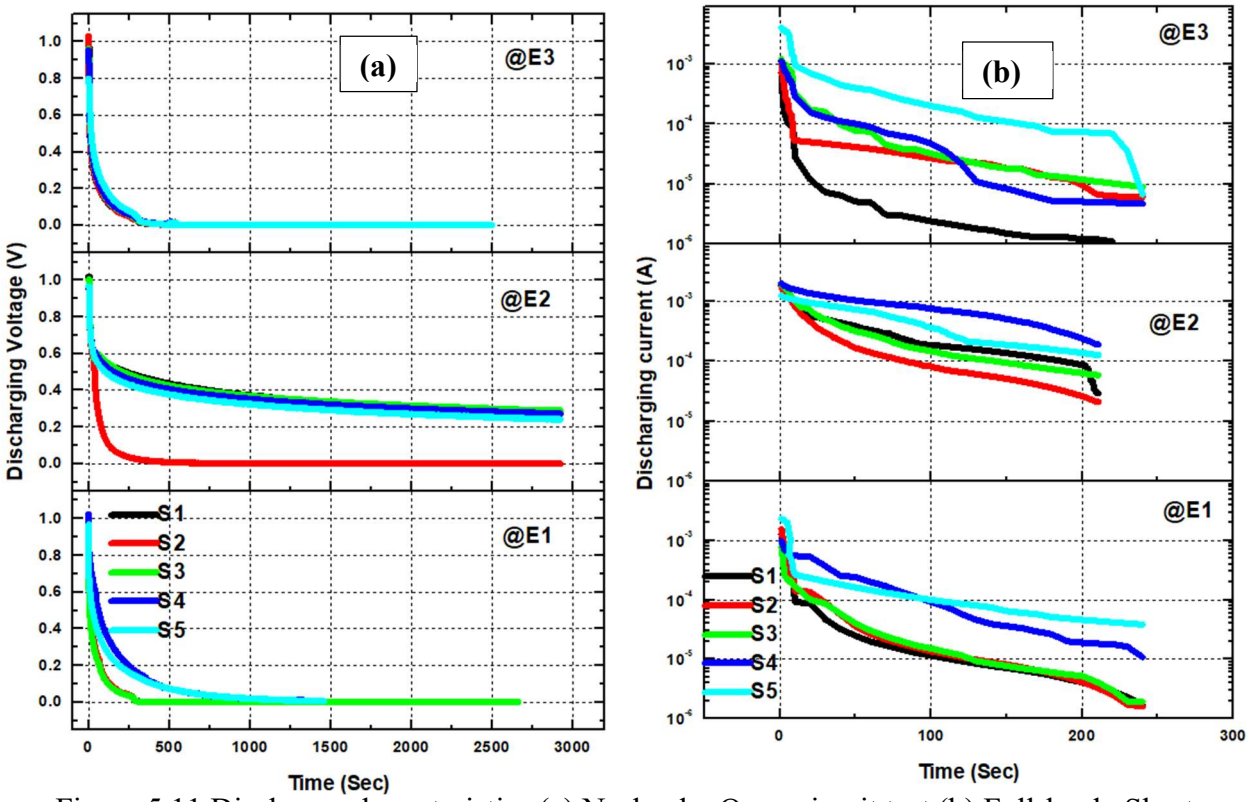

Figure 5.11 Discharge characteristics (a) No-load _ Open circuit test (b) Full-load _Short circuit test.

The time of voltage storage can be calculated by the discharge voltage curve at no Load, as shown in Figure 5.11(a). It is noticed in the discharge curve that when switches S1 and S2 open, the voltage drops immediately. During this time, no voltage is measured at the load terminals, and it is called dead-zone. After the dead zone, the voltage is sustained due to stored charge, and it is called the operation zone of the supercapacitor. [215].

Figure 5.11(b) shows the discharging current characteristics of supercapacitors. Table 5.4 shows how much current can be provided by a supercapacitor for 4 minutes. In the open circuit tests, electrolyte E2 shows the highest initial currents, exceeding 1200μF across all samples. Additionally, after 4 minutes, it maintains high values of the lowest current, greater than 20μF in all cases. This indicates that electrolyte E2 provides better initial charging and discharging responses than the other electrolytes. For the S4 sample, the electrostatic behavior under full load is particularly noticeable with electrolyte E2. Both the initial and final currents reach their maximum values, showcasing the superior performance of E2 in these conditions. Electrolyte E2 is highly compatible with the electrodes that were fabricated, further enhancing the total performance of the supercapacitor. In terms of the dead zone, the range for electrolyte E2 is from 0.9V to 0.7V, except for sample S2, which discharges quickly across all electrolytes. For all samples with electrolyte E2 (except S2), the supercapacitors retain a voltage of approximately 0.3V after around 3000 seconds (50 minutes), which serves as a key indicator of performance during the open-circuit test.

This voltage retention is a significant figure of merit, showing how well the supercapacitor holds its charge. The operating time of the electrodes using electrolyte E2 is approximately 30 minutes, demonstrating its efficient discharge characteristics over this period. Overall,

electrolyte E2 provides the most stable and effective performance, with high currents, good voltage retention, and strong compatibility with the electrodes.

Table 5.4 Maximum to minimum current values while discharging

(I_i= initial current, I_f=Final current)

Electrolytes	Current (µA)									
	S1		**S2**		**S3**		**S4**		**S5**	
	I_i	I_f	I_i	I_f	I_i	I_f	I_i	I_f	I_i	I_f
E1	1272	1.7	1567	1.6	779	1.91	983	10.8	2320	38.2
E2	1890	29	1805	21	1935	58.7	2011	189	1247	128
E3	706	0.1	1100	6.1	1199	9	1126	4.7	4100	6.7

5.2 MXenes / Conducting Polymers-based Asymmetric Supercapacitors

This study develops three asymmetric supercapacitors using Poly (benzoxazole aniline) (pBOA) as the anode. The cathodes in these supercapacitors include pristine MXene, a binary composite (MXene-PANI), and a ternary composite (MXene-PANI-PEDOT: PSS). Notably, pBOA has only been explored in symmetric supercapacitor systems, such as NiO-pBOA-GNP and V_2O_5-pBOA-Graphene.

This study systematically investigates the potential of pBOA in asymmetric configurations, in conjunction with MXene-based materials, to optimize the performance and practical applicability of flexible energy storage devices [218,219]. The fabricated supercapacitors demonstrated enhanced electrochemical performance, marked by a higher charge storage capacity.

5.2.1 Experimental Details

The study utilized high-purity research- and analytical-grade materials. Materials such as titanium aluminum carbide (Ti_3AlC_2), lithium fluoride (LiF), polyvinyl alcohol (PVA), N-methyl-2-pyrrolidone (NMP), carboxymethyl cellulose (CMC), activated carbon (AC), polyaniline (PANI), and poly(3,4-ethylenedioxythiophene): polystyrene sulfonate (PEDOT: PSS) were used as received, with no additional purification or modification.

$Ti_3C_2T_x$ MXene was synthesized through a selective etching process, where aluminum (Al) layers were removed from the Ti_3AlC_2 MAX phase. This was done using a mixture of lithium fluoride (LiF) and hydrochloric acid (HCl), which facilitated the breakdown of the MAX phase structure, resulting in the formation of layered $Ti_3C_2T_x$ MXene. Initially, 1.5 g of LiF was dissolved in 45 mL of 6 M HCl in a container under continuous magnetic stirring. Then, 1.5 g of the MAX phase powder was slowly added to the solution with continuous stirring. The etching reaction was carried out at 45 °C for 24 hours, followed by cooling the mixture to room temperature. The resulting material was washed multiple times with deionized water via centrifugation at 3500 rpm for 6 minutes per cycle until the pH of the supernatant exceeded 5. The final product was collected using Whatman filter paper and dried under vacuum at 60 °C for 12 hours to yield $Ti_3C_2T_x$ MXene powder [220]. Poly(benzoxazole aniline) (pBOA) was synthesized using a one-step procedure that involved chemical polymerization combined with reflux condensation [221]. The binary MXene composite was synthesized by dissolving blue polyaniline (PANI) powder in N-methyl-2-pyrrolidone (NMP) and stirring the solution for approximately 4 hours at 50 °C to form a uniform solution. This solution was then mixed with an aqueous dispersion of $Ti_3C_2T_x$ MXene under continuous stirring, resulting in the preparation of black MXene–

PANI precipitates, which were subsequently isolated by filtration to obtain the final composite [169].

The MXene–PANI composite was combined with PEDOT: PSS by thoroughly grinding the components together using a mortar and pestle. This process was carried out continuously to ensure proper integration. As a result, a ternary MXene–PANI–PEDOT: PSS composite was formed.

Carbon fiber serves as the substrate for depositing the active material due to its flexibility, superior electrical conductivity, and ductile properties. Carbon fiber was pretreated with a sulfuric–nitric acid mixture to activate its surface before electrode material application. Once activated, the carbon fiber was repeatedly rinsed with ethanol and deionized water to remove any remaining acid residues. It was then oven-dried to ensure all moisture was eliminated before further application.

PBOA, MXenes, MXene–PANI, and MXene–PANI–PEDOT: PSS electrodes were fabricated using a defined process to ensure effective mixing and material deposition. Initially, the active material, carboxymethyl cellulose (CMC) binder, and activated carbon (AC) were measured out in a proportion of 8:1:1. These components are then spread in NMP (N-Methyl-2-pyrrolidone) through continuous crushing. This step ensures uniform blending of the components and produces a homogeneous suspension, commonly referred to as “ink.” Ink concentration was controlled by varying the amount of NMP solvent. This allows control over the viscosity and consistency of the ink for deposition. Once the ink is ready, it is applied to activated carbon cloth using the dip-coating method. The cloth acts as a flexible substrate for the electrode material. During this process, it is immersed in the ink, allowing the active material to coat its surface evenly. The dip-coating step ensures uniform deposition, resulting in a well-formed and structured electrode.

For the preparation of MXene-PANI-PEDOT: PSS electrodes, a defined fabrication process is used. MXene-PANI composites are mixed and ground with PEDOT: PSS, a conducting polymer, without the addition of NMP. The prepared mixture is applied to carbon cloth via the dip-coating method, eliminating the need for a separate binder. In this composite, PEDOT: PSS functions simultaneously as a conductive additive and a binder. PEDOT: PSS, a well-known conductive polymer, significantly improves the electrical conductivity of the material, making it suitable for electrode applications. Its incorporation facilitates more efficient charge transport pathways, allowing electrons to move quickly through the material. This enhanced conductivity not only reduces internal resistance but also promotes better energy transfer during device operation, ultimately boosting the overall electrochemical performance of the electrode. In addition to increasing the conductivity, PEDOT: PSS also serves as a structural binder within the electrode. By effectively interlinking the MXene–PANI composites, it reinforces the mechanical stability of the electrode structure. This cohesive interaction eliminates the need for an external binder like carboxymethyl cellulose (CMC), simplifying the fabrication process and improving the overall electrochemical performance by reducing inactive components. This dual functionality of PEDOT: PSS enhances the performance and stability of the electrode material [222]. Overall, these steps ensure the creation of highly efficient electrodes with high conductivity, mechanical stability, and optimal electrochemical properties for use in energy storage or supercapacitor applications.

Before supercapacitor assembly, a gel polymer electrolyte was prepared by dissolving 0.2 g PVA in 6 mL deionized water at 90 °C with stirring. After adding 1 mL glycerol and stirring for 10 minutes, Irgacure, MBA, acrylamide, and AMPS were sequentially mixed in until fully dissolved [189,223]. The hydrogel precursor was placed in a mold and UV-

cured under vacuum. Electrodes were soaked in electrolyte, followed by an additional electrolyte layer, then UV-cured again to form the gel.

5.2.2 General Characterizations and Electrochemical Analysis

The surface features of fabricated electrodes were characterized using scanning electron microscopy (SEM). The crystal structure of the synthesised materials was analysed with X-ray diffraction (XRD). The ASMEC system with a two-probe setup was used to measure the electrical resistance, using voltage–current spectroscopy at ultra-low current resolution. Electrochemical testing was performed using a standard two-electrode setup connected to an electrochemical system analyzer. The supercapacitor's performance was assessed through three methods: cyclic voltammetry (CV), galvanostatic charge–discharge (GCD), and electrochemical impedance spectroscopy (EIS). CV and GCD analyzed specific capacitance, charge–discharge characteristics, and capacitance retention. EIS was performed to measure the system's equivalent series resistance.

Figure 5.12(a) shows the original Carbon Fiber Cloth (CF) morphology, with no additional materials deposited. The fibers appear smooth at their edges, and each fiber's diameter is approximately 8 μm. This shows the natural, pristine structure of the carbon fiber material, highlighting its uniformity and smooth surface.

In Figure 5.12 (b), the changes in the structure of carbon cloth are shown when the MXene-PANI composite is deposited onto a selected portion. This image reveals that the MXene-PANI composite has been successfully applied to the carbon fiber surface. The composite's presence is visually confirmed as it appears to coat and bond with the carbon fibers, enhancing the overall surface structure. When viewed in this state, the rough texture of the fiber shows a marked change due to the deposition. This roughness indicates strong

physical bonding between the MXene-PANI composite and the carbon fibers, which likely enhances their mechanical or electrochemical performance. This bonding enhances adhesion, ensuring the active material remains intact and does not detach during multiple charge–discharge cycles. It shows that the deposition process was successful, allowing the composite to integrate well with the carbon cloth without separation, resulting in durable interface materials [224]. Together, these factors contribute to improved electrochemical performance and long-term durability of the supercapacitor.

Scanning electron microscopy shows that the electrolyte readily flows through the spaces between the carbon fibers. The material deposited on the electrodes also enters the spaces between carbon fibers. (Figure 5.12 (c–d)). Such an open and interconnected structure facilitates efficient ion transport during charge and discharge. This improved electrolyte accessibility improves the overall capacitance and supercapacitor's energy storage performance. Electrolyte ion diffusion helps in the electrode activation by enhancing ion transport and interaction at the electrode surface [225].

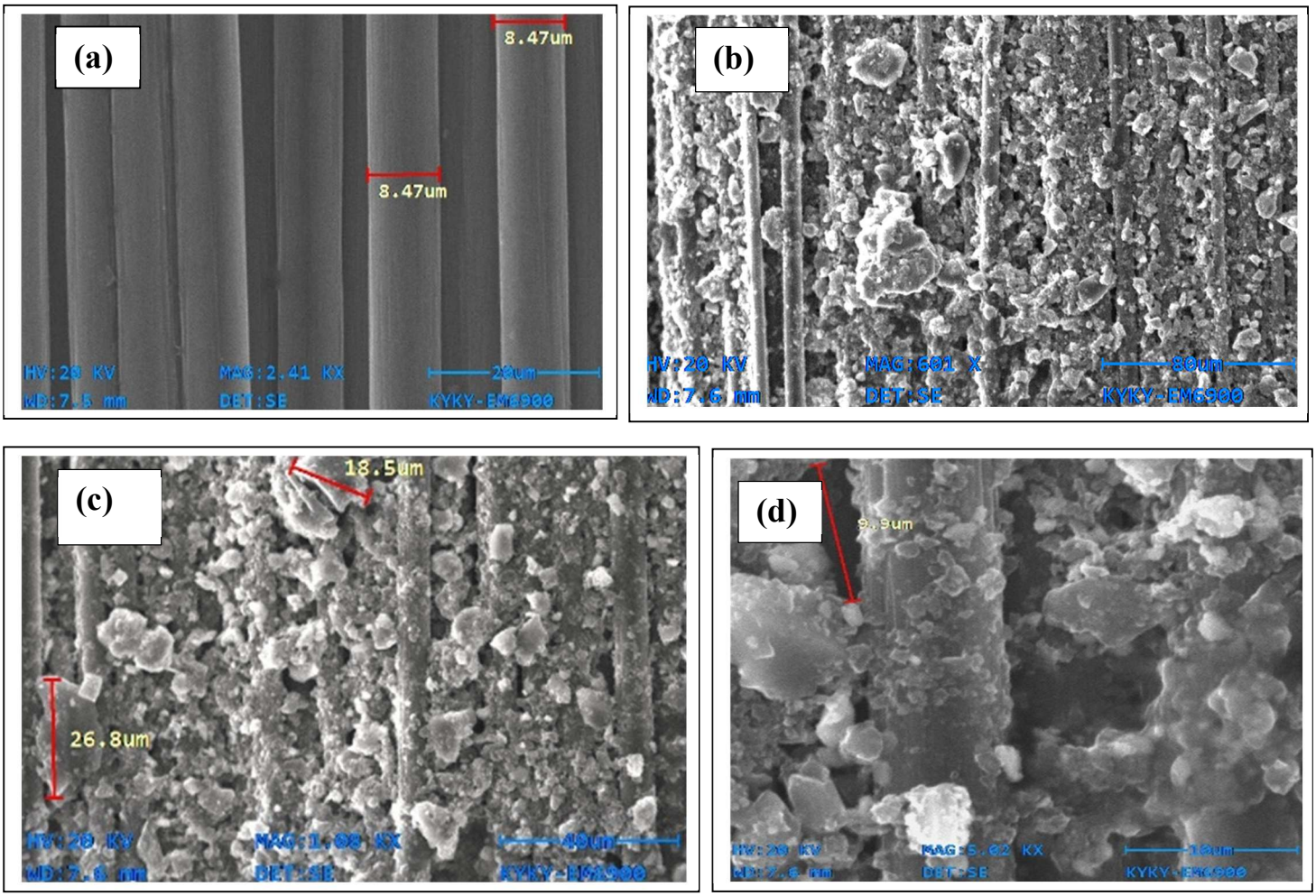

Figure 5.12 SEM images of (a) carbon fiber, (b) carbon fiber coated with MXene–PANI composite, (c, d) detailed views of MXene–PANI deposition on the fiber surface

Figure 5.13(a–b) shows the XRD analysis of MXene and the composites of MXenes with conducting polymer. In pristine MXenes, the (002) peak appears in the XRD pattern, reflecting changes in interlayer spacing influenced by surface functional groups (e.g., –OH, –F, –O). The peak's position and intensity may vary depending on several factors such as synthesis conditions, chemical composition, and post-synthesis treatments [226]. A closer view of the MXene peak is shown, where the main characteristic peak is observed at $2\theta \approx 8.4°$ at the (002) phase (Figure 5.13 (a)) [227,228]. The (002) peak shifted toward

a lower angle (2θ ≈ 7.2°) in the binary (MXene-PANI) composite, confirming the successful intercalation of PANI into the MXene [229,230]. The (002) diffraction peak shifts to approximately 6.6° in the ternary composite of PEDOT: PSS, PANI, and MXene, indicating further interlayer expansion (Figure 5.13(b)). It indicates planar displacement during the development of the ternary structure. Moreover, in the ternary (MXene–PANI–PEDOT: PSS) composite, the PANI peak at 2θ ≈ 25.9°, which is visible in the binary(MXene–PANI) composite, becomes less prominent, suggesting effective encapsulation of PANI by PEDOT: PSS [231,232].

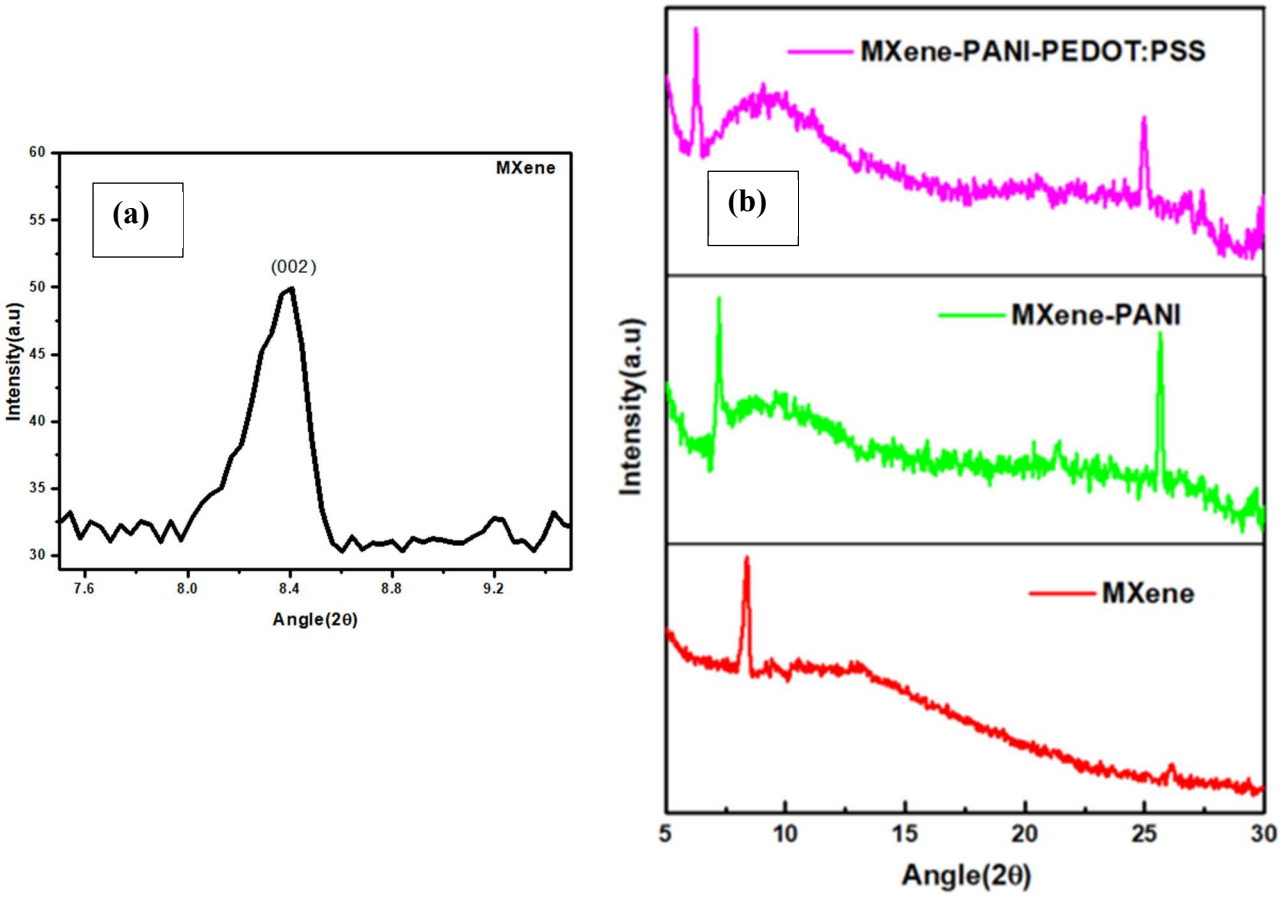

Figure 5.13 XRD (a) Magnified view of XRD of MXene (b) MXenes and their composites

Electrochemical performance of each sample in a two-electrode configuration was evaluated using a two-electrode setup with CV, GCD, and EIS measurements.

CV curves for pBOA//MXene, pBOA//MXene-PANI, and pBOA//MXene-PANI-PEDOT: PSS were recorded at scan rates ranging from 5 to 150 mV/s within a 0.6 V window (Figure 5.14a–c). The CV curves of all supercapacitors exhibited a quasi-rectangular shape, remaining stable even at 150 mV/s, indicating an outstanding rate capability. High-rate capability means the device can efficiently store charge and rapidly diffuse ions during fast charge-discharge cycles, a crucial factor for high-power applications. The CV curve's shape remains stable at higher scan rates, showing the electrode's rapid charge–discharge behavior. This stability suggests minimal resistive losses, allowing ions to move quickly through the electrode material without significant hindrance. The area enclosed by the CV curve represents the charge stored during the cycle. Therefore, a larger enclosed area indicates higher capacitance and better overall performance of the supercapacitor.

Figure 5.14(d) shows CV curves of the reported asymmetric supercapacitors, recorded at a scan rate of 150 mV/s. MXene-based supercapacitor displays only a slight response, indicating low capacitance and limited charge storage capability. This outcome likely stems from the intrinsic properties of pristine MXene, which, despite its high electrical conductivity and broad surface area, may not provide the synergistic benefits found in composite materials that boost energy storage performance.

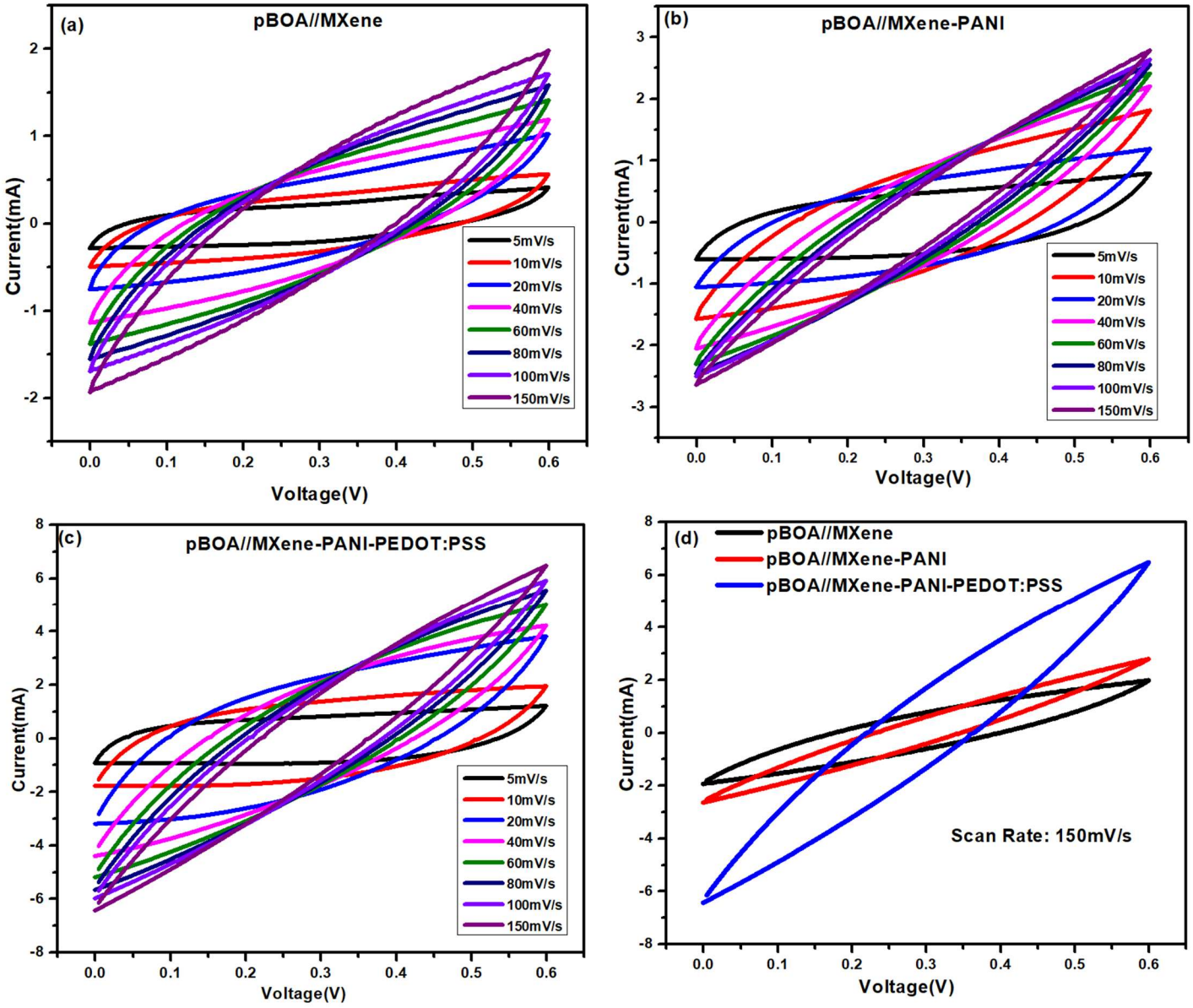

Figure 5.14 CV curves of (a) MXene, (b) binary(MXene-PANI) composite, (c) ternary(MXene–PANI–PEDOT: PSS) composite-based asymmetric supercapacitors, (d) all devices at 150 mV/s

Asymmetric supercapacitor based on ternary composite exhibits a much greater CV loop area than MXene and binary composite-based supercapacitors, indicating higher specific capacitance and better charge storage performance. The stronger current response recorded at a scan rate of 150 mV/s scan rate confirms the improved electrochemical performance of this hybrid system. This enhancement is due to the combined properties of the materials

used, such as MXene's high conductivity and surface area, polyaniline's (PANI) pseudocapacitance through its redox-active nature, and PEDOT: PSS's enhanced electronic conductivity and structural stability. Of all the configurations, MXene–PANI–PEDOT: PSS-based supercapacitors exhibit the highest charge and energy storage capacity, outperforming both MXene and MXene-PANI systems.

GCD (galvanostatic charge–discharge) measurements were carried out within a consistent potential window at varying current densities ranging from 0.1 to 0.5 A/g, as shown in Figure 5.15(a–c). The specific capacitance of each device was calculated using data obtained from both cyclic voltammetry (CV) and GCD analyses, providing a comprehensive evaluation of their charge storage capabilities [233,234].

At a scan rate of 5 mV/s, the MXene–PANI–PEDOT: PSS supercapacitor achieves a high specific capacitance of 279 F/g. This performance is substantially higher than that of the MXene–PANI composite, which delivers 153 F/g, and the pristine MXene-based supercapacitor, which only achieves 68 F/g. This significant improvement can be attributed to the synergistic interaction between PEDOT: PSS and PANI, which work together to enhance both charge storage capacity and overall electrochemical performance. When combined with MXenes, these polymers form a conductive and porous network that promotes efficient ion diffusion, increases active surface area, and ensures better utilization of electroactive sites. As a result, the composite electrode exhibits improved capacitance, faster charge–discharge kinetics, and enhanced long-term stability compared to its components.

GCD measurements at 0.1 A/g revealed specific capacitances of 208, 136, and 56 F/g for MXene-PANI-PEDOT: PSS, MXene-PANI, and MXene-based supercapacitors, respectively. Corresponding energy densities were calculated as 13, 7.3, and 3 Wh/kg.

These results demonstrate the enhanced energy storage performance of the composite systems, particularly the MXene–PANI–PEDOT: PSS configuration, because of its improved charge storage mechanisms.

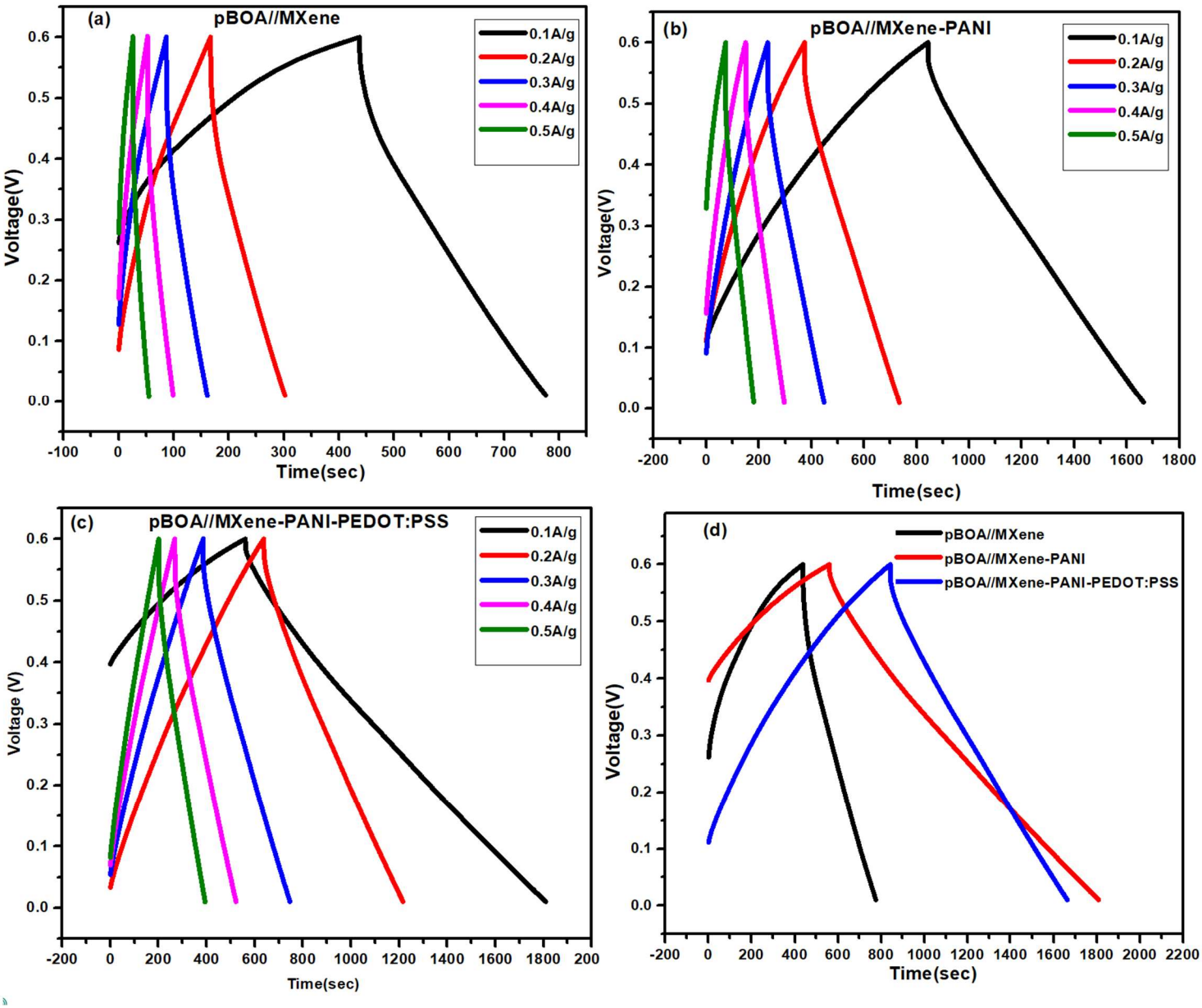

Figure 5.15 GCD curves for (a) MXene, (b) binary(MXene-PANI) composite, (c) ternary(MXene–PANI–PEDOT: PSS) composite-based asymmetric supercapacitors, (d) all devices at 0.1 A/g.

Figures 5.16(a) and (b) show how specific capacitance (C_{SP}) varies with scan rate and current density for all three fabricated asymmetric devices. The specific capacitance is higher at lower scan rates and current densities but drops as these values increase. At lower scan rates, electrolyte ions have enough time to penetrate the porous electrode structure and reach active sites, enabling efficient charge accumulation and resulting in higher capacitance [233,234].

Furthermore, the cyclic stability of the supercapacitors was assessed through GCD measurements conducted at a current density of 1 A/g. As illustrated in Figure 5.16(c), after 1,000 charge–discharge cycles, the capacitance retention was 96% for MXene-PANI-PEDOT: PSS, 91% for MXene-PANI, and 89% for the pure MXene-based devices.

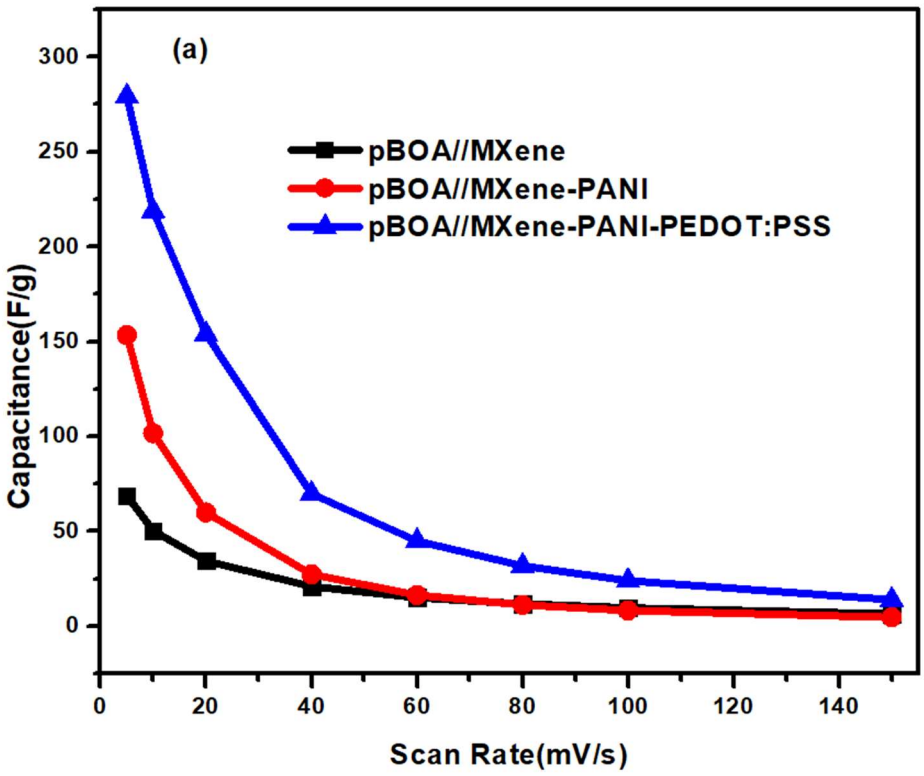

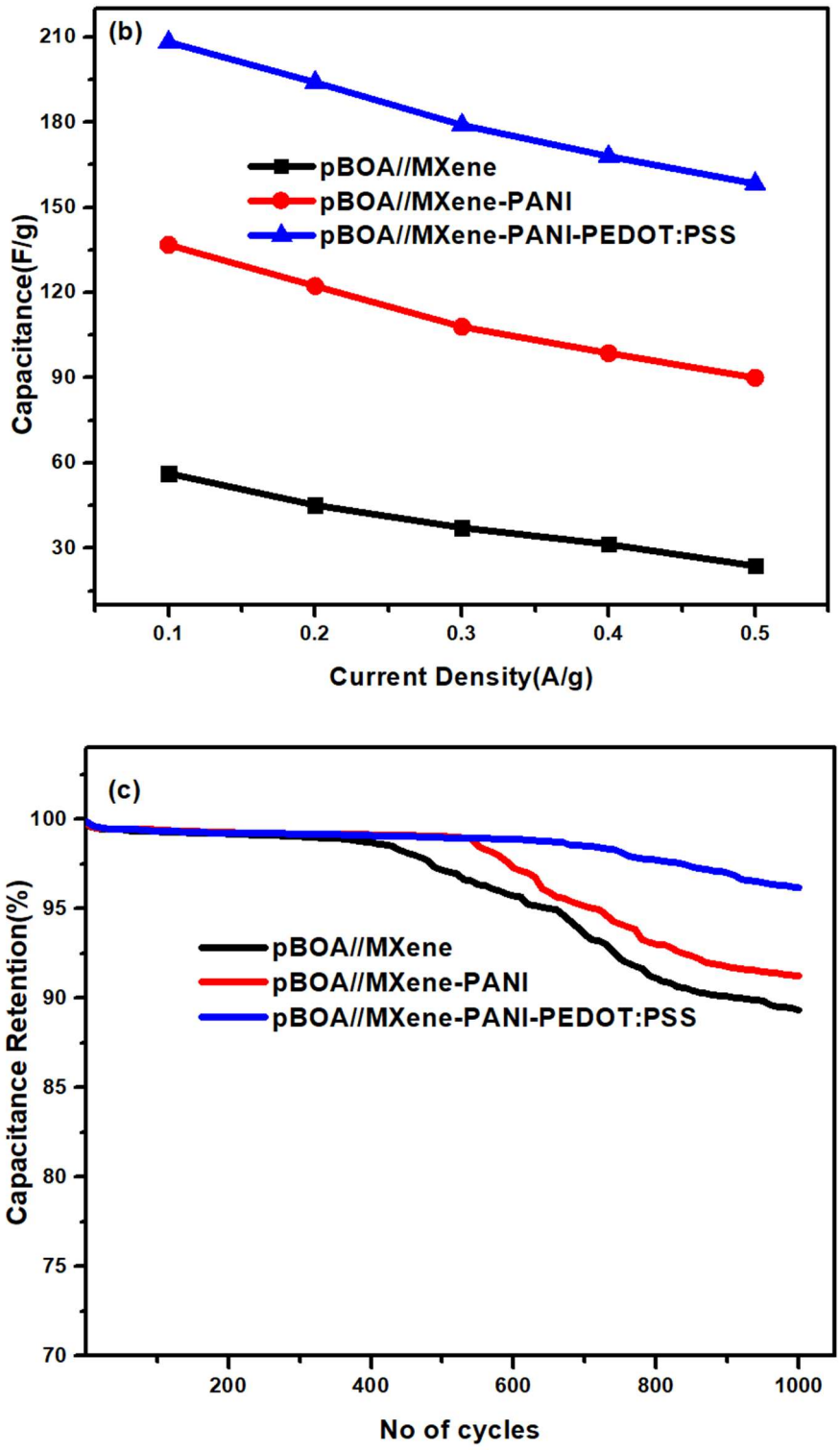

Figure 5.16 (a) Capacitance as a function of scan rate, (b) Capacitance as a function of current density, and (c) Capacitance retention

EIS analysis was done to further investigate the behavior of each component of the supercapacitor as well as the overall cell performance. The analysis was performed over a frequency range of 0.1 Hz to 10 kHz, with a bias voltage ranging from 0.2 V to 1 V. However, in this study, only the readings at 0.2 V are discussed, owing to the complexity and large size of the dataset. Figure 5.17(a) shows the Nyquist plots for all the supercapacitors. After performing circuit fitting based on the Randles circuit, equivalent series resistance (Rs) and charge transfer resistance (Rct) values were obtained from the high-frequency region. The electrochemical impedance spectroscopy results showed that the ternary composite (MXene-PANI-PEDOT: PSS)-based supercapacitor exhibited the lowest series resistance (Rs) and charge transfer resistance (Rct), with values of 27.19 Ω and 28.03 Ω, respectively. In comparison, the MXene–PANI device showed slightly higher Rs and Rct values of 37.43 Ω and 38.72 Ω, while the pure MXene-based supercapacitor demonstrated the highest resistances at 75.71 Ω (Rs) and 77.57 Ω (Rct). These findings indicate improved electrical conductivity and more efficient charge transfer at the electrode–electrolyte interface for the ternary composite-based device. In the low-frequency region of the EIS (electrochemical impedance spectroscopy) curve, the slope reflects the ion diffusion characteristics within the electrode material, exhibiting behavior indicative of Warburg resistance. This suggests effective ion transport and favorable electrochemical kinetics within the composite electrode structure [150]. At low frequencies, the Warburg diffusion line appears almost parallel to the imaginary axis, indicating efficient ion diffusion from the electrolyte to the electrode interface. This boosts the specific capacitance of the MXene–PANI–PEDOT: PSS supercapacitor. The ternary device has the lowest equivalent series resistance (Rs) reported, due to its minimal sheet resistance, as shown in the IV characteristics of Figure 5.17(b). IV analysis reveals that the

ternary composite has a significantly lower sheet resistance of 0.3 kΩ/sq, compared to 1.06 kΩ/sq for the binary composite and 1.3 kΩ/sq for pure MXene, respectively.

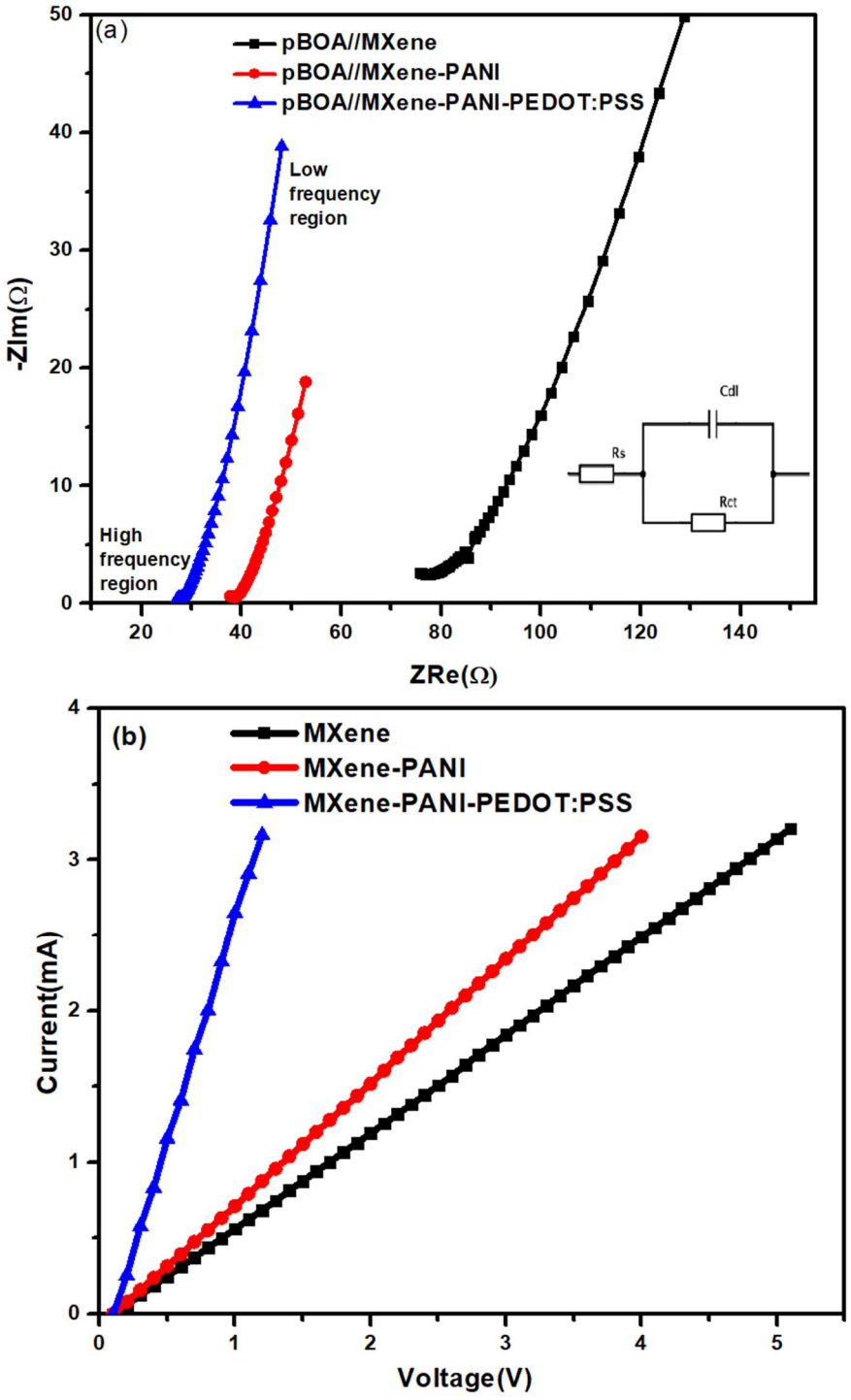

Figure 5.17 (a) Nyquist plots of reported asymmetric supercapacitors and (b) I–V curves of MXene-PANI-PEDOT: PSS, MXene-PANI, and MXene materials.

The voltage is systematically varied in IV analysis, and the corresponding current response is measured, as depicted in Figure 5.17(b). The differences in charge storage behavior among the supercapacitors are due to variations in the conductive behavior of fabricated binary and ternary composites. These variations influence how each material responds to the applied voltage. The MXene–PANI–PEDOT: PSS composite achieves its peak current response at an applied voltage of 1 V. The peak current for MXene–PANI occurs at 4 V, while MXene reaches a maximum current at 5 V. This suggests a direct correlation between electrical conductivity and capacitive performance, with the trend: MXene-PANI-PEDOT: PSS > MXene-PANI > MXene.

To illustrate practical applications, MXene-PANI-PEDOT: PSS devices were connected in series glow the Light Emitting Diodes (LEDs). In this series configuration, the CV curve at 10 mV/s reveals an extended potential window of up to 3 V (Figure 5.18(a)). Figure 5.18(b) shows that four series-connected asymmetric supercapacitors powered four 1.8 V red LEDs for 300 seconds, confirming operation above 1.5 V.

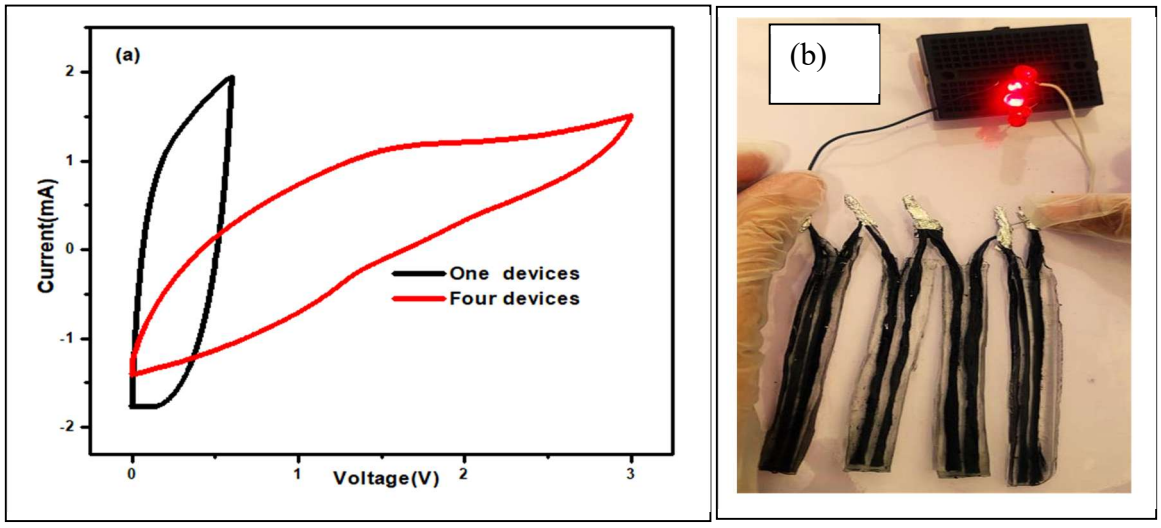

Figure 5.18 a) CV curve of the series-connected supercapacitors; (b) LEDs powered by the series connection device

Table 5.5 highlights the superior electrochemical performance of the MXene-PANI-PEDOT: PSS-based supercapacitor as compared to the other devices.

Table 5.5 Comparative Electrochemical Performance of pBOA//MXene, pBOA//MXene–PANI, and pBOA//MXene–PANI–PEDOT: PSS Supercapacitors

S No.	Device name	Specific capacitance F/g	Energy density Wh/kg	Discharge time(s)	Rs(Ω)	Rct(Ω)
1	pBOA//MXene	68	3	338	75.71	77.57
2	pBOA//MXene -PANI	153	7.3	821	37.43	38.72
3	pBOA//MXene -PANI- PEDOT: PSS	279	13	1249	27.19	28.03

Of the three configurations, the pBOA//MXene–PANI–PEDOT: PSS shows the highest specific capacitance (279 F/g) and energy density (13 Wh/kg), as well as the longest discharge time (1249 s), highlighting its exceptional charge storage capacity. This device also exhibits the lowest series resistance (R_s: 27.19 Ω) and charge transfer resistance (R_{ct}: 28.03 Ω), which contributes to enhanced charge transfer kinetics. The pBOA//MXene–PANI device delivers moderate performance with 153 F/g capacitance, 7.3 Wh/kg energy density, and reduced resistances (R_s: 37.43 Ω, R_{ct}: 38.72 Ω). The pBOA//MXene device, while having the highest resistance (R_s: 75.71 Ω, R_{ct}: 77.57 Ω), shows the lowest capacitance (68 F/g) and energy density (3 Wh/kg), showing limited electrochemical activity. Overall, the sequential incorporation of PANI and PEDOT: PSS significantly enhances the capacitive behavior, energy storage capability, and conductivity of the supercapacitor systems.

5.3 MXene Quaternary (MXene-pBOA-NiO-rGO) Composite-based Symmetric Supercapacitors

This study utilized pBOA, an aniline-derived polybenzoxazole, in binary (pBOA–NiO), ternary (pBOA–NiO–rGO), and quaternary (MXene–pBOA–NiO–rGO) configurations. Composite polymer and its composites are synthesized and deposited over conductive fiber yarn and placed in an acrylamide-based gel electrolyte to fabricate supercapacitors.

5.3.1 Experimental Details

All chemicals were of analytical grade and used as received, without further purification. NiO nanoparticles were synthesized by dissolving 2.2 g of $NiCl_2$ in 100 mL of distilled water, while 0.06 g of CTAB was separately dissolved in 20 mL of distilled water. Both solutions were stirred at room temperature, then combined and mixed for two hours. Sodium hydroxide was gradually added to the mixture until it turned green, indicating the reaction's completion. The mixture was then left at room temperature for 7 hours to allow for further precipitation. The resulting precipitate was thoroughly washed with distilled water, dried at 80 °C for 9 hours, and then calcined at 550 °C for 6 hours to obtain black NiO nanoparticles.

The NiO–pBOA binary nanocomposite was synthesized using an in situ chemical polymerization approach. Initially, the prepared NiO nanoparticles were dispersed in deionized water through 40 minutes of ultrasonication, then continuously stirred to achieve a homogeneous suspension. This suspension was then added to an HCl solution containing the monomer 2-(benzoxazole-2-yl) aniline, initiating the polymerization reaction. After the reaction, the mixture was filtered, and the resulting material was dried at 60 °C.

The pBOA-NiO-rGO ternary nanocomposite was produced through chemical polymerization. Reduced graphene oxide (rGO) is a chemically modified form of graphene, was prepared from graphite. To obtain a uniform dispersion, the pBOA and rGO powder were ultrasonically treated in 100 mL of deionized water for 60 minutes. It was then mixed with dispersion of NiO nanoparticles to form a ternary composite.

For the quaternary composite (MXene-pBOA-NiO-rGO), Ti_3C_2 MXene sheets were effectively prepared through selective etching using HF. Then, an aqueous MXene solution was added to the ternary nanocomposite suspended in NMP and stirred for two hours. The final mixture was filtered to obtain the quaternary nanocomposite.

The fabrication of all supercapacitor devices followed the same procedure. First, MXene, pBOA, NiO, and rGO were mixed in equal mass ratios (1:1:1:1). Then, a cellulose-derived binder, carboxymethyl cellulose (CMC), comprising 10% of the total mass, was added to the active material. To offset the effects of binder, an equal mass of carbon black was added. The mixture was stirred for one hour using NMP as the solvent. This produced a uniform slurry for deposition on carbon cloth.

The conductive carbon fiber cloth was cut into 4 cm lengths and cleaned before depositing the slurry. Each strip was dip-coated with the prepared uniform slurry and placed in an oven at 80°C for three hours. Meanwhile, the electrolyte was prepared, with half poured into the mold and UV-cured for five minutes. After solidification of the electrolyte, the electrodes were placed in the mold at distances of 2, 3, and 4 mm. The remaining electrolyte was then added to fully encapsulate the electrodes in gel electrolyte. After the final UV polymerization, the assembled supercapacitor devices were ready for performance evaluation.

5.3.2 Results and Discussion

Figure 5.19 displays the XRD patterns of the individual materials and the quaternary nanocomposite. The X-ray diffraction (XRD) pattern of NiO nanoparticles reveals distinct peaks at 38°, 42°, 63°, 75°, and 78°, which can be indexed to the (111), (200), (220), (311), and (222) crystal planes, respectively. These sharp and well-defined peaks confirm the crystalline nature of the NiO nanoparticles. In comparison, the XRD profile of poly (benzoxazole aniline) (pBOA) shows broad humps centered around 22° and 23°, corresponding to the (321) and (113) planes. The broadness of these peaks suggests the amorphous or semi-crystalline nature of the pBOA polymer, which is typical for conjugated polymer structures.

In Figure 5.19(c), the presence of MXene is confirmed by the XRD peaks observed at 9.7° and 19.4°, corresponding to the (002) and (004) crystal planes, respectively. These peaks indicate the characteristic layered structure of Ti_3C_2 MXene [235]. In Figure 5.19(d), the XRD pattern shows a prominent peak near 27°, which is characteristic of rGO prepared by the Hummers method. This peak corresponds to the (002) plane of rGO, representing the restoration of graphitic stacking and the effective reduction of oxygen-containing groups during the synthesis process [236].

For the quaternary composite MXene-pBOA-NiO-rGO, the XRD pattern in Figure 5.19(e) shows the characteristic features of each component. The presence of distinct peaks from NiO, MXene, and rGO, along with the broad feature associated with amorphous pBOA, confirms the successful integration of all materials into a single nanocomposite. These combined signatures reveal that the structural and crystalline properties of each component are conserved within the quaternary composite, confirming the effectiveness of the synthesis process [237].

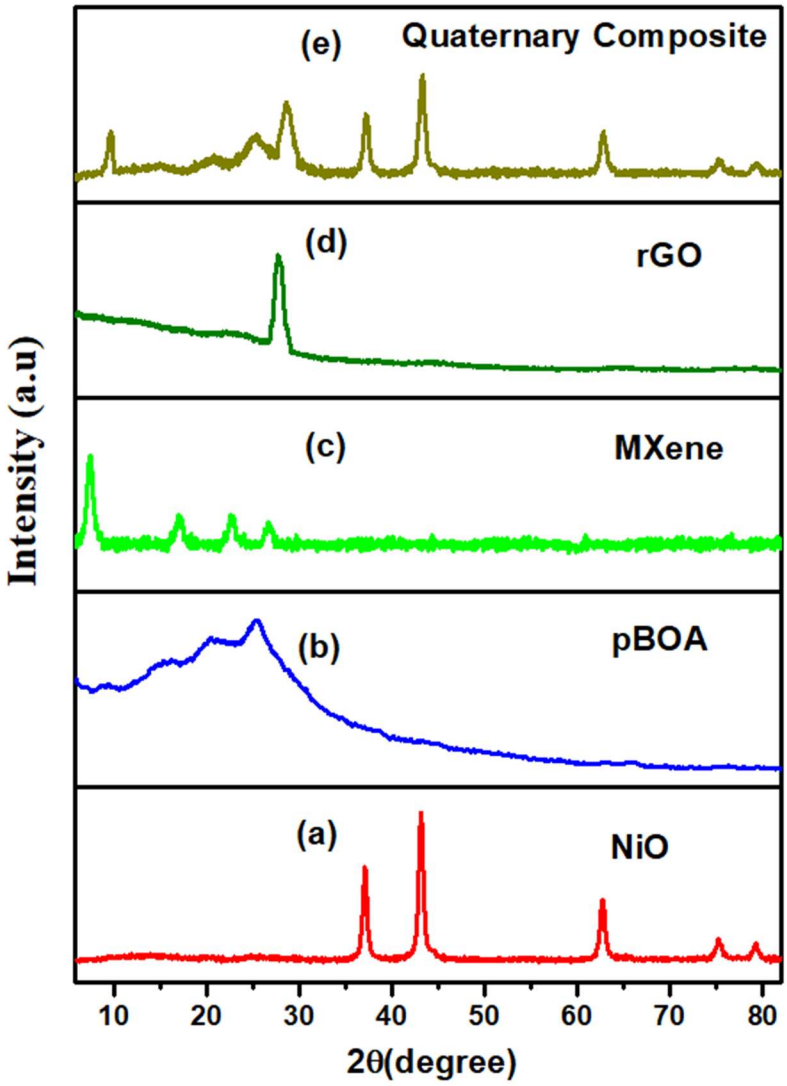

Figure 5.19 XRD patterns of (a) NiO Nanoparticles, (b) pBOA, (c) MXene, (d) rGO, and (e) the quaternary MXene-pBOA-NiO-rGO composite

Cyclic voltammetry (CV) analysis was performed using a two-electrode setup to assess the electrochemical behavior of the fabricated pBOA-based supercapacitors. As shown in Figure 5.20, CV curves were recorded within a 0–0.6 V window at scan rates ranging from 5 to 100 mV/s. The nearly rectangular shape of the CV curves, along with the absence of distinct Faradaic peaks, confirms that the charge storage mechanism is dominated by electric double-layer capacitance (EDLC) rather than redox-based pseudocapacitance.

The pBOA-based supercapacitor exhibits a specific capacitance of 125 F/g at a scan rate of 5 mV/s with an electrode spacing of d_1 = 2 mm. However, increasing the distance between the electrodes to d_2 = 3mm and d_3 = 4 mm results in a noticeable decline in capacitance, dropping to 106 and 84.7 F/g, respectively, as illustrated in Figures 5.20(a–c). This reduction can be attributed to the increased internal resistance and reduced ion transport efficiency across the wider electrode gaps, which adversely affect charge storage performance. Figure 5.20(d) presents the variation of specific capacitance with scan rate, as determined from cyclic voltammetry (CV) measurements. The results reveal that specific capacitance declines as the scan rate increases and further demonstrate its dependence on the spacing between the fibrous electrodes.

Further experiments systematically assess how the composition of binary, ternary, and quaternary nanocomposites affects the electrochemical performance of supercapacitors. To ensure reliable comparisons, all key experimental parameters were kept consistent throughout the experiments. These parameters include the type of electrolyte, the device fabrication process, the spacing between electrodes, and the methods used for mass loading. By keeping these parameters constant, the study focuses on the impact of compositional changes, providing a clearer understanding of how various material combinations affect charge storage and capacitance characteristics.

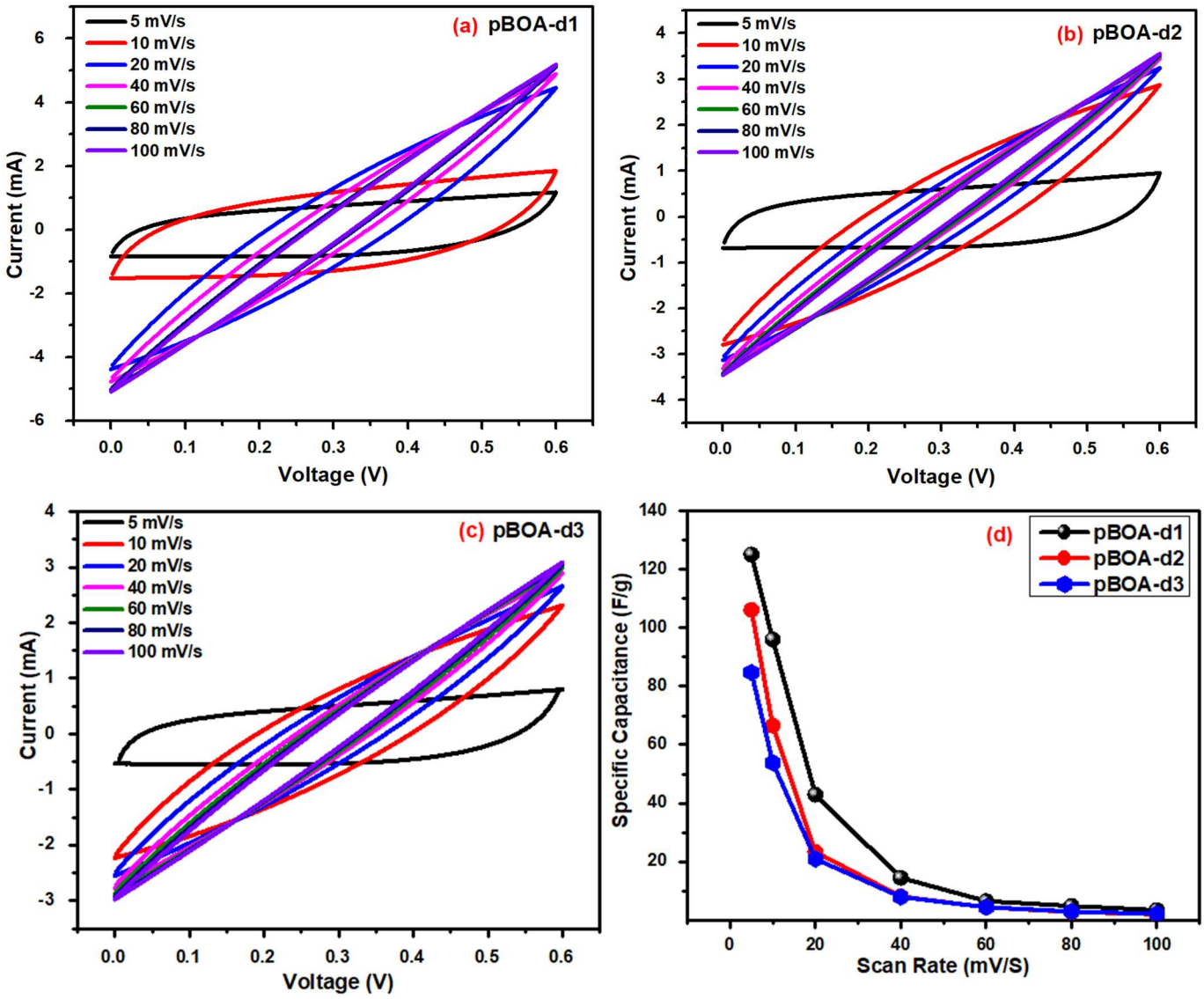

Figure 5.20 Cyclic voltammetry curves of pBOA-based supercapacitors at varying scan rates and electrode gaps: (a) 2 mm, (b) 3 mm, (c) 4 mm, (d) Specific capacitance vs. scan rate

A binary composite was formed by incorporating 50 wt% NiO nanoparticles into the pBOA matrix, yielding a uniform dispersion of the inorganic phase within the polymer network. All other factors, including the electrolyte used, device fabrication technique, spacing between electrodes, and mass loading, were maintained consistently across all

nanocomposites. Incorporating NiO nanoparticles into pBOA enhances capacitive current and CV area, indicating better charge storage. Figures 5.21(a–c) present CV curves for pBOA-NiO devices with electrode spacings of 2, 3, and 4 mm, measured at scan rates from 5 to 100 mV/s in the 0–0.6 V range.

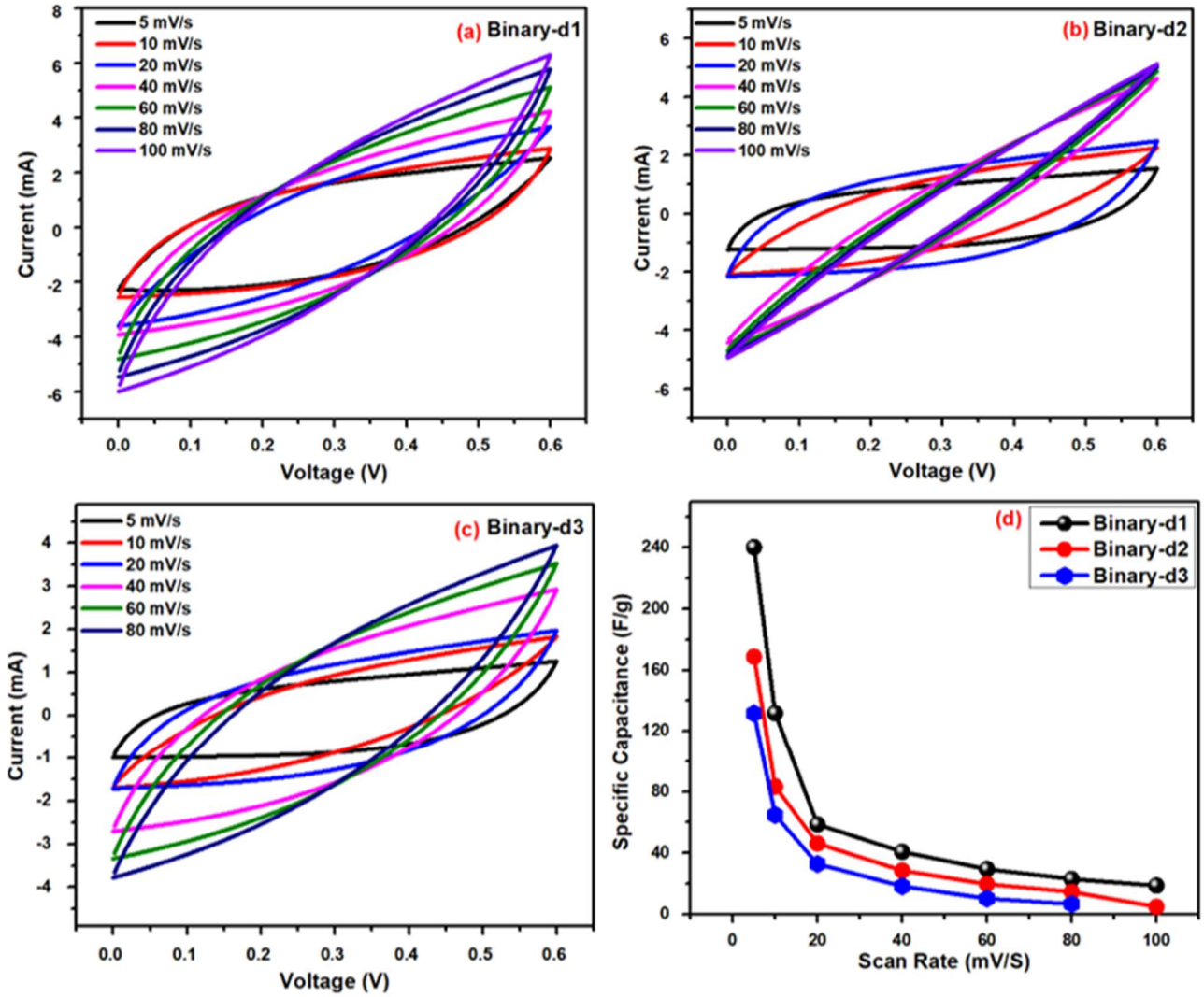

Figure 5.21 Cyclic voltammetry curves pBOA-NiO-based supercapacitors at varying scan rates and electrode gaps: (a) 2 mm, (b) 3 mm, (c) 4 mm, (d) Specific capacitance vs. scan rate

Figure 5.21(d) shows a decline in specific capacitance with increasing scan rate. At 5 mV/s, the supercapacitors based on the binary composite exhibit a significantly higher specific capacitance of 240.3 F/g compared to the 125 F/g shown by the supercapacitor based on pBOA polymer. The improvement is due to the lattice mismatch between pBOA and NiO, aiding ion diffusion and electrolyte access.

Moreover, variations in electrode spacing and scan rates considerably affect energy storage performance, as depicted in Figure 5.21(d). Adding rGO to the pBOA-NiO composite forms a ternary (pBOA-NiO-rGO) nanocomposite, where rGO improves electrochemical performance by increasing electrode conductivity.

Additionally, Graphene's high surface area raises specific capacitance from 240.3 to 266.4 F/g at 5 mV/s in the ternary composite at a scan rate of 5 mV/s (d = 2 mm). Figure 5.22 displays the CV curves and capacitance of the pBOA-NiO-rGO supercapacitor at various scan rates and electrode spacings. All ternary devices fabricated exhibit a steady reduction in specific capacitance as the scan rate and electrode distance increase, following the same pattern observed for both the pBOA and binary nanocomposite devices.

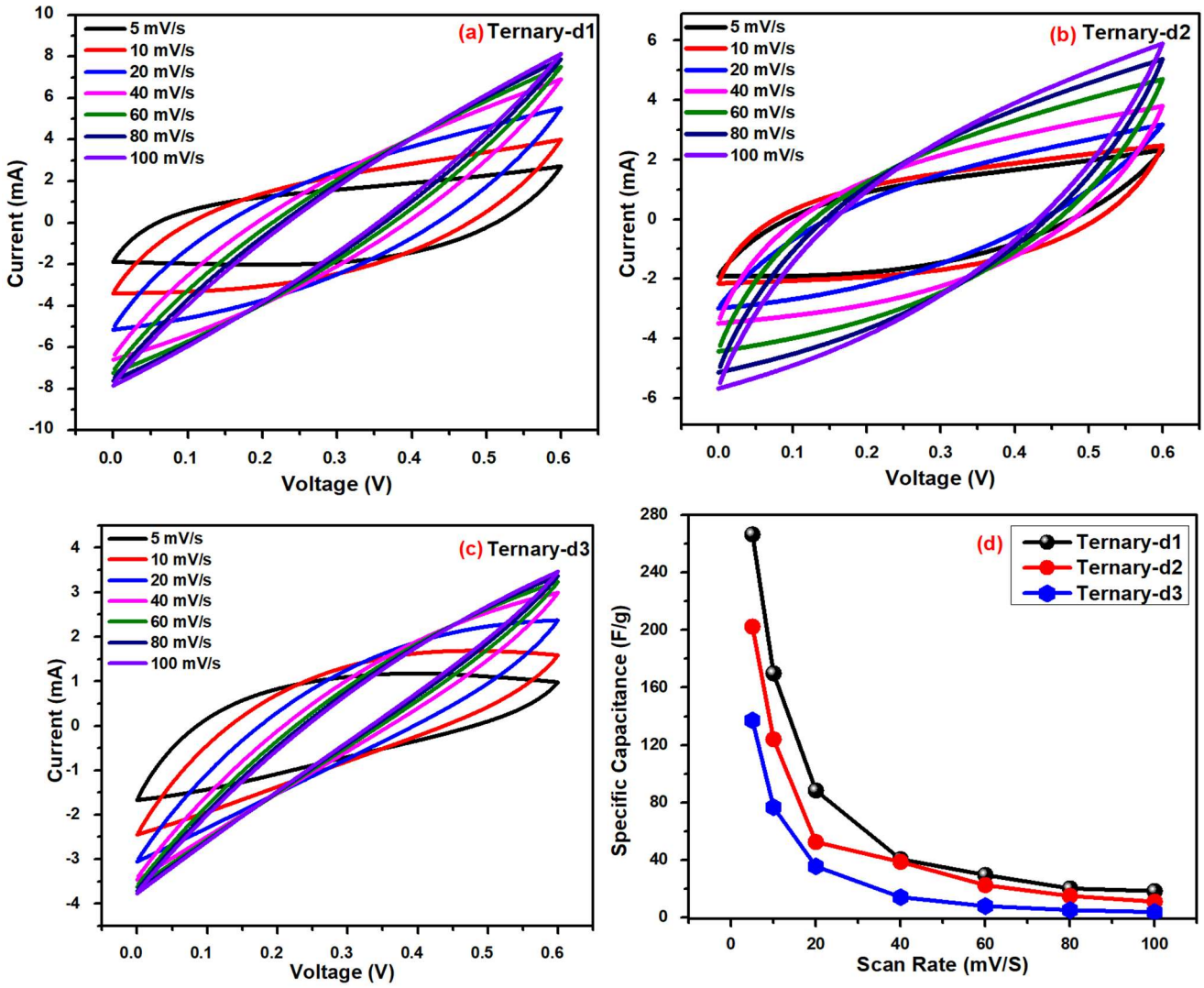

Figure 5.22 Cyclic voltammetry curves of pBOA-NiO-rGO-based supercapacitors at varying scan rates and electrode gaps: (a) 2 mm, (b) 3 mm, (c) 4 mm, (d) Specific capacitance vs. scan rate

The addition of MXene to the pBOA–NiO–rGO ternary composite produces a novel quaternary nanocomposite: MXene–pBOA–NiO–rGO. Its superior supercapacitor performance arises from the synergistic interactions among the components. MXene and rGO establish an interconnected conductive network that facilitates rapid electron

transport, while NiO and pBOA contribute to enhanced redox activity, thereby increasing the overall pseudocapacitive behavior.

The layered and porous structure of the MXene–pBOA–NiO–rGO quaternary composite facilitates efficient ion diffusion and enhances electrolyte infiltration within the electrode matrix. Additionally, pBOA contributes to structural stability, while rGO inhibits MXene restacking, thereby preserving a large surface area.

The electrochemical behavior of this MXene-pBOA-NiO-rGO nanocomposite was analyzed with cyclic voltammetry (CV), as shown in Figure 5.23(a–c).CV performed at various scan rates, with variations in electrode distances, revealed that the addition of MXene markedly enhanced the electrochemical performance of supercapacitors, as shown in Figure 5.23(d). A specific capacitance of 338.4 F/g was achieved at a 5 mV/s scan rate with a 2 mm electrode gap. Increasing the electrode spacing to 3 mm and 4 mm resulted in a decrease in capacitance to 265 and 252 F/g, respectively, highlighting that smaller electrode gaps increase the specific capacitance and charge transfer. Overall, the specific capacitance decreased at higher scan rates and larger electrode separations. Lower scan rates yielded higher capacitance due to more effective electrode-electrolyte interaction. Even at 5 mV/s, capacitance varied with electrode distance, mainly because electric double-layer capacitance (EDLC) weakens as electrode separation increases. These results highlight how device geometry influences electrochemical performance.

By optimizing the geometric configuration, it is possible to improve charge transfer. Such improvements can lead to higher energy storage capacity and faster response times. The design layout directly impacts the overall efficiency and performance of the system.

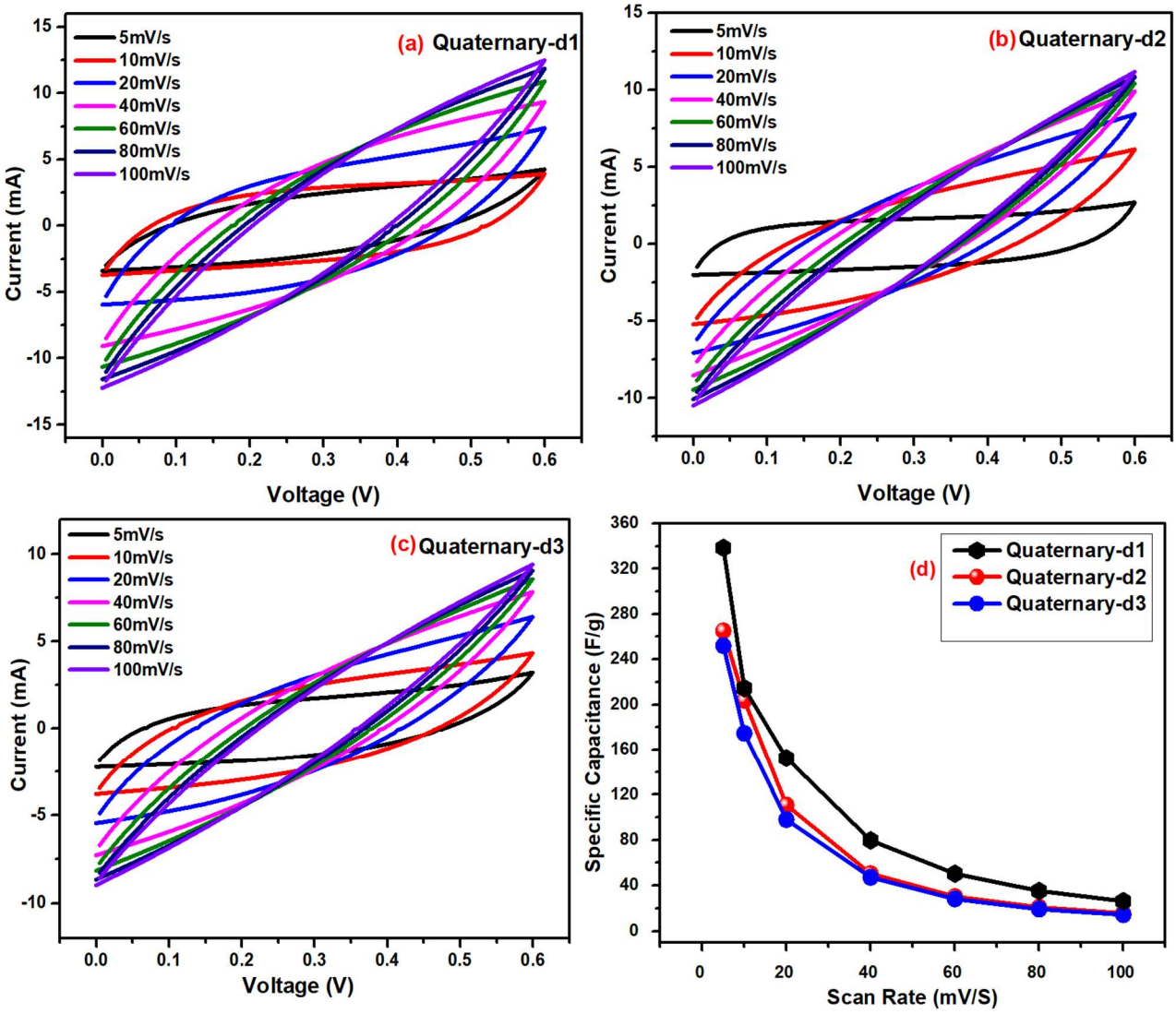

Figure 5.23 Cyclic voltammetry curves of MXene-pBOA-NiO-rGO-based supercapacitors at varying scan rates and electrode gaps: (a) 2 mm, (b) 3 mm, (c) 4 mm, (d) Specific capacitance vs. scan rate

Galvanostatic charge-discharge (GCD) analysis was performed at fixed current densities from 0.1A/g to 0.3A/g within a voltage window (0-0.6V) and a 2mm electrode gap for all fabricated devices. At the initial current density of 0.1 A/g, the supercapacitor exhibited the lowest IR drop, suggesting minimal internal resistance within the device. This reduced

resistance facilitates more efficient charge and discharge cycles by allowing smoother ion transport and electron, eventually enhancing overall electrochemical performance.

The symmetrical shape of the GCD (galvanostatic charge–discharge) curves reflects ideal capacitive behavior, indicating efficient and reversible charge storage. Additionally, the minimal voltage drop and symmetry suggest low contact resistance between the carbon thread current collector and the electrode material. This effective interface supports smooth electron transfer and ion diffusion, contributing to improved energy storage capacity, enhanced charge–discharge efficiency, and long-term cycling stability of the device.

The quaternary nanocomposite-based supercapacitor device with electrode separation of 2mm displayed the longest discharge time of 2000 seconds, and achieved a maximum energy density of 16.9 Wh/kg among all tested supercapacitors. These findings confirm that the addition of MXene notably improves the energy density of the supercapacitor. Its layered structure facilitates efficient ion transport, while the high surface area offers abundant active sites for ion adsorption, enabling greater energy storage without compromising power performance.

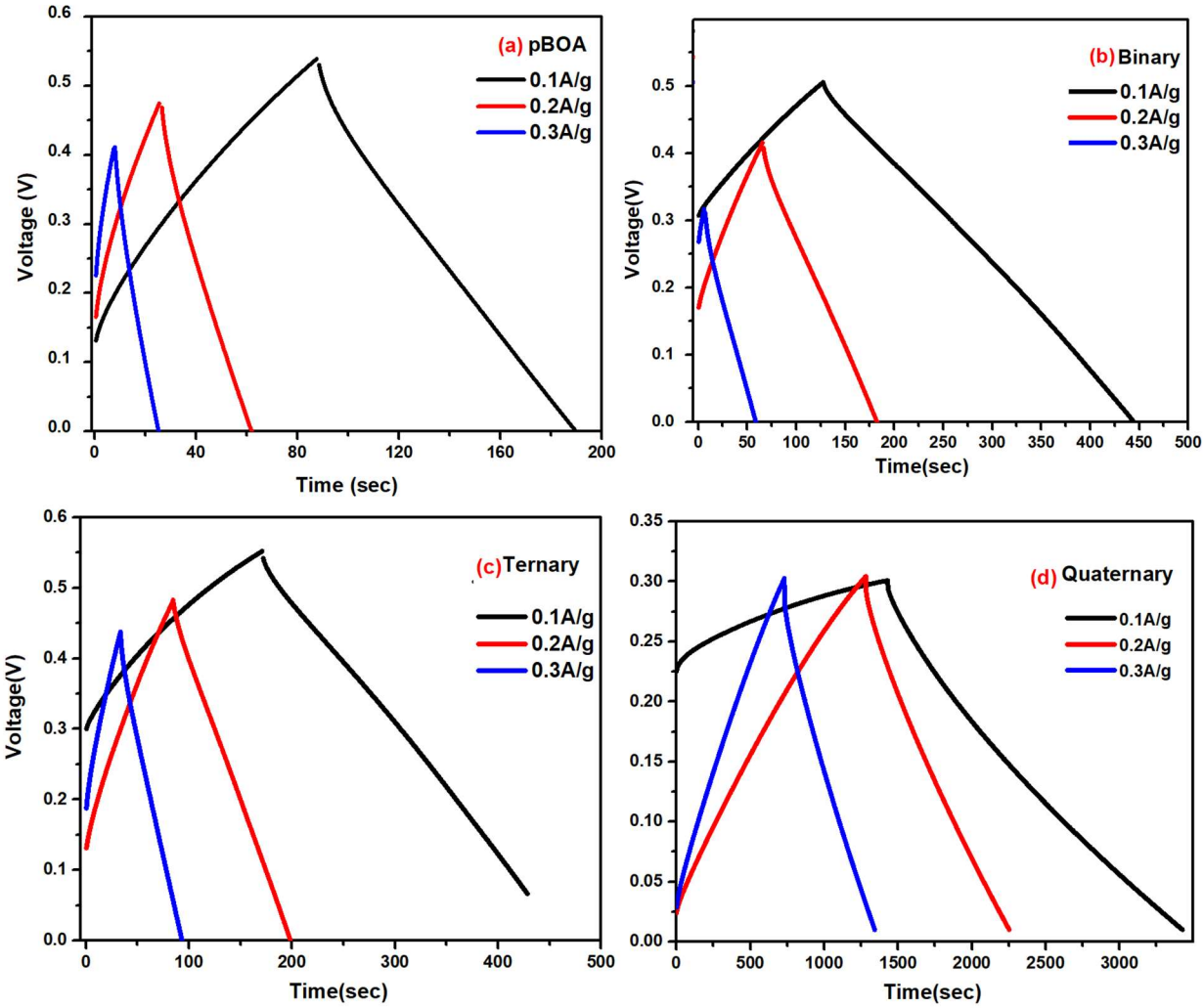

Figure 5.24 GCD curves for reported devices at various current densities (electrode spacing: 2 mm)

EIS was used to evaluate the mobility of ions in the electrolyte and the electrical resistance of the electrode materials. Measurements were conducted using an alternating current of 0.01 mA combined with a direct current biasing of 0.6 V (open-circuit potential), over a frequency range of 0.1 Hz to 10 kHz. Nyquist plots for the pBOA, binary, ternary, and quaternary configurations are presented in Figure 5.25

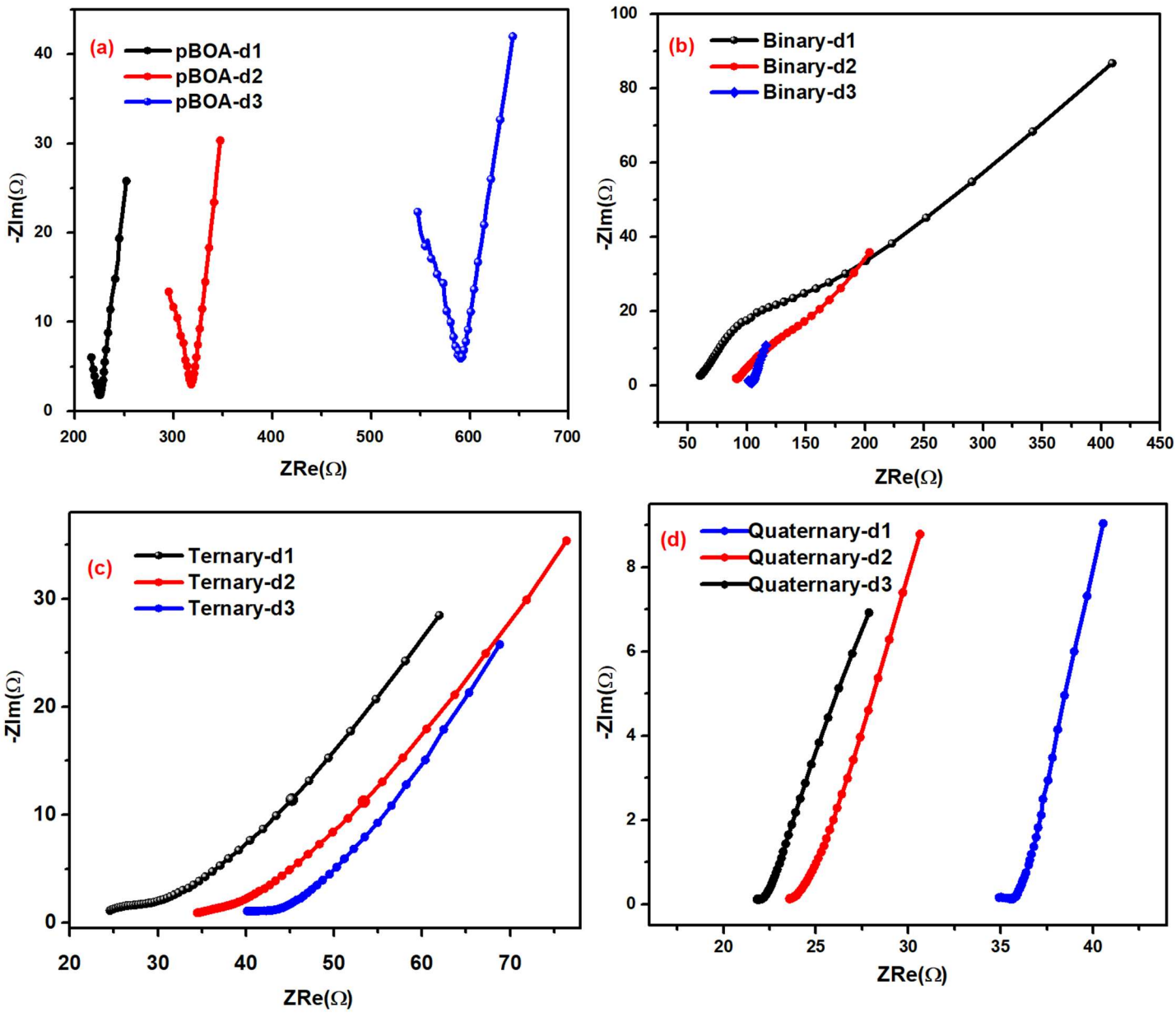

Figure 5.25 Nyquist plots for devices with electrode gaps of 2, 3, and 4 mm: (a) pBOA, (b) binary, (c) ternary, and (d) quaternary composite

A Nyquist plot analysis through an equivalent circuit model offers a valuable understanding of the operational characteristics and performance of the supercapacitor device. The Randles circuit model is used to determine the equivalent series resistance (Rs)

and the charge transfer resistance (Rct). Higher values of series resistance (Rs) reduce power and energy efficiency.

In a standard Nyquist plot of an electrochemical system, the high-frequency region typically shows a semicircle, the mid-frequency region presents a 45° slope, and the low-frequency region appears as a vertical 90° line. In contrast, an ideal supercapacitor should lack a high-frequency semicircle and show a line of 45° immediately, following the equivalent series resistance (Rs).

Figure 5.24(d) shows that the quaternary devices exhibit full supercapacitor behavior, featuring the lowest series resistance (Rs) of 22 Ω, a 45° line, and a 70° sloped line. Series resistance (Rs) decreases from the polymer device to the binary and ternary composites, reaching a minimum in the quaternary device. Furthermore, Rs increases with greater electrode separation (d_1 to d_3) because a larger distance weakens the electric field.

Figure 5.26 presents the impedance-based BODE plots for all the fabricated devices. At lower frequencies, higher impedance values reflect superior supercapacitive behavior, as they indicate the device's ability to store and retain charge effectively. In contrast, the reduction in impedance at higher frequencies is consistent with typical electrochemical responses. Among the various supercapacitor configurations, devices with the shortest inter-electrode distance of 2 mm show the lowest impedance at low frequencies, highlighting their enhanced electrochemical performance and more efficient charge transport compared to devices with larger electrode separations.

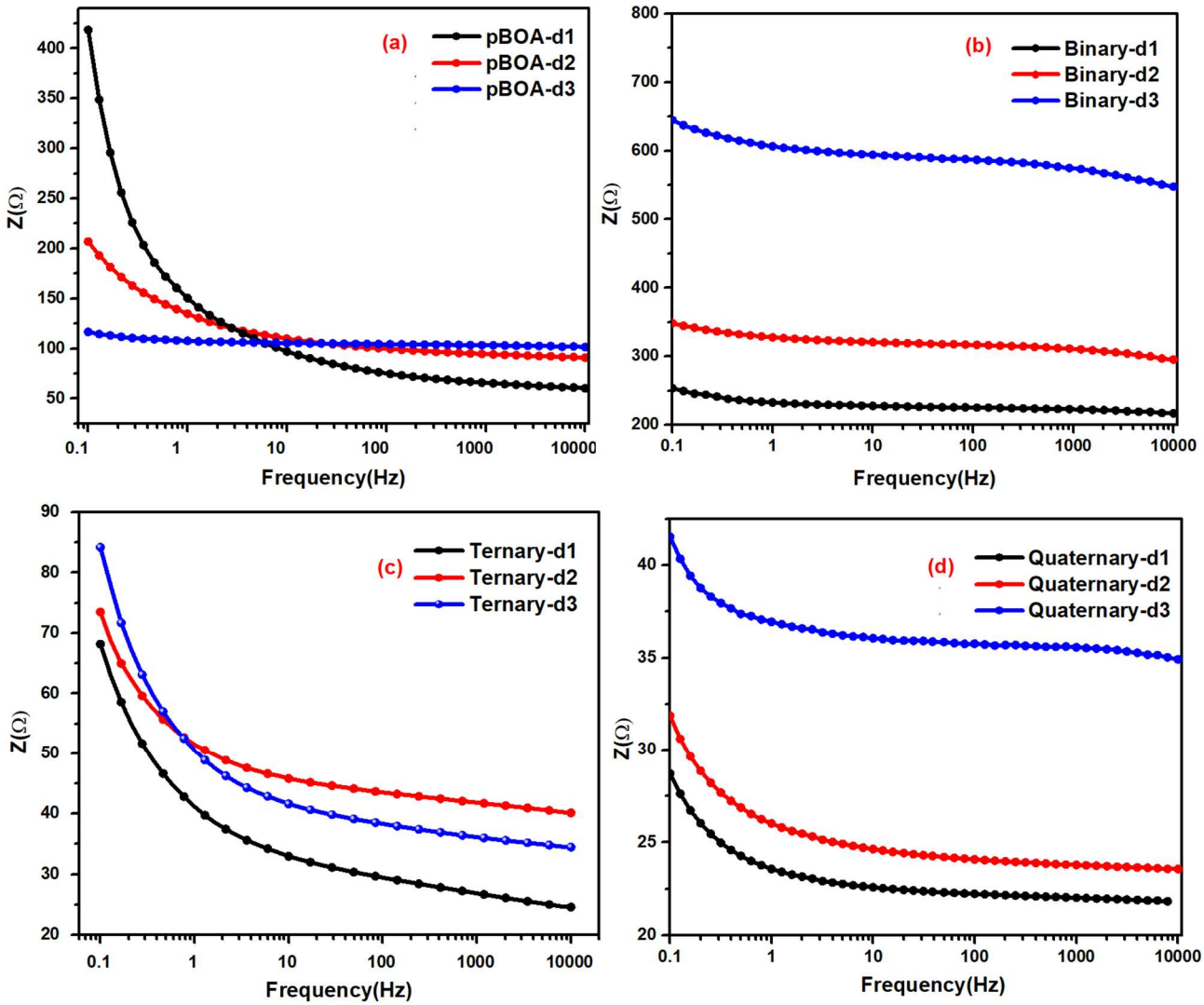

Figure 5.26 BODE plot with electrode separation 2mm, 3mm, and 4mm (a) pBOA device. (b) Binary device (c) Ternary device (d) Quaternary device

The fabricated flexible supercapacitors demonstrated outstanding electrochemical properties, as shown by cyclic voltammetry and galvanostatic charge-discharge measurements, validating the reliability and efficiency of our fabricated supercapacitors. Table 5.6 indicates that, under identical mass loading and electrode spacing, the quaternary composite-based devices outperform the rest of the devices in the electrochemical analysis.

Table 5.6 Evaluation of the electrochemical performance of supercapacitor devices incorporating pBOA, binary, ternary, and quaternary nanocomposites

Device name	Electrode spacing (d)	Specific capacitance F/g	Energy density Wh/kg	Discharge time(s)	Rs (Ω)	Impedance (Ω) @ f→0hz
pBOA	2mm	125.1	6.2	102	208	424
Binary	2mm	240.3	12	256	60	253.4
Ternary	2mm	266.4	13.3	290	25	68
Quaternary	2mm	338.4	16.9	2000	22	42

The engineered flexible supercapacitors of binary, ternary, and quaternary configurations demonstrated remarkable electrochemical performance. The quaternary nanocomposite (MXene-pBOA-NiO-rGO) flexible supercapacitor demonstrated the peak electrochemical performance, with a specific capacitance of 338.4 F/g, energy density of 16.9 Wh/kg, and a discharge time of 2000 seconds. These results highlight its potential for next-generation self-powered, flexible energy storage and electronic systems.

5.4 Comparison with the Reported Literature

A comprehensive comparative analysis has been carried out to evaluate the electrochemical characteristics of various MXene-based devices documented in recent scientific literature and to assess how they compare with our research findings. This analysis focuses on identifying similarities, differences, and potential improvements in electrochemical performance. In alignment with our research methodology, MXene-based supercapacitors are systematically fabricated and subjected to rigorous electrochemical characterization. The fabrication and characterization processes are implemented through the following

three distinct strategies, each designed to optimize different aspects of the supercapacitor's performance.

- MXene-Enabled Impurities (TiC) -Based Supercapacitors
- MXenes and Conducting Polymers composites for flexible asymmetric Supercapacitors
- Quaternary Composite of MXene (MXene-pBOA-NiO-rGO) for Enhanced Energy Storage in Symmetric Supercapacitors

By using these three approaches, this study aims to enhance the understanding of the factors that influence MXene-based supercapacitor performance and to establish a comparative framework that places our work within the broader field of existing research. The insights gained from this analysis contribute to the ongoing development of high-performance energy storage systems utilizing MXene materials.

The details about the key works published in the literature, compared with the findings presented in sections 5.1-5.3, are provided in the following section.

MXene-Enabled Impurities (TiC)-based Supercapacitors: The TiC-based supercapacitors developed in this study demonstrate a maximum specific capacitance of 79 F/g (197 mF/cm^2) and an energy density of 44 Wh/kg (109.5 mWh/cm^2). Table 5.7 provides a comparison of the capacitance values for TiC- and TiS-based supercapacitors reported in the literature, alongside the capacitance results of TiC-based supercapacitors using gel electrolytes obtained in this work.

Table 5.7 Comparison of Capacitance and Energy density of TiC-based supercapacitors reported in our work with the literature.

Device	**Specific Capacitance**	**Energy density**	**Ref.**
TiC nanotube arrays	27.6 mF/cm^2	4.5 µWh /cm^2	[137]
TiC nanotube arrays	53.3 mF/cm^2	4.6 mWh /cm^2	[138]
TiS_2/Ti	68.62 mF/cm^2	34.35 mWh /cm^2	[238]
TiC /AC	197mF/cm^2 79 F/g	109 mWh /cm^2 44Wh/kg	Current research

MXenes and Conducting Polymers Composites for Flexible Asymmetric Supercapacitors: Table 5.8 compares the specific capacitance and energy density values of different MXene-based asymmetric supercapacitors documented in previous studies with those obtained in the current research**.** Particularly, supercapacitors utilizing Metal selenides on MXene/g-C_3N_4 exhibit superior performance, showing specific capacitance and energy density of 60F/g and 10.1 Wh/kg, respectively [239]. The Co_3O_4-MXene-based asymmetric supercapacitor achieves an energy density of 10.41 Wh/kg [240]. This research presents two novel supercapacitor devices: a pBOA//Ti_3C_2Tx-PANI device shows specific capacitance of 153 F/g and an energy density of 7.6 Wh/kg, whereas the pBOA//Ti_3C_2Tx-PANI-PEDOT: PSS device outperformed it, achieving a capacitance of 279 F/g and an energy density of 13 Wh/kg. These results indicate that ternary composite-based devices fabricated in this work surpass MXene-based supercapacitors in both capacitance and energy storage performance.

Table 5.8 Comparison of Capacitance and Energy density of various MXene-based asymmetric supercapacitors from literature with our work

Device	Specific Capacitance	Energy density	Reference
80 wt%- MXene/CNT composite film	50 F/g	7.34 Wh /kg	[178]
MXene //MoS2@MXene	29 F/g	1.21 Wh /kg	[179]
MXene/graphitic carbon nitride-supported metal selenide	60 F/g	10.1 Wh /kg	[239]
Co_3O_4-MXene nanocomposite		10.41 Wh /kg	[240]
pBOA// $Ti_3C_2T_x$ -PANI	153 F/g	7.6 Wh /kg	Current research
pBOA// $Ti_3C_2T_x$ -PANI-PEDOT: PSS	279 F/g	13 Wh /kg	Current research

Quaternary MXene Composite (MXene-pBOA-NiO-rGO) for Improved Energy Storage in Symmetric Supercapacitors: In this study, we present a quaternary nanocomposite device with a 2 mm electrode spacing, demonstrating enhanced electrochemical performance. The results are compared with previous studies and summarized in Table 5.9. The d-Ti_3CN MXene-based supercapacitors achieved a capacitance of 41 F/g and an energy density of 5.7 Wh/kg [242]. The incorporation of polypyrrole (PPY) in MXene-based supercapacitors resulted in an energy density of 8.77 Wh/kg [243]. In another study, MXene is combined with carbon nanotubes (CNTs) in a Ni-based film structure to fabricate a supercapacitor and achieve an energy density of 14.5 Wh/kg [244]. The PANI/Ti_3C_2Tx-modified cotton (PTC) yarn-based supercapacitor showed a specific capacitance of 175.6 F/g and an energy density of 6.1 Wh/kg [245]. The present study introduces a novel MXene-pBOA-NiO-rGO composite, which significantly outperforms previously reported ones. With a specific capacitance of 338.4 F/g and an

energy density of 16.92 Wh/kg, this composite surpasses all previously reported materials. The outstanding performance is likely due to the synergistic interaction of MXene with NiO, rGO, and pBOA, which enhances charge storage capacity, conductivity, and electrochemical stability.

Table 5.9 Comparison of the Capacitance of various MXene-based symmetric supercapacitors with our work

Device	**Specific Capacitance**	**Energy density**	**Ref**
MX-ANF-NB	----------	9.4 Wh /kg	[241]
d-Ti_3CN MXene	41 F/g	5.7 Wh /kg	[242]
MXene/PPY	----------	8.77 W h/ kg	[243]
MXene/CNTs @Ni film	----------	14.5 Wh /kg	[244]
PANI/$Ti_3C_2T_x$ modified cotton (PTC) yarn	175.6F/g	6.1Wh/ kg	[245]
Polyaniline (PANI) hybridized $Ti_3C_2T_x$ (PT) fiber	88.7F/g	2.5Wh/kg	[246]
Bacterial cellulose (BC)/$Ti_3C_2T_x$ (PBT) hybrid fiber	259 F/g	7.28 Wh /kg	[247]
MXene-pBOA-NiO-rGO	338.4 F/g	16.92312 Wh /kg	Current research

5.5 Summary

This study explores the design and creation of flexible, stretchable electrodes for advanced energy storage devices. This is achieved by using the unique features of MXene-based Titanium Carbide (TiC) impurities, which boost conductivity, stability, and overall electrochemical performance. Additionally, advanced polymer composites with MXenes are also created in binary, ternary, and quaternary forms, each providing better strength and adjustable electrochemical properties. By integrating MXene-based electrodes in both symmetric and asymmetric device architectures, this research aims to optimize energy storage performance. The symmetric configuration, where identical electrode materials are used, ensures balanced charge distribution and extended cycling stability. Meanwhile, the asymmetric configuration, which combines different electrode materials, allows for a broader operating voltage window, leading to higher energy and power densities. These methods support the fabrication of durable, flexible, and high-performance energy storage solutions, addressing major challenges in today's electronics and energy systems.

Chapter 6 Conclusion and Future Work

This chapter provides a summary of the work earned and major findings, along with some discussion about the future directions of work, which may be important to understand the problem and solutions better.

6.1 Conclusion

This study primarily explored the development and fabrication of flexible, stretchable electrodes for energy storage. The compositions of MXenes are systematically varied to include pure MXenes, MXene-based composites, and electrodes with precisely controlled levels of MXene impurities. Integrating MXene-based electrodes in both symmetric and asymmetric configurations was found to enhance electrochemical performance, providing high conductivity, exceptional charge storage capacity, and improved mechanical stability and flexibility.

Some of the important highlights of the work are as follows.

a) Five different electrode materials were tested with three different gel electrolytes to evaluate their behavior and compatibility. TiC material was specifically used to study MXene impurities as a conducting material in supercapacitors. MXene-enabled TiC electrodes exhibited excellent electrochemical properties with N, N´-Dimethylacrylamide, and 2-Hydroxyethyl methacrylate electrolytes. The highest specific capacitance values recorded were 50 F/g with N, N´-Dimethylacrylamide, and 79 F/g with 2-Hydroxyethyl methacrylate.

b) Electrochemical Impedance Spectroscopy (EIS) was used to determine equivalent series resistance (Rs) with pure TiC electrodes showing the best performance using 2-Hydroxyethyl methacrylate (Rs = 72.09 Ω). Open circuit and short circuit tests

confirmed the best electrode compatibility with N, N′-Dimethylacrylamide electrolyte. The operating time of the electrodes with this electrolyte was approximately 30 minutes. TiC-based supercapacitors demonstrated a promising combination of electrode properties with novel electrolytes.

c) This study highlights the outstanding capabilities of MXene-based conducting polymer composites, especially the $Ti_3C_2T_x$-PANI-PEDOT: PSS composite as a high-performance electrode material for electrochemical energy storage applications. An asymmetric supercapacitor utilizing $Ti_3C_2T_x$-PANI-PEDOT: PSS achieved a notable specific capacitance of 279 F/g. The device retained 97% of its capacitance after undergoing 1,000 charge–discharge cycles at a current density of 1 A/g. Moreover, when four pBOA//$Ti_3C_2T_x$-PANI-PEDOT: PSS units were connected in series, they successfully powered small electronic devices, highlighting their suitability for flexible energy harvesting applications.

d) The flexible symmetric supercapacitor shows significant promise for the development of next-generation flexible electrochemical energy storage systems. These devices, made with standalone (pBOA), binary (pBOA-NiO), ternary (pBOA-NiO-rGO), and quaternary (MXene-pBOA-NiO-rGO) composites, demonstrated excellent electrochemical performance, effectively overcoming several issues noted in recent studies.

e) Electrochemical analysis, including cyclic voltammetry, galvanostatic charge-discharge, and electrochemical impedance spectroscopy, verified the supercapacitors' stability and performance in all cases. With an electrode spacing of 2 mm, the quaternary nanocomposite device achieved a specific capacitance of 338.4 F/g and an energy density of 16.9 Wh/kg.

These findings mark a significant step forward in the practical development of efficient wearable electronics. This study enhances insight into MXene-based flexible supercapacitors and presents a viable strategy for creating self-sustaining, flexible energy storage systems.

6.2 Directions for Future Work

Future research will focus on developing novel strategies to enhance porosity, increase the effective surface area, and reduce restacking in MXene-based electrodes. Some of the ideas are summarized.

- **Chemical etching and intercalation methods**: Utilizing strong acid or base treatments can introduce micropores and mesopores, improving charge storage and electrolyte accessibility.
- **Janus MXenes**: Designing asymmetric MXenes with distinct chemical terminations on each side may enhance surface reactivity and charge storage capability.
- **Integration with conductive polymers or carbon-based materials**: This approach can prevent stacking while maintaining high electrical conductivity and mechanical stability.

As wearable electronics continue to advance, there is a growing need for supercapacitors that are flexible and lightweight. MXenes have demonstrated potential in textile-based energy storage systems, but there are still several aspects that need to be further researched:

- **Scalability and manufacturing techniques:** Maintaining consistent MXene properties across different batches remains difficult, affecting device uniformity. The use of toxic chemicals and low material yields increases costs and

environmental risks. Developing affordable, scalable synthesis methods for MXene-coated fabrics is essential for commercialization. Future efforts should focus on eco-friendly approaches, replacing hazardous HF etching with safer alternatives like electrochemical or molten salt etching to enable sustainable production. Implementing roll-to-roll manufacturing can support continuous MXene film production, vital for large-scale output. Incorporating automation, AI, and robotics can improve reproducibility, minimize human error, and streamline manufacturing processes. Additionally, conducting thorough lifecycle assessments of environmental impact, energy use, and costs is crucial for sustainable commercial adoption. These strategies are key to moving MXenes from laboratory research to practical, industrial energy storage solutions.

- **Long-term stability and durability**: MXene-based textile supercapacitors show great potential for wearable electronics because of their high conductivity and flexibility. However, their long-term performance in real-world scenarios is still a concern. To make these devices practical, they must undergo thorough testing under repeated mechanical stresses like bending and stretching, which are typical in clothing and wearables. Washing resistance is also crucial, as water and detergent exposure can impair performance or lead to delamination of active materials. Such tests are vital to evaluate the mechanical strength, electrochemical stability, and adhesion of MXene films on textile substrates. Achieving durability under these conditions is essential for creating washable and flexible energy storage solutions integrated into smart fabrics.

- **Electrolyte compatibility**: A major challenge with MXene-based supercapacitors is ensuring compatibility with different electrolytes. $Ti_3C_2T_x$ MXenes are particularly prone to oxidation in aqueous electrolytes, leading to a notable decline in their electrochemical performance over time. Such systems also limit the voltage range, which reduces energy density. When using organic or ionic liquid electrolytes, interface stability becomes an issue, as weak interactions between the electrode and electrolyte hinder charge transfer. Moreover, the large ions in ionic liquids may find it difficult to intercalate into MXene layers, decreasing capacitance and rate performance. These challenges emphasize the need for developing new electrolytes and surface treatments to fully energy storage capabilities of MXenes. Advances in gel or polymer electrolytes that offer high ionic conductivity and mechanical flexibility are vital for wearable devices. Additionally, protective coatings or barrier layers that prevent oxidation without hindering ion access are crucial areas for further research.
- **Flexibility:** Although MXene films are ultrathin and two-dimensional, they can be brittle and prone to delamination with repeated bending, which challenges their application in flexible and wearable supercapacitors. A key issue is substrate compatibility, as MXenes often do not adhere well to flexible materials like PET or textiles, leading to mechanical instability and compromised device integrity. Additionally, electrochemical degradation under mechanical strain is a concern; ongoing deformation can create microcracks in the electrode, causing conductivity loss and reduced capacitance over time. These issues underscore the importance of developing better material integration and mechanical reinforcement methods to preserve flexibility and electrochemical performance in MXene-based energy

storage devices. Future research should focus on optimizing these factors to produce durable, high-performance flexible supercapacitors suitable for real-world use. This includes exploring MXene-based fibers and inks for wearable electronics and establishing testing protocols under actual bending and twisting conditions.

References

[1] L. da Silva Lima *et al.*, "Life cycle assessment of lithium-ion batteries and vanadium redox flow batteries-based renewable energy storage systems," *Sustain. Energy Technol. Assessments*, vol. 46, p. 101286, Aug. 2021, doi: 10.1016/J.SETA.2021.101286.

[2] M. Kiehbadroudinezhad, A. Merabet, and H. Hosseinzadeh-Bandbafha, "Review of Latest Advances and Prospects of Energy Storage Systems: Considering Economic, Reliability, Sizing, and Environmental Impacts Approach," *Clean Technol.*, vol. 4, no. 2, pp. 477–501, Jun. 2022, doi: 10.3390/CLEANTECHNOL4020029.

[3] S. P. Neill, M. R. Hashemi, and M. J. Lewis, "Tidal energy leasing and tidal phasing," *Renew. Energy*, vol. 85, pp. 580–587, Jan. 2016, doi: 10.1016/J.RENENE.2015.07.016.

[4] P. G. Machado, D. Mouette, R. Rathmann, E. dos Santos, and D. Peyerl, "Is Energy Planning Moving Towards Sustainable Development? A Review of Energy Systems Modeling and Their Focus on Sustainability," *World Sustain. Ser.*, pp. 629–644, 2020, doi: 10.1007/978-3-030-26759-9_36.

[5] S. Haider *et al.*, "Enhanced Energy Density of PANI/Co3O4/Graphene Ternary Nanocomposite in a Neutral Aqueous Electrolyte of Na2SO4 for Supercapacitor Applications," *J. Electron. Mater.*, vol. 51, no. 9, pp. 5417–5428, Sep. 2022, doi: 10.1007/S11664-022-09788-0.

[6] S. Haider, R. Abid, I. Murtaza, A. Shuja, A. Basit, and M. A. Asghar, "Exploring the Synergistic Effect of a PANI/Cr2O3/Graphene Nanocomposite in a Hybrid Gel Electrolyte for Supercapacitor Performance," *J. Electron. Mater.*, vol. 52, no. 11, pp. 7576–7589, Nov. 2023, doi: 10.1007/S11664-023-10686-2/FIGURES/8.

[7] H. Ibrahim, A. Ilinca, and J. Perron, "Energy storage systems-Characteristics and comparisons," *Renew. Sustain. Energy Rev.*, vol. 12, no. 5, pp. 1221–1250, Jun. 2008, doi: 10.1016/j.rser.2007.01.023.

[8] M. Winter and R. J. Brodd, "What are batteries, fuel cells, and supercapacitors?," *Chem. Rev.*, vol. 104, no. 10, pp. 4245–4269, 2004, doi: 10.1021/cr020730k.

[9] G. R. Timilsina, L. Kurdgelashvili, and P. A. Narbel, "Solar energy: Markets, economics and policies," *Renew. Sustain. Energy Rev.*, vol. 16, no. 1, pp. 449–465, Jan. 2012, doi: 10.1016/J.RSER.2011.08.009.

[10] D. A. Elalfy, E. Gouda, M. F. Kotb, V. Bureš, and B. E. Sedhom, "Comprehensive review of energy storage systems technologies, objectives, challenges, and future trends," *Energy Strateg. Rev.*, vol. 54, p. 101482, Jul. 2024, doi: 10.1016/J.ESR.2024.101482.

[11] S. Rehman, M. A. Bader, and S. A. Al-Moallem, "Cost of solar energy generated using PV panels," *Renew. Sustain. Energy Rev.*, vol. 11, no. 8, pp. 1843–1857, 2007, https://doi.org/10.1016/j.rser.2006.03.005

[12] M. R. Islam, S. Mekhilef, and R. Saidur, "Progress and recent trends of wind energy technology," *Renew. Sustain. Energy Rev.*, vol. 21, pp. 456–468, May 2013, doi: 10.1016/J.RSER.2013.01.007.

[13] H. T. A. Awan *et al.*, "MXene-polymer hybrid composites for advanced energy storage: Insights into supercapacitors and batteries," *J. Energy Storage*, vol. 95, p. 112449, Aug. 2024, doi: 10.1016/J.EST.2024.112449.

[14] M. Winter and R. J. Brodd, “What are batteries, fuel cells, and supercapacitors?,” *Chem. Rev.*, vol. 104, no. 10, pp. 4245–4269, Oct. 2004, doi: 10.1021/CR020730K.
[15] Shukla AK, Sampath S, Vijayamohanan K. “Electrochemical supercapacitors: Energy storage beyond batteries.” *Current science*, vol. 79, no. 12, pp. 1656-1661, DEC. 2000,http://www.jstor.org/stable/24104124
[16] C. Meng, O. Z. Gall, and P. P. Irazoqui, “A flexible super-capacitive solid-state power supply for miniature implantable medical devices,” *Biomed. Microdevices*, vol. 15, no. 6, pp. 973–983, Dec. 2013, doi: 10.1007/S10544-013-9789-1/FIGURES/7.
[17] W. Raza *et al.*, “Recent advancements in supercapacitor technology,” *Nano Energy*, vol. 52, no. July, pp. 441–473, 2018, doi: 10.1016/j.nanoen.2018.08.013.
[18] A. Dutta, S. Mitra, M. Basak, and T. Banerjee, “A comprehensive review on batteries and supercapacitors: Development and challenges since their inception,” *Energy Storage*, vol. 5, no. 1, p. e339, Feb. 2023, doi: 10.1002/EST2.339.
[19] K. Dissanayake and D. Kularatna-Abeywardana, “A review of supercapacitors: Materials, technology, challenges, and renewable energy applications,” *J. Energy Storage*, vol. 96, p. 112563, Aug. 2024, doi: 10.1016/J.EST.2024.112563.
[20] P. Simon, Y. Gogotsi, and B. Dunn, “Where Do Batteries End and Supercapacitors Begin?,” *Science (80-.).*, vol. 343, no. 6176, pp. 1210–1211, Mar. 2014, doi: 10.1126/SCIENCE.1249625.
[21] W. J. Liu, H. Jiang, and H. Q. Yu, “Emerging applications of biochar-based materials for energy storage and conversion,” *Energy Environ. Sci.*, vol. 12, no. 6, pp. 1751–1779, Jun. 2019, doi: 10.1039/C9EE00206E.
[22] Z. Zhu *et al.*, “Versatile carbon-based materials from biomass for advanced electrochemical energy storage systems,” *eScience*, vol. 4, no. 5, p. 100249, Oct. 2024, doi: 10.1016/J.ESCI.2024.100249.
[23] J. Zhang, M. Gu, and X. Chen, “Supercapacitors for renewable energy applications: A review,” *Micro Nano Eng.*, vol. 21, p. 100229, Dec. 2023, doi: 10.1016/J.MNE.2023.100229.
[24] B. H. Xiao, K. Xiao, J. X. Li, C. F. Xiao, S. Cao, and Z. Q. Liu, “Flexible electrochemical energy storage devices and related applications: recent progress and challenges,” *Chem. Sci.*, vol. 15, no. 29, pp. 11229–11266, Jul. 2024, doi: 10.1039/D4SC02139H.
[25] A. G. Olabi, Q. Abbas, A. Al Makky, and M. A. Abdelkareem, “Supercapacitors as next generation energy storage devices: Properties and applications,” *Energy*, vol. 248, p. 123617, 2022, doi: 10.1016/j.energy.2022.123617.
[26] S. Najib and E. Erdem, “Current progress achieved in novel materials for supercapacitor electrodes: Mini review,” *Nanoscale Adv.*, vol. 1, no. 8, pp. 2817–2827, 2019, doi: 10.1039/c9na00345b.
[27] G. Wang, L. Zhang, and J. Zhang, “A review of electrode materials for electrochemical supercapacitors,” *Chem. Soc. Rev.*, vol. 41, no. 2, pp. 797–828, Jan. 2012, doi: 10.1039/C1CS15060J.
[28] A. González, E. Goikolea, J. A. Barrena, and R. Mysyk, “Review on supercapacitors: Technologies and materials,” *Renew. Sustain. Energy Rev.*, vol. 58, pp. 1189–1206, May 2016, doi: 10.1016/J.RSER.2015.12.249.
[29] Poonam, K. Sharma, A. Arora, and S. K. Tripathi, “Review of supercapacitors: Materials and devices,” *J. Energy Storage*, vol. 21, pp. 801–825, Feb. 2019, doi: 10.1016/J.EST.2019.01.010.

[30] D. Larcher and J. M. Tarascon, “Towards greener and more sustainable batteries for electrical energy storage,” *Nat. Chem. 2014 71*, vol. 7, no. 1, pp. 19–29, Nov. 2014, doi: 10.1038/nchem.2085.
[31] X. Hong, J. He, C. Duan, G. Wang, and B. Liang, “Recent advance in electrochemically activated supercapacitors: Activation mechanisms, electrode materials and prospects,” *Renew. Sustain. Energy Rev.*, vol. 209, p. 115134, Mar. 2025, doi: 10.1016/J.RSER.2024.115134.
[32] S. Yasami, S. Mazinani, and M. Abdouss, “Developed composites materials for flexible supercapacitors electrode: ‘Recent progress & future aspects,’” *J. Energy Storage*, vol. 72, p. 108807, Nov. 2023, doi: 10.1016/J.EST.2023.108807.
[33] S. H. Nagarajarao *et al.*, “Recent Developments in Supercapacitor Electrodes: A Mini Review,” *ChemEngineering*, vol. 6, no. 1, 2022, doi: 10.3390/chemengineering6010005.
[34] M. E. Şahin, F. Blaabjerg, and A. Sangwongwanich, “A Comprehensive Review on Supercapacitor Applications and Developments,” *Energies 2022, Vol. 15, Page 674*, vol. 15, no. 3, p. 674, Jan. 2022, doi: 10.3390/EN15030674.
[35] S. J. Panchu, K. Raju, and H. C. Swart, “Emerging Two–Dimensional Intercalation Pseudocapacitive Electrodes for Supercapacitors,” *ChemElectroChem*, vol. 11, no. 15, p. e202300810, Aug. 2024, doi: 10.1002/CELC.202300810.
[36] P. Cudazzo, L. Sponza, C. Giorgetti, L. Reining, F. Sottile, and M. Gatti, “Exciton band structure in two-dimensional materials,” *Phys. Rev. Lett.*, vol. 116, no. 6, pp. 1–6, 2016, doi: 10.1103/PhysRevLett.116.066803.
[37] O. Folorunso, N. Kumar, Y. Hamam, R. Sadiku, and S. S. Ray, “Recent progress on 2D metal carbide/nitride (MXene) nanocomposites for lithium-based batteries,” *FlatChem*, vol. 29, no. September, p. 100281, 2021, doi: 10.1016/j.flatc.2021.100281.
[38] B. Ahmed, “Surface Modification of MXenes: A Pathway to Improve MXene Electrode Performance in Electrochemical Energy Storage Devices,” Dec. 2017, doi: 10.25781/KAUST-3UF69.
[39] S. Ali *et al.*, “Two-dimensional MXene based innovative electrode materials for supercapacitors: Recent advances and prospects,” *Fuel*, vol. 377, p. 132783, Dec. 2024, doi: 10.1016/J.FUEL.2024.132783.
[40] A. U. Ammar, I. D. Yildirim, F. Bakan, and E. Erdem, “ZnO and MXenes as electrode materials for supercapacitor devices,” *Beilstein J. Nanotechnol.*, vol. 12, pp. 49–57, 2021, doi: 10.3762/BJNANO.12.4.
[41] B. Anasori, M. R. Lukatskaya, and Y. Gogotsi, “2D metal carbides and nitrides (MXenes) for energy storage,” *Nat. Rev. Mater.*, vol. 2, no. 2, 2017, doi: 10.1038/natrevmats.2016.98.
[42] M. Naguib *et al.*, “Two-dimensional transition metal carbides,” *ACS Nano*, vol. 6, no. 2, pp. 1322–1331, 2012, doi: 10.1021/nn204153h.
[43] M. Naguib *et al.*, “Two-dimensional nanocrystals produced by exfoliation of Ti 3AlC 2,” *Adv. Mater.*, vol. 23, no. 37, pp. 4248–4253, 2011, doi: 10.1002/adma.201102306.
[44] M. M. Baig, I. H. Gul, S. M. Baig, and F. Shahzad, “2D MXenes: Synthesis, properties, and electrochemical energy storage for supercapacitors – A review,” *J. Electroanal. Chem.*, vol. 904, no. June 2021, p. 115920, 2022, doi: 10.1016/j.jelechem.2021.115920.

[45] D. Ribeiro dos Santos, “2D Ti3C2Tx MXenes for electrochemical energy storage,” p. 255, Nov. 2020, doi: 10.34894/VQ1DJA.
[46] Y. Gogotsi and B. Anasori, “The Rise of MXenes,” *ACS Nano*, vol. 13, no. 8, pp. 8491–8494, 2019, doi: 10.1021/acsnano.9b06394.
[47] X. Pan, T. Shao, X. Zheng, Y. Zhang, X. Ma, and Q. Zhang, “Energy and sustainable development nexus: A review,” *Energy Strateg. Rev.*, vol. 47, p. 101078, May 2023, doi: 10.1016/J.ESR.2023.101078.
[48] R. Kötz and M. Carlen, “Principles and applications of electrochemical capacitors,” *Electrochim. Acta*, vol. 45, no. 15–16, pp. 2483–2498, May 2000, doi: 10.1016/S0013-4686(00)00354-6.
[49] H. J. Becker, “Low voltage electrolytic capacitor,” Apr. 1954.
[50] M. Endo, T. Takeda, Y. J. Kim, K. Koshiba, and K. Ishii, “High Power Electric Double Layer Capacitor (EDLC’s); from Operating Principle to Pore Size Control in Advanced Activated Carbons,” *Carbon Lett.*, vol. 1, no. 3_4, pp. 117–128, 2001.
[51] S. Hadz¯i-Jordanov, H. Angerstein-Kozlowska, M. Vukovič, and B. E. Conway, “Reversibility and Growth Behavior of Surface Oxide Films at Ruthenium Electrodes,” *J. Electrochem. Soc.*, vol. 125, no. 9, pp. 1471–1480, Sep. 1978, doi: 10.1149/1.2131698/PDF.
[52] M. Yaseen *et al.*, “A review of supercapacitors: Materials design, modification, and applications,” *Energies*, vol. 14, no. 22, pp. 1–40, 2021, doi: 10.3390/en14227779.
[53] Y. A. Kumar, N. Roy, T. Ramachandran, M. Hussien, M. Moniruzzaman, and S. W. Joo, “Shaping the future of energy: The rise of supercapacitors progress in the last five years,” *J. Energy Storage*, vol. 98, p. 113040, Sep. 2024, doi: 10.1016/J.EST.2024.113040.
[54] A. Shuja *et al.*, “Supercapacitors for energy storage applications: Materials, devices and future directions: A comprehensive review,” *J. Alloys Compd.*, vol. 1009, p. 176924, Dec. 2024, doi: 10.1016/J.JALLCOM.2024.176924.
[55] S. Faraji and F. N. Ani, “The development of supercapacitor from activated carbon by electroless plating—A review,” *Renew. Sustain. Energy Rev.*, vol. 42, pp. 823–834, Feb. 2015, doi: 10.1016/J.RSER.2014.10.068.
[56] Y. Zhang *et al.*, “Progress of electrochemical capacitor electrode materials: A review,” *Int. J. Hydrogen Energy*, vol. 34, no. 11, pp. 4889–4899, Jun. 2009, doi: 10.1016/J.IJHYDENE.2009.04.005.
[57] “Wasterlain, Sébastien, et al. "Hybrid power source with batteries and supercapacitor for vehicle applications." *Proceedings of the ESCAP* 6 (2006)
[58] M. V. Kiamahalleh, S. H. S. Zein, G. Najafpour, S. A. Sata, and S. Buniran, “Multiwalled carbon nanotubes based nanocomposites for supercapacitors: A review of electrode materials,” *Nano*, vol. 7, no. 2, Apr. 2012, doi: 10.1142/S1793292012300022.
[59] V. S. Marin Halper James C Ellenbogen, “Supercapacitors: A Brief Overview MITRE,” 2006
[60] Z. S. Iro, C. Subramani, and S. S. Dash, “A Brief Review on Electrode Materials for Supercapacitor,” *Int. J. Electrochem. Sci.*, vol. 11, no. 12, pp. 10628–10643, Dec. 2016, doi: 10.20964/2016.12.50.
[61] H. Wang *et al.*, “In situ NMR spectroscopy of supercapacitors: Insight into the charge storage mechanism,” *J. Am. Chem. Soc.*, vol. 135, no. 50, pp. 18968–18980, Dec. 2013, doi: 10.1021/JA410287S/SUPPL_FILE/JA410287S_SI_003.MPG.

[62] B. E. Conway, V. Birss, and J. Wojtowicz, “The role and utilization of pseudocapacitance for energy storage by supercapacitors,” *J. Power Sources*, vol. 66, no. 1–2, pp. 1–14, May 1997, doi: 10.1016/S0378-7753(96)02474-3.

[63] S. Sharma and P. Chand, “Supercapacitor and electrochemical techniques: A brief review,” *Results Chem.*, vol. 5, no. November 2022, p. 100885, 2023, doi: 10.1016/j.rechem.2023.100885.

[64] J. W. Long, D. Bélanger, T. Brousse, W. Sugimoto, M. B. Sassin, and O. Crosnier, “Asymmetric electrochemical capacitors-Stretching the limits of aqueous electrolytes,” *MRS Bull. • Vol.*, vol. 36, 2011, doi: 10.1557/mrs.2011.137.

[65] X. Chen, R. Paul, and L. Dai, “Carbon-based supercapacitors for efficient energy storage,” *Natl. Sci. Rev.*, vol. 4, pp. 453–489, 2017, doi: 10.1093/nsr/nwx009.

[66] S. Najib and E. Erdem, “Current progress achieved in novel materials for supercapacitor electrodes: mini review,” *Nanoscale Adv.*, vol. 1, no. 8, pp. 2817–2827, Aug. 2019, doi: 10.1039/C9NA00345B.

[67] F. Béguin, V. Presser, A. Balducci, and E. Frackowiak, “Carbons and electrolytes for advanced supercapacitors,” *Adv. Mater.*, vol. 26, no. 14, pp. 2219–2251, Apr. 2014, doi: 10.1002/ADMA.201304137.

[68] M. Demir, S. K. Saraswat, and R. B. Gupta, “Hierarchical nitrogen-doped porous carbon derived from lecithin for high-performance supercapacitors,” *RSC Adv.*, vol. 7, no. 67, pp. 42430–42442, 2017, doi: 10.1039/c7ra07984b.

[69] W. Raza *et al.*, “Recent advancements in supercapacitor technology,” *Nano Energy*, vol. 52, pp. 441–473, Oct. 2018, doi: 10.1016/J.NANOEN.2018.08.013.

[70] K. Zhang *et al.*, “Polyhydroxyalkanoate-Modified Bacterium Regulates Biomass Structure and Promotes Synthesis of Carbon Materials for High-Performance Supercapacitors,” *ChemSusChem*, vol. 12, no. 8, pp. 1732–1742, Apr. 2019, doi: 10.1002/CSSC.201802894.

[71] J. Cherusseri, D. Pandey, and J. Thomas, “Symmetric, Asymmetric, and Battery-Type Supercapacitors Using Two-Dimensional Nanomaterials and Composites,” *Batter. Supercaps*, vol. 3, no. 9, pp. 860–875, Sep. 2020, doi: 10.1002/BATT.201900230.

[72] Y. Shao *et al.*, “Design and Mechanisms of Asymmetric Supercapacitors,” *Chem. Rev.*, vol. 118, no. 18, pp. 9233–9280, Sep. 2018, doi: 10.1021/ACS.CHEMREV.8B00252/ASSET/IMAGES/MEDIUM/CR-2018-00252Z_0028.GIF.

[73] Mancera, J.J.C., Rengel, R., Pérez, A.Z., Manzano, F.S., López, E. and Andújar, J.M., 2020. “Hybrid Supercapacitors as a Promising Alternative for Hybrid Electric Vehicles Fueling”. *Proceedings of the Fomento de la Cultura Científica, Tecnológica y de Innovación en Ciudades Inteligentes (ScienCity 2020), Huelva, Spain*, pp.17-19,2020

[74] S. Yu *et al.*, “Battery-like supercapacitors from diamond networks and water-soluble redox electrolytes,” *J. Mater. Chem. A*, vol. 5, no. 4, pp. 1778–1785, Jan. 2017, doi: 10.1039/C6TA08607A.

[75] J. S. Shayeh, M. Sadeghinia, S. O. R. Siadat, A. Ehsani, M. Rezaei, and M. Omidi, “A novel route for electrosynthesis of CuCr2O4 nanocomposite with p-type conductive polymer as a high performance material for electrochemical supercapacitors,” *J. Colloid Interface Sci.*, vol. 496, pp. 401–406, Jun. 2017, doi: 10.1016/J.JCIS.2017.02.010.

[76] H. Meskher *et al.*, "Prospects of functionalized carbon nanotubes for supercapacitors applications," *Mater. Today Commun.*, vol. 38, p. 108517, Mar. 2024, doi: 10.1016/J.MTCOMM.2024.108517.
[77] F. Ahmad *et al.*, "Recent developments in transition metal oxide-based electrode composites for supercapacitor applications," *J. Energy Storage*, vol. 81, p. 110430, Mar. 2024, doi: 10.1016/J.EST.2024.110430.
[78] S. H. S. Pai, S. K. Pandey, E. J. J. Samuel, J. U. Jang, A. K. Nayak, and H. S. Han, "Recent advances in NiO-based nanostructures for energy storage device applications," *J. Energy Storage*, vol. 76, p. 109731, Jan. 2024, doi: 10.1016/J.EST.2023.109731.
[79] H. Chen, L. Hu, M. Chen, Y. Yan, and L. Wu, "Nickel-cobalt layered double hydroxide nanosheets for high-performance supercapacitor electrode materials," *Adv. Funct. Mater.*, vol. 24, no. 7, pp. 934–942, Feb. 2014, doi: 10.1002/ADFM.201301747.
[80] I. Shown, A. Ganguly, L. C. Chen, and K. H. Chen, "Conducting polymer-based flexible supercapacitor," *Energy Sci. Eng.*, vol. 3, no. 1, pp. 2–26, Jan. 2015, doi: 10.1002/ESE3.50.
[81] R. Ramya, R. Sivasubramanian, and M. V. Sangaranarayanan, "Conducting polymers-based electrochemical supercapacitors—Progress and prospects," *Electrochim. Acta*, vol. 101, pp. 109–129, Jul. 2013, doi: 10.1016/J.ELECTACTA.2012.09.116.
[82] Y. Ma *et al.*, "Three-dimensional core-shell Fe3O4/Polyaniline coaxial heterogeneous nanonets: Preparation and high performance supercapacitor electrodes," *Electrochim. Acta*, vol. 315, pp. 114–123, Aug. 2019, doi: 10.1016/J.ELECTACTA.2019.05.073.
[83] P. R. Das, L. Komsiyska, O. Osters, and G. Wittstock, "PEDOT: PSS as a Functional Binder for Cathodes in Lithium Ion Batteries," *J. Electrochem. Soc.*, vol. 162, no. 4, pp. A674–A678, Jan. 2015, doi: 10.1149/2.0581504JES/XML.
[84] L. Qin *et al.*, "High-Performance Ultrathin Flexible Solid-State Supercapacitors Based on Solution Processable Mo1.33C MXene and PEDOT:PSS," *Adv. Funct. Mater.*, vol. 28, no. 2, pp. 1–8, 2018, doi: 10.1002/adfm.201703808.
[85] C. Liu, Z. Yu, D. Neff, A. Zhamu, and B. Z. Jang, "Graphene-based supercapacitor with an ultrahigh energy density," *Nano Lett.*, vol. 10, no. 12, pp. 4863–4868, Dec. 2010, doi: 10.1021/NL102661Q/SUPPL_FILE/NL102661Q_SI_001.PDF.
[86] R. Gautam, N. Marriwala, and R. Devi, "A review: Study of Mxene and graphene together," *Meas. Sensors*, vol. 25, 2023, doi: 10.1016/j.measen.2022.100592.
[87] T. Y. Kim *et al.*, "High-performance supercapacitors based on poly(ionic liquid)-modified graphene electrodes," *ACS Nano*, vol. 5, no. 1, p. 436, Jan. 2011, doi: 10.1021/nn101968p.
[88] G. P. Pandey and A. C. Rastogi, "Graphene-based all-solid-state supercapacitor with ionic liquid gel polymer electrolyte," *Mater. Res. Soc. Symp. Proc.*, vol. 1440, no. 1, pp. 7–12, Apr. 2012, doi: 10.1557/OPL.2012.1279/METRICS.
[89] F. Ahmad *et al.*, "Advances in graphene-based electrode materials for high-performance supercapacitors: A review," *J. Energy Storage*, vol. 72, p. 108731, Nov. 2023, doi: 10.1016/J.EST.2023.108731.
[90] F. Wang *et al.*, "Advances in molten-salt-assisted synthesis of 2D MXenes and their applications in electrochemical energy storage and conversion," *Chem. Eng. J.*, vol.

470, p. 144185, 2023.
[91] S. A. Kadam, K. P. Kadam, and N. R. Pradhan, “Advancements in 2D MXene-based supercapacitor electrodes: synthesis, mechanisms, electronic structure engineering, flexible wearable energy storage for real-world applications, and future prospects,” *J. Mater. Chem. A*, vol. 12, no. 29, pp. 17992–18046, Jul. 2024, doi: 10.1039/D4TA00328D.
[92] Q. Zhu, J. Li, P. Simon, and B. Xu, “Two-dimensional MXenes for electrochemical capacitor applications: Progress, challenges and perspectives,” *Energy Storage Mater.*, vol. 35, no. November 2020, pp. 630–660, 2021, doi: 10.1016/j.ensm.2020.11.035.
[93] M. R. Lukatskaya *et al.*, “Ultra-high-rate pseudocapacitive energy storage in two-dimensional transition metal carbides,” *Nat. Energy*, vol. 6, 2017, doi: 10.1038/nenergy.2017.105.
[94] A. Nashim and K. Parida, “A Glimpse on the plethora of applications of prodigious material MXene,” *Sustain. Mater. Technol.*, vol. 32, Jul. 2022, doi: 10.1016/j.susmat.2022.e00439.
[95] J. Pang *et al.*, “Applications of 2D MXenes in energy conversion and storage systems,” *Chem. Soc. Rev.*, vol. 48, no. 1, pp. 72–133, 2019, doi: 10.1039/c8cs00324f.
[96] T. Hu, J. Yang, W. Li, X. Wang, and C. M. Li, “Quantifying the rigidity of 2D carbides (MXenes),” *Phys. Chem. Chem. Phys.*, vol. 22, no. 4, pp. 2115–2121, 2020, doi: 10.1039/c9cp05412j.
[97] R. Cheng *et al.*, “MXenes induce epitaxial growth of size-controlled noble nanometals: A case study for surface enhanced Raman scattering (SERS),” *J. Mater. Sci. Technol.*, vol. 40, pp. 119–127, 2020, doi: 10.1016/j.jmst.2019.09.013.
[98] C. Zhong, Y. Deng, W. Hu, J. Qiao, L. Zhang, and J. Zhang, “A review of electrolyte materials and compositions for electrochemical supercapacitors,” *Chem. Soc. Rev.*, vol. 44, no. 21, pp. 7484–7539, Oct. 2015, doi: 10.1039/C5CS00303B.
[99] V. A. Tran, N. T. Tran, V. D. Doan, T. Q. Nguyen, H. H. P. Thi, and G. N. L. Vo, “Application Prospects of MXenes Materials Modifications for Sensors,” *Micromachines 2023, Vol. 14, Page 247*, vol. 14, no. 2, p. 247, Jan. 2023, doi: 10.3390/MI14020247.
[100] W. Hong, B. C. Wyatt, S. K. Nemani, and B. Anasori, “Double transition-metal MXenes: Atomistic design of two-dimensional carbides and nitrides,” *MRS Bull.*, vol. 45, no. 10, pp. 850–861, 2020, doi: 10.1557/mrs.2020.251.
[101] M. Shen *et al.*, “One-Pot Green Process to Synthesize MXene with Controllable Surface Terminations using Molten Salts,” *Angew. Chemie - Int. Ed.*, vol. 60, no. 52, pp. 27013–27018, 2021, doi: 10.1002/anie.202110640.
[102] M. Sokol, V. Natu, S. Kota, and M. W. Barsoum, “On the Chemical Diversity of the MAX Phases,” *Trends Chem.*, vol. 1, no. 2, pp. 210–223, 2019, doi: 10.1016/j.trechm.2019.02.016.
[103] S. Jin, Q. Hu, and A. Zhou, “Composition and hydrogen storage structure of Ti2CTx MXene with ultrahigh hydrogen storage capacity,” arXiv preprint arXiv: 2104.12930, 2021
[104] B. Scheibe, V. Kupka, B. Peplińska, M. Jarek, and K. Tadyszak, “The Influence of Oxygen Concentration during MAX Phases (Ti 3 AlC 2) Preparation on the αAl 2 O 3 Microparticles Content and Specific Surface Area of Multilayered MXenes (Ti

3 C 2 T x)," *Materials (Basel).*, vol. 12, no. 3, Jan. 2019, doi: 10.3390/MA12030353.
[105] H. Zhou *et al.*, "Two-dimensional molybdenum carbide 2D-Mo2C as a superior catalyst for CO2 hydrogenation," *Nat. Commun.*, vol. 12, no. 1, pp. 1–10, 2021, doi: 10.1038/s41467-021-25784-0.
[106] P. A. Maughan, "Porous two-dimensional materials (MXenes) for high capacity energy storage Submitted by Philip Adam Maughan , MChem For the degree of Doctor of Philosophy," no. September, 2019.
[107] T. S. Mathis *et al.*, "Modified MAX Phase Synthesis for Environmentally Stable and Highly Conductive Ti3C2MXene," *ACS Nano*, vol. 15, no. 4, pp. 6420–6429, 2021, doi: 10.1021/acsnano.0c08357.
[108] C. E. Shuck *et al.*, "Effect of Ti3AlC2 MAX Phase on Structure and Properties of Resultant Ti3C2Tx MXene," *ACS Appl. Nano Mater.*, vol. 2, no. 6, pp. 3368–3376, 2019, doi: 10.1021/acsanm.9b00286.
[109] M. Magnuson and M. Mattesini, "Chemical bonding and electronic-structure in MAX phases as viewed by X-ray spectroscopy and density functional theory," *Thin Solid Films*, vol. 621, pp. 108–130, 2017, doi: 10.1016/j.tsf.2016.11.005.
[110] R. M. Ronchi, J. T. Arantes, and S. F. Santos, "Synthesis, structure, properties and applications of MXenes: Current status and perspectives," *Ceram. Int.*, vol. 45, no. 15, pp. 18167–18188, 2019, doi: 10.1016/j.ceramint.2019.06.114.
[111] J. L. Hart *et al.*, "Control of MXenes' electronic properties through termination and intercalation," *Nat. Commun.*, vol. 10, no. 1, 2019, doi: 10.1038/s41467-018-08169-8.
[112] U. Fatima *et al.*, "Two-dimensional materials and synthesis, energy storage, utilization, and conversion applications of two-dimensional MXene materials," *Int. J. Energy Res.*, vol. 45, no. 7, pp. 9878–9894, 2021, doi: 10.1002/er.6595.
[113] X. Li, F. Ran, F. Yang, J. Long, and L. Shao, *Advances in MXene Films: Synthesis, Assembly, and Applications*, vol. 27, no. 3. Tianjin University, 2021. doi: 10.1007/s12209-021-00282-y.
[114] W. Zhao *et al.*, "Interlayer Hydrogen-Bonded Metal Porphyrin Frameworks/MXene Hybrid Film with High Capacitance for Flexible All-Solid-State Supercapacitors," *Small*, vol. 15, no. 18, pp. 1–10, 2019, doi: 10.1002/smll.201901351.
[115] K. Montazeri, M. Currie, L. Verger, P. Dianat, M. W. Barsoum, and B. Nabet, "Beyond Gold: Spin-Coated Ti3C2-Based MXene Photodetectors," *Adv. Mater.*, vol. 31, no. 43, pp. 1–9, 2019, doi: 10.1002/adma.201903271.
[116] K. Wang, Y. Zhou, W. Xu, D. Huang, Z. Wang, and M. Hong, "Fabrication and thermal stability of two-dimensional carbide Ti3C2 nanosheets," *Ceram. Int.*, vol. 42, no. 7, pp. 8419–8424, 2016, doi: 10.1016/j.ceramint.2016.02.059.
[117] L. Yan *et al.*, "Universal unilateral electro-spinning/spraying strategy to construct water-unidirectional Janus membranes with well-tuned hierarchical micro/nanostructures," *Chem. Commun.*, vol. 56, no. 3, pp. 478–481, 2020, doi: 10.1039/c9cc08088k.
[118] M. Q. Zhao *et al.*, "Flexible MXene/carbon nanotube composite paper with high volumetric capacitance," *Adv. Mater.*, vol. 27, no. 2, pp. 339–345, 2015, doi: 10.1002/adma.201404140.
[119] X. Sheng, Y. Zhao, L. Zhang, and X. Lu, "Properties of two-dimensional Ti3C2 MXene/thermoplastic polyurethane nanocomposites with effective reinforcement

via melt blending," *Compos. Sci. Technol.*, vol. 181, no. May, p. 107710, 2019, doi: 10.1016/j.compscitech.2019.107710.
[120] Z. Lv *et al.*, "Editable Supercapacitors with Customizable Stretchability Based on Mechanically Strengthened Ultralong MnO2 Nanowire Composite," *Adv. Mater.*, vol. 30, no. 2, pp. 1–9, 2018, doi: 10.1002/adma.201704531.
[121] Y. Tian, C. Yang, W. Que, X. Liu, X. Yin, and L. B. Kong, "Flexible and free-standing 2D titanium carbide film decorated with manganese oxide nanoparticles as a high volumetric capacity electrode for supercapacitor," *J. Power Sources*, vol. 359, pp. 332–339, 2017, doi: 10.1016/j.jpowsour.2017.05.081.
[122] M. Boota, B. Anasori, C. Voigt, M. Q. Zhao, M. W. Barsoum, and Y. Gogotsi, "Pseudocapacitive Electrodes Produced by Oxidant-Free Polymerization of Pyrrole between the Layers of 2D Titanium Carbide (MXene)," *Adv. Mater.*, vol. 28, no. 7, pp. 1517–1522, 2016, doi: 10.1002/adma.201504705.
[123] N. Choudhary *et al.*, "Asymmetric Supercapacitor Electrodes and Devices," *Adv. Mater.*, vol. 29, no. 21, Jun. 2017, doi: 10.1002/ADMA.201605336.
[124] X. Fang and D. Yao, "An overview of solid-like electrolytes for supercapacitors," *ASME Int. Mech. Eng. Congr. Expo. Proc.*, vol. 6 A, 2013, doi: 10.1115/IMECE2013-64069.
[125] A. Lewandowski, A. Olejniczak, M. Galinski, and I. Stepniak, "Performance of carbon–carbon supercapacitors based on organic, aqueous and ionic liquid electrolytes," *J. Power Sources*, vol. 195, no. 17, pp. 5814–5819, Sep. 2010, doi: 10.1016/J.JPOWSOUR.2010.03.082.
[126] X. Xu *et al.*, "MXenes with applications in supercapacitors and secondary batteries: A comprehensive review," *Mater. Reports Energy*, vol. 2, no. 1, p. 100080, 2022, doi: 10.1016/j.matre.2022.100080.
[127] V. Kamysbayev *et al.*, "Covalent surface modifications and superconductivity of two-dimensional metal carbide MXenes," *Science (80-.).*, vol. 369, no. 6506, pp. 979–983, 2020, doi: 10.1126/science.aba8311.
[128] M. Hu *et al.*, "Surface Functional Groups and Interlayer Water Determine the Electrochemical Capacitance of Ti3C2 T x MXene," *ACS Nano*, vol. 12, no. 4, pp. 3578–3586, 2018, doi: 10.1021/acsnano.8b00676.
[129] C. (John) Zhang *et al.*, "Additive-free MXene inks and direct printing of micro-supercapacitors," *Nat. Commun.*, vol. 10, no. 1, pp. 1–9, 2019, doi: 10.1038/s41467-019-09398-1.
[130] Y. Chae *et al.*, "An investigation into the factors governing the oxidation of two-dimensional Ti 3 C 2 MXene," *Nanoscale*, vol. 11, no. 17, pp. 8387–8393, 2019, doi: 10.1039/c9nr00084d.
[131] V. Natu, J. L. Hart, M. Sokol, H. Chiang, M. L. Taheri, and M. W. Barsoum, "Edge Capping of 2D-MXene Sheets with Polyanionic Salts To Mitigate Oxidation in Aqueous Colloidal Suspensions," *Angew. Chemie - Int. Ed.*, vol. 58, no. 36, pp. 12655–12660, 2019, doi: 10.1002/anie.201906138.
[132] X. Xia *et al.*, "Tubular TiC fibre nanostructures as supercapacitor electrode materials with stable cycling life and wide-temperature performance," *Energy Environ. Sci.*, vol. 8, no. 5, pp. 1559–1568, May 2015, doi: 10.1039/C5EE00339C.
[133] T. Chen, M. Li, S. Song, P. Kim, and J. Bae, "Biotemplate preparation of multilayered TiC nanoflakes for high performance symmetric supercapacitor," *Nano Energy*, vol. 71, May 2020, doi: 10.1016/J.NANOEN.2020.104549.

[134] J. Li, J. Ao, C. Zhong, and R. Zhao, "Multidimensional carbon template preparation of 3D multilayered TiC nanoflakes for high performance symmetric supercapacitor," *J. Alloys Compd.*, vol. 872, p. 159690, 2021, doi: 10.1016/j.jallcom.2021.159690.
[135] W. Sen *et al.*, "Preparation of titanium carbide powders by carbothermal reduction of titania/charcoal at vacuum condition," *Int. J. Refract. Met. Hard Mater.*, vol. 28, no. 5, pp. 628–632, 2010, doi: 10.1016/j.ijrmhm.2010.06.005.
[136] W. Liu, J. L. Cheong, M. F. Ng, and J. Y. Ying, "Carbon nitride mediated synthesis of titanium-based electrodes for high-performance asymmetric supercapacitors," *Nano Energy*, vol. 112, p. 108489, Jul. 2023, doi: 10.1016/J.NANOEN.2023.108489.
[137] M. Hu, R. Tan, X. Jiang, M. Dong, L. Wen, and M. Hu, "Capture of CO2 during the Electrolysis Process and Its Utilization in Supercapacitor Materials," *ACS Omega*, vol. 9, no. 6, pp. 6888–6893, Feb. 2024, doi: 10.1021/ACSOMEGA.3C07587/ASSET/IMAGES/LARGE/AO3C07587_0007.JPEG..
[138] T. Ma *et al.*, "Synthesis of TiC nanotube arrays and their excellent supercapacitor performance," *J. Mater. Chem. A*, vol. 10, no. 18, pp. 9932–9940, May 2022, doi: 10.1039/D2TA00957A.
[139] A. Mateen *et al.*, "Ti2CTx–MXene aerogel based ultra–stable Zn–ion supercapacitor," *Compos. Commun.*, vol. 38, Feb. 2023, doi: 10.1016/J.COCO.2023.101493.
[140] S. Nahirniak, A. Ray, and B. Saruhan, "Challenges and Future Prospects of the MXene-Based Materials for Energy Storage Applications," *Batter. 2023, Vol. 9, Page 126*, vol. 9, no. 2, p. 126, Feb. 2023, doi: 10.3390/BATTERIES9020126.
[141] H. Aghamohammadi, N. Amousa, and R. Eslami-Farsani, "Recent advances in developing the MXene/polymer nanocomposites with multiple properties: A review study," *Synth. Met.*, vol. 273, p. 116695, Mar. 2021, doi: 10.1016/J.SYNTHMET.2020.116695.
[142] A. Muzaffar, K. Deshmukh, and M. B. Ahamed, "MXene-based multifunctional polymer composites for electromagnetic interference shielding applications," *MXenes their Compos. Synth. Prop. Potential Appl.*, pp. 649–686, Jan. 2021, doi: 10.1016/B978-0-12-823361-0.00006-X.
[143] K. Gong, K. Zhou, X. Qian, C. Shi, and B. Yu, "MXene as emerging nanofillers for high-performance polymer composites: A review," *Compos. Part B Eng.*, vol. 217, p. 108867, Jul. 2021, doi: 10.1016/J.COMPOSITESB.2021.108867.
[144] P. Forouzandeh and S. C. Pillai, "MXenes-based nanocomposites for supercapacitor applications," *Curr. Opin. Chem. Eng.*, vol. 33, p. 100710, Sep. 2021, doi: 10.1016/J.COCHE.2021.100710.
[145] R. Ma *et al.*, "Self-Supporting, Binder-Free, and Flexible Ti3C2TxMXene-Based Supercapacitor Electrode with Improved Electrochemical Performance," *ACS Nano*, vol. 16, no. 6, pp. 9713–9727, Jun. 2022, doi: 10.1021/ACSNANO.2C03351/SUPPL_FILE/NN2C03351_SI_001.PDF.
[146] T. Chen, M. Li, Y. Li, S. Song, J. Kim, and J. Bae, "Synthesis of hierarchical structure MXene/PANI composite hybrid electrodes for supercapacitors," *Mater. Sci. Eng. B*, vol. 290, p. 116354, Apr. 2023, doi: 10.1016/J.MSEB.2023.116354.
[147] X. Wang *et al.*, "Unveiling the potential: Asymmetric supercapacitors with conductive polymers/Ti3C2Tx/Ni3S4 electrodes deliver high energy densities,"

Electrochim. Acta, vol. 507, p. 145155, Dec. 2024, doi: 10.1016/J.ELECTACTA.2024.145155.
[148] W. Luo *et al.*, "Overview of MXene/conducting polymer composites for supercapacitors," *J. Energy Storage*, vol. 52, p. 105008, Aug. 2022, doi: 10.1016/J.EST.2022.105008.
[149] J. Zhou *et al.*, "Ultrahigh rate capability of 1D/2D polyaniline/titanium carbide (MXene) nanohybrid for advanced asymmetric supercapacitors," *Nano Res.*, vol. 15, no. 1, pp. 285–295, Jan. 2022, doi: 10.1007/S12274-021-3472-2/METRICS.
[150] S. M. Varghese, V. V. Mohan, S. Suresh, E. Bhoje Gowd, and R. B. Rakhi, "Synergistically modified Ti3C2Tx MXene conducting polymer nanocomposites as efficient electrode materials for supercapacitors," *J. Alloys Compd.*, vol. 973, p. 172923, Feb. 2024, doi: 10.1016/J.JALLCOM.2023.172923.
[151] H. Xu, D. Zheng, F. Liu, W. Li, and J. Lin, "Synthesis of an MXene/polyaniline composite with excellent electrochemical properties," *J. Mater. Chem. A*, vol. 8, no. 12, pp. 5853–5858, Mar. 2020, doi: 10.1039/D0TA00572J.
[152] I. Dědek *et al.*, "Maximizing the electrochemical performance of supercapacitor electrodes from plastic waste," *J. Energy Storage*, vol. 72, p. 108660, Nov. 2023, doi: 10.1016/J.EST.2023.108660.
[153] W. Zheng, J. Halim, P. O. Å. Persson, J. Rosen, and M. W. Barsoum, "MXene-based symmetric supercapacitors with high voltage and high energy density," *Mater. Reports Energy*, vol. 2, no. 1, p. 100078, 2022, doi: 10.1016/j.matre.2022.100078.
[154] Q. X. Xia *et al.*, "Seawater electrolyte-mediated high volumetric MXene-based electrochemical symmetric supercapacitors," *Dalt. Trans.*, vol. 47, no. 26, pp. 8676–8682, Jul. 2018, doi: 10.1039/C8DT01375F.
[155] C. Yang *et al.*, "Achieving of Flexible, Free-Standing, Ultracompact Delaminated Titanium Carbide Films for High Volumetric Performance and Heat-Resistant Symmetric Supercapacitors," *Adv. Funct. Mater.*, vol. 28, no. 15, Apr. 2018, doi: 10.1002/ADFM.201705487.
[156] W. Wu, C. Wang, C. Zhao, D. Wei, J. Zhu, and Y. Xu, "Facile strategy of hollow polyaniline nanotubes supported on Ti3C2-MXene nanosheets for High-performance symmetric supercapacitors," *J. Colloid Interface Sci.*, vol. 580, pp. 601–613, Nov. 2020, doi: 10.1016/J.JCIS.2020.07.052.
[157] Y. Zhou, Y. Zou, Z. Peng, C. Yu, and W. Zhong, "Arbitrary deformable and high-strength electroactive polymer/MXene anti-exfoliative composite films assembled into high performance, flexible all-solid-state supercapacitors," *Nanoscale*, vol. 12, no. 40, pp. 20797–20810, Oct. 2020, doi: 10.1039/D0NR04980H.
[158] Y. Zhou *et al.*, "Ti3C2Tx MXene-Reduced Graphene Oxide Composite Electrodes for Stretchable Supercapacitors," *ACS Nano*, vol. 14, no. 3, pp. 3576–3586, Mar. 2020, doi: 10.1021/acsnano.9b10066.
[159] J. Zhang *et al.*, "Highly Conductive Ti3C2Tx MXene Hybrid Fibers for Flexible and Elastic Fiber-Shaped Supercapacitors," *Small*, vol. 15, no. 8, p. 1804732, Feb. 2019, doi: 10.1002/SMLL.201804732.
[160] H. Hwang, S. Byun, S. Yuk, S. Kim, S. H. Song, and D. Lee, "High-rate electrospun Ti3C2Tx MXene/carbon nanofiber electrodes for flexible supercapacitors," *Appl. Surf. Sci.*, vol. 556, p. 149710, Aug. 2021, doi: 10.1016/J.APSUSC.2021.149710.
[161] H. Li *et al.*, "Laser crystallized sandwich-like MXene/Fe3O4/MXene thin film electrodes for flexible supercapacitors," *J. Power Sources*, vol. 497, p. 229882, Jun.

2021, doi: 10.1016/J.JPOWSOUR.2021.229882.
[162] Y. Luo, Y. Tang, X. Bin, C. Xia, and W. Que, "3D Porous Compact 1D/2D Fe2O3/MXene Composite Aerogel Film Electrodes for All-Solid-State Supercapacitors," *Small*, vol. 18, no. 48, p. 2204917, Dec. 2022, doi: 10.1002/SMLL.202204917.
[163] B. Mustafa *et al.*, "Ultrahigh Energy and Power Densities of d-MXene-Based Symmetric Supercapacitors," *Nanomaterials*, vol. 12, no. 19, pp. 1–11, 2022, doi: 10.3390/nano12193294.
[164] D. Kasprzak, C. C. Mayorga-Martinez, O. Alduhaish, and M. Pumera, "Wearable and Flexible All-Solid-State Supercapacitor Based on MXene and Chitin," *Energy Technol.*, vol. 11, no. 3, p. 2201103, Mar. 2023, doi: 10.1002/ENTE.202201103.
[165] W. Luo *et al.*, "Fabrication of Ti3C2Tx MXene/polyaniline composite films with adjustable thickness for high-performance flexible all-solid-state symmetric supercapacitors," *Electrochim. Acta*, vol. 406, p. 139871, Feb. 2022, doi: 10.1016/J.ELECTACTA.2022.139871.
[166] A. El Ghazaly *et al.*, "Enhanced supercapacitive performance of Mo1.33C MXene based asymmetric supercapacitors in lithium chloride electrolyte," *Energy Storage Mater.*, vol. 41, no. May, pp. 203–208, 2021, doi: 10.1016/j.ensm.2021.05.006.
[167] C. F. Du, X. Zhao, Z. Wang, H. Yu, and Q. Ye, "Recent advanced on the mxene–organic hybrids: Design, synthesis, and their applications," *Nanomaterials*, vol. 11, no. 1, pp. 1–25, 2021, doi: 10.3390/nano11010166.
[168] B. Shi, L. Li, A. Chen, T. C. Jen, X. Liu, and G. Shen, "Continuous Fabrication of Ti3C2Tx MXene-Based Braided Coaxial Zinc-Ion Hybrid Supercapacitors with Improved Performance," *Nano-Micro Lett.*, vol. 14, no. 1, pp. 1–10, Dec. 2022, doi: 10.1007/S40820-021-00757-6/FIGURES/5.
[169] Y. Wang *et al.*, "Scalable fabrication of polyaniline nanodots decorated MXene film electrodes enabled by viscous functional inks for high-energy-density asymmetric supercapacitors," *Chem. Eng. J.*, vol. 405, p. 126664, Feb. 2021, doi: 10.1016/J.CEJ.2020.126664.
[170] M. Boota, M. Bécuwe, and Y. Gogotsi, "Phenothiazine-MXene Aqueous Asymmetric Pseudocapacitors," *ACS Appl. Energy Mater.*, vol. 3, no. 4, pp. 3144–3149, Apr. 2020, doi: 10.1021/ACSAEM.9B02404/SUPPL_FILE/AE9B02404_SI_001.PDF.
[171] Q. X. Xia, J. Fu, J. M. Yun, R. S. Mane, and K. H. Kim, "High volumetric energy density annealed-MXene-nickel oxide/MXene asymmetric supercapacitor," *RSC Adv.*, vol. 7, no. 18, pp. 11000–11011, Feb. 2017, doi: 10.1039/C6RA27880A.
[172] J. Fu, J. Yun, S. Wu, L. Li, L. Yu, and K. H. Kim, "Architecturally Robust Graphene-Encapsulated MXene Ti2CTx@Polyaniline Composite for High-Performance Pouch-Type Asymmetric Supercapacitor," *ACS Appl. Mater. Interfaces*, vol. 10, no. 40, pp. 34212–34221, Oct. 2018, doi: 10.1021/ACSAMI.8B10195/SUPPL_FILE/AM8B10195_SI_001.PDF.
[173] L. Li, N. Zhang, M. Zhang, X. Zhang, and Z. Zhang, "Flexible Ti3C2Tx/PEDOT:PSS films with outstanding volumetric capacitance for asymmetric supercapacitors," *Dalt. Trans.*, vol. 48, no. 5, pp. 1747–1756, Jan. 2019, doi: 10.1039/C8DT04374D.
[174] Y. Wei *et al.*, "All pseudocapacitive MXene-MnO2 flexible asymmetric supercapacitor," *J. Energy Storage*, vol. 45, p. 103715, Jan. 2022, doi:

10.1016/J.EST.2021.103715.
[175] Y. Wei *et al.*, "PANI-MnO2 and Ti3C2Tx (MXene) as electrodes for high-performance flexible asymmetric supercapacitors," *Electrochim. Acta*, vol. 406, p. 139874, Feb. 2022, doi: 10.1016/J.ELECTACTA.2022.139874.
[176] R. A. Chavan *et al.*, "NiO@MXene Nanocomposite as an Anode with Enhanced Energy Density for Asymmetric Supercapacitors," *Energy and Fuels*, vol. 37, no. 6, pp. 4658–4670, Mar. 2023, doi: 10.1021/ACS.ENERGYFUELS.2C04206/SUPPL_FILE/EF2C04206_SI_001.PDF.
[177] S. Chen, X. Zhou, X. Ma, L. Li, P. Sun, and M. Zhang, "Asymmetric supercapacitors with excellent rate performance by integrating Co(OH)F nanorods and layered Ti3C2T: X paper," *RSC Adv.*, vol. 9, no. 53, pp. 30957–30963, 2019, doi: 10.1039/C9RA06393E.
[178] X. Shi *et al.*, "Highly Flexible All-Solid-State Supercapacitors Based on MXene/CNT Composites," *Energy and Fuels*, vol. 37, no. 13, pp. 9704–9712, Jul. 2023, doi: 10.1021/ACS.ENERGYFUELS.3C01420/SUPPL_FILE/EF3C01420_SI_001.PDF.
[179] H. P. Hayat, F. K. Dokan, M. S. Onses, E. Yılmaz, A. Duran, and E. Sahmetlioglu, "Flexible electrodes composed of flower-like MoS2 and MXene for supercapacitor applications," *Mater. Res. Bull.*, vol. 175, p. 112747, Jul. 2024, doi: 10.1016/J.MATERRESBULL.2024.112747.
[180] S. Suresh, V. Sindhu, M. Ramesh Aravind, A. Arundinesh, and N. Krishna Chandar, "Asymmetric pseudocapacitive electrodes for high energy density supercapacitor in aqueous electrolyte," *J. Indian Chem. Soc.*, vol. 101, no. 10, p. 101354, Oct. 2024, doi: 10.1016/J.JICS.2024.101354.
[181] K. Li *et al.*, "All-pseudocapacitive asymmetric MXene-carbon-conducting polymer supercapacitors," *Nano Energy*, vol. 75, no. February, 2020, doi: 10.1016/j.nanoen.2020.104971.
[182] Y. Li, P. Kamdem, and X. J. Jin, "Hierarchical architecture of MXene/PANI hybrid electrode for advanced asymmetric supercapacitors," *J. Alloys Compd.*, vol. 850, p. 156608, 2021, doi: 10.1016/j.jallcom.2020.156608.
[183] K. Li *et al.*, "An Ultrafast Conducting Polymer@MXene Positive Electrode with High Volumetric Capacitance for Advanced Asymmetric Supercapacitors," *Small*, vol. 16, no. 4, p. 1906851, Jan. 2020, doi: 10.1002/SMLL.201906851.
[184] C. Li *et al.*, "NiCoO2 nanosheets interlayer network connected in reduced graphene oxide and MXene for high-performance asymmetric supercapacitors," *J. Energy Storage*, vol. 49, p. 104176, 2022, doi: https://doi.org/10.1016/j.est.2022.104176.
[185] Y. Zhang, J. Cao, Z. Yuan, L. Zhao, L. Wang, and W. Han, "Assembling Co3O4 Nanoparticles into MXene with Enhanced electrochemical performance for advanced asymmetric supercapacitors," *J. Colloid Interface Sci.*, vol. 599, pp. 109–118, 2021, doi: https://doi.org/10.1016/j.jcis.2021.04.089.
[186] R. Venkatkarthick, J. Qin, and T. Maiyalagan, "Amorphous cobalt boride nanoparticles incorporated vanadium carbide MXene composite for asymmetric supercapacitor applications," *Int J Energy Res*, vol. 46, pp. 22474–22485, 2022, doi: 10.1002/er.8551.
[187] X. Li *et al.*, "All pseudocapacitive MXene-PPy//MnO2 flexible asymmetric supercapacitor," *J. Mater. Sci. Mater. Electron.*, vol. 34, no. 27, Sep. 2023, doi: 10.1007/S10854-023-11341-6.

[188] Y. Wei *et al.*, "PANI-MnO2 and Ti3C2Tx (MXene) as electrodes for high-performance flexible asymmetric supercapacitors," *Electrochim. Acta*, vol. 406, p. 139874, 2022, doi: 10.1016/j.electacta.2022.139874.
[189] G. Chen *et al.*, "Highly flexible and adhesive poly(vinyl alcohol)/poly(acrylic amide-co-2-acrylamido-2-methylpropane sulfonic acid)/glycerin hydrogel electrolyte for stretchable and resumable supercapacitor," *Chem. Eng. J.*, vol. 425, no. 2, p. 131505, 2021, doi: 10.1016/j.cej.2021.131505.
[190] F. Adams, "X-Ray Absorption and Diffraction - Overview," *Encycl. Anal. Sci. Second Ed.*, pp. 365–377, Jan. 2004, doi: 10.1016/B0-12-369397-7/00668-3.
[191] H. Khan, A. S. Yerramilli, A. D'Oliveira, T. L. Alford, D. C. Boffito, and G. S. Patience, "Experimental methods in chemical engineering: X-ray diffraction spectroscopy—XRD," *Can. J. Chem. Eng.*, vol. 98, no. 6, pp. 1255–1266, Jun. 2020, doi: 10.1002/CJCE.23747.
[192] C. E. Barn, "Session 53 Singularity Expansion Method Introduction to SEM".
[193] "IOP Conference Series: Earth and Environmental Science Review on Material Synthesis and Characterization of Sodium (Na) Super-Ionic Conductor (NASICON)", doi: 10.1088/1755-1315/140/1/012156.
[194] M. Devi and A. Kumar, "In-situ reduced graphene oxide nanosheets–polypyrrole nanotubes nanocomposites for supercapacitor applications," *Synth. Met.*, vol. 222, pp. 318–329, Dec. 2016, doi: 10.1016/J.SYNTHMET.2016.11.004.
[195] Marken, F., Neudeck, A., Bond, A.M. (2010). Cyclic Voltammetry. In: Scholz, F., *et al.* Electroanalytical Methods. Springer, Berlin, Heidelberg. https://doi.org/10.1007/978-3-642-02915-8_4
[196] F. Marken, A. Neudeck, and A. M. Bond, "Cyclic Voltammetry," *Electroanal. Methods Guid. to Exp. Appl.*, pp. 57–106, 2010, doi: 10.1007/978-3-642-02915-8_4.
[197] D. H. Evans, K. M. O'Connell, R. A. Petersen, and M. J. Kelly, "Cyclic voltammetry," *J. Chem. Educ.*, vol. 60, no. 4, pp. 290–293, 1983, doi: 10.1021/ED060P290.
[198] V. Khomenko, E. Frackowiak, and F. Béguin, "Determination of the specific capacitance of conducting polymer/nanotubes composite electrodes using different cell configurations," *Electrochim. Acta*, vol. 50, no. 12, pp. 2499–2506, Apr. 2005, doi: 10.1016/J.ELECTACTA.2004.10.078.
[199] O. E. Eleri, F. Lou, and Z. Yu, "Characterization Methods for Supercapacitors," pp. 101–128, 2022, doi: 10.1007/978-3-030-99302-3_5.
[200] N. O. Laschuk, E. B. Easton, and O. V. Zenkina, "Reducing the resistance for the use of electrochemical impedance spectroscopy analysis in materials chemistry," *RSC Adv.*, vol. 11, no. 45, pp. 27925–27936, 2021, doi: 10.1039/d1ra03785d.
[201] J. Huang, Z. Li, B. Y. Liaw, and J. Zhang, "Graphical analysis of electrochemical impedance spectroscopy data in Bode and Nyquist representations," *J. Power Sources*, vol. 309, pp. 82–98, Mar. 2016, doi: 10.1016/J.JPOWSOUR.2016.01.073.
[202] F. Lufrano and P. Staiti, "Performance improvement of Nafion based solid state electrochemical supercapacitor," *Electrochim. Acta*, vol. 49, no. 16, pp. 2683–2689, 2004, https://doi.org/10.1016/j.electacta.2004.02.021
[203] S. Zhang and N. Pan, "Supercapacitors performance evaluation," *Adv. Energy Mater.*, vol. 5, no. 6, pp. 1–19, 2015, doi: 10.1002/aenm.201401401.
[204] A. Allagui *et al.*, "Review of fractional-order electrical characterization of supercapacitors," *J. Power Sources*, vol. 400, pp. 457–467, Oct. 2018, doi:

10.1016/J.JPOWSOUR.2018.08.047.
[205] D. Peyrow Hedayati, G. Singh, M. Kucher, T. D. Keene, and R. Böhm, "Physicochemical Modeling of Electrochemical Impedance in Solid-State Supercapacitors," *Mater. 2023, Vol. 16, Page 1232*, vol. 16, no. 3, p. 1232, Jan. 2023, doi: 10.3390/MA16031232.
[206] G. Bhattacharya, A. Mathur, S. Pal, J. McLaughlin, and S. S. Roy, "Equivalent Circuit Models and Analysis of Electrochemical Impedance Spectra of Caffeine Solutions and Beverages," *Int. J. Electrochem. Sci.*, vol. 11, no. 7, pp. 6370–6386, Jul. 2016, doi: 10.20964/2016.07.86.
[207] Z. Qiao, K. Bian, C. Ding, and Y. Zhao, "Recent progress of carbon-fiber-based electrode materials for energy storage," *Diam. Relat. Mater.*, vol. 138, no. July, p. 110208, 2023, doi: 10.1016/j.diamond.2023.110208.
[208] L. Duan, Z. Ren, X. Chen, D. Zhang, and S. Xu, "FeNi Confined in N-Doped Carbon as a Highly Efficient Bi-Functional Catalyst for Rechargeable Zn–Air Batteries," *Inorganics*, vol. 11, no. 7, p. 300, 2023, doi: 10.3390/inorganics11070300.
[209] W. Wang *et al.*, "A novel exfoliation strategy to significantly boost the energy storage capability of commercial carbon cloth," *Adv. Mater.*, vol. 27, no. 23, pp. 3572–3578, 2015, doi: 10.1002/adma.201500707.
[210] Cropico, "A Guide to Low Resistance Measurement Contents," 2007.
[211] S. Srinivasa Rao *et al.*, "One-pot hydrothermal synthesis of novel Cu-MnS with PVP cabbage-like nanostructures for high-performance supercapacitors," *Energies*, vol. 11, no. 6, pp. 1–6, 2018, doi: 10.3390/en11061590.
[212] S. Palisoc, J. M. Dungo, and M. Natividad, "Low-cost supercapacitor based on multi-walled carbon nanotubes and activated carbon derived from Moringa Oleifera fruit shells," *Heliyon*, vol. 6, no. 1, Jan. 2020, doi: 10.1016/j.heliyon.2020.e03202.
[213] S. Suresh and V. Sindhu, "Enhanced gravimetric capacitance of CeO2 by compositing with the hybridized phase of MoS2," *Ionics (Kiel).*, vol. 29, no. 2, pp. 843–852, 2023, doi: 10.1007/s11581-022-04846-3.
[214] R. A. Murugesan and K. C. N. Raja, "A comparative study on the electrochemical capacitor performance of 1T/2H hybridized phase and 2H pure phase of MoS2 nanoflowers," *Nanotechnology*, vol. 33, no. 3, p. 035402, Oct. 2021, doi: 10.1088/1361-6528/AC2E24.
[215] H. Ur-Rehman, A. Shuja, M. Ali, M. S. Khan, I. Murtaza, and H. Meng, "Investigation of charge and current dynamics in PVA–KOH gel electrolyte-based supercapacitor," *J. Mater. Sci. Mater. Electron.*, vol. 33, no. 5, pp. 2322–2335, 2022, doi: 10.1007/s10854-021-07432-x.
[216] H. Ur Rehman, A. Shuja, M. Ali, I. Murtaza, and H. Meng, "Evaluation of defects and current kinetics for aging analysis of PEDOT:PSS based supercapacitors," *J. Energy Storage*, vol. 28, no. November 2019, p. 101243, 2020, doi: 10.1016/j.est.2020.101243.
[217] A. Shuja, S. Fahad, M. Ali, S. Ashraf, and I. Murtaza, "Development and performance evaluation of reduced graphene oxide based all-flexible supercapacitors with open and short circuit tests," *J. Mater. Sci. Mater. Electron.*, vol. 34, no. 32, p. 2151, Nov. 2023, doi: 10.1007/S10854-023-11479-3.
[218] M. S. Khan *et al.*, "Tailored NiO-pBOA-GNP ternary nanocomposite: Advances in flexible supercapacitors and practical applications for wearable technology and environmental monitoring," *J. Energy Storage*, vol. 86, p. 111128, May 2024, doi:

10.1016/J.EST.2024.111128.
[219] M. S. Khan *et al.*, "Energy on-the-go: V2O5-pBOA-Graphene nanocomposite for wearable supercapacitor applications," *Electrochim. Acta*, vol. 486, p. 144119, May 2024, doi: 10.1016/J.ELECTACTA.2024.144119.
[220] A. Alshanableh, B. A. Albiss, B. Aljawrneh, S. Alrousan, A. Al-Othman, and H. Megdadi, "Novel and flexible asymmetric supercapacitors based on NiCo2O4 nanosheets coated on Al and Cu tapes for wearable devices applications," *SN Appl. Sci.*, vol. 5, no. 4, pp. 1–12, Apr. 2023, doi: 10.1007/S42452-023-05341-8/FIGURES/9.
[221] M. S. Khan *et al.*, "Unveiling the electrochemical advantages of a scalable and novel aniline-derived polybenzoxazole-reduced graphene oxide composite decorated with manganese oxide nanoparticles for supercapacitor applications," *J. Energy Storage*, vol. 73, p. 109109, Dec. 2023, doi: 10.1016/J.EST.2023.109109.
[222] F. Markoulidis, A. Dawe, and C. Lekakou, "Electrochemical double-layer capacitors with lithium-ion electrolyte and electrode coatings with PEDOT:PSS binder," *J. Appl. Electrochem.*, vol. 51, no. 3, pp. 373–385, Mar. 2021, doi: 10.1007/S10800-020-01497-Y/FIGURES/8.
[223] M. Ahmad, A. Shuja, M. Ali, F. Sajid, and S. Ashraf, "Development of MXene-Enabled Titanium Carbide (TiC) Impurities-Based Electrodes for the Fabrication and Circuit-Level Testing of Gel-Based Supercapacitors," *Int. J. Energy Res.*, vol. 2024, no. 1, p. 9229089, Jan. 2024, doi: 10.1155/2024/9229089.
[224] X. Li *et al.*, "All pseudocapacitive MXene-PPy//MnO2 flexible asymmetric supercapacitor," *J. Mater. Sci. Mater. Electron.*, vol. 34, no. 27, pp. 1–12, Sep. 2023, doi: 10.1007/S10854-023-11341-6/TABLES/1.
[225] F. Liu *et al.*, "Hierarchical Porous RGO/PEDOT/PANI Hybrid for Planar/Linear Supercapacitor with Outstanding Flexibility and Stability," *Nano-Micro Lett.*, vol. 12, no. 1, pp. 1–15, Jan. 2020, doi: 10.1007/S40820-019-0342-5/FIGURES/7.
[226] R. Akhter and S. S. Maktedar, "MXenes: A comprehensive review of synthesis, properties, and progress in supercapacitor applications," *J. Mater.*, vol. 9, no. 6, pp. 1196–1241, Nov. 2023, doi: 10.1016/J.JMAT.2023.08.011.
[227] M. A. Iqbal *et al.*, "Ti3C2-MXene/Bismuth Ferrite Nanohybrids for Efficient Degradation of Organic Dyes and Colorless Pollutants," *ACS Omega*, vol. 4, no. 24, pp. 20530–20539, Dec. 2019, doi: 10.1021/acsomega.9b02359.
[228] Y. Wen, C. Ma, Z. Wei, X. Zhu, and Z. Li, "FeNC/MXene hybrid nanosheet as an efficient electrocatalyst for oxygen reduction reaction," *RSC Adv.*, vol. 9, no. 24, pp. 13424–13430, Apr. 2019, doi: 10.1039/C9RA01330J.
[229] G. Ma *et al.*, "Sulfonated polyaniline/MXene composite electrode with high cycling stability for anti-freezing flexible supercapacitor," *Chem. Eng. J.*, vol. 496, p. 153730, Sep. 2024, doi: 10.1016/J.CEJ.2024.153730.
[230] H. Xu, L. Cui, Z. Lei, M. Xu, and X. Jin, "MXene/carboxymethylcellulose-polyaniline (Ti3C2Tx/CMC-PANI) film as flexible electrode for high-performance asymmetric supercapacitors," *Electrochim. Acta*, vol. 436, p. 141408, Dec. 2022, doi: 10.1016/J.ELECTACTA.2022.141408.
[231] Y. Liu *et al.*, "Development of Graphene Oxide/Polyaniline Inks for High Performance Flexible Microsupercapacitors via Extrusion Printing," *Adv. Funct. Mater.*, vol. 28, no. 21, p. 1706592, May 2018, doi: 10.1002/ADFM.201706592.
[232] D. Jiang *et al.*, "Polyaniline-MXene-coated carbon cloth as an anode for microbial

fuel cells," *J. Solid State Electrochem.*, vol. 26, no. 11, pp. 2435–2443, Nov. 2022, doi: 10.1007/S10008-022-05255-2/TABLES/2.

[233] M. R. Thalji, G. A. M. Ali, P. Liu, Y. L. Zhong, and K. F. Chong, "W18O49 nanowires-graphene nanocomposite for asymmetric supercapacitors employing AlCl3 aqueous electrolyte," *Chem. Eng. J.*, vol. 409, p. 128216, Apr. 2021, doi: 10.1016/J.CEJ.2020.128216.

[234] H. Peng *et al.*, "A novel aqueous asymmetric supercapacitor based on petal-like cobalt selenide nanosheets and nitrogen-doped porous carbon networks electrodes," *JPS*, vol. 297, pp. 351–358, Nov. 2015, doi: 10.1016/J.JPOWSOUR.2015.08.025.

[235] Z. Li *et al.*, "Synthesis and thermal stability of two-dimensional carbide MXene Ti 3 C 2," *Mater. Sci. Eng. B*, vol. 191, pp. 33–40, 2015, doi: 10.1016/j.mseb.2014.10.009.

[236] S. Nasimul Alam, N. Sharma, L. Kumar, and S. N. Alam, "Synthesis of Graphene Oxide (GO) by Modified Hummers Method and Its Thermal Reduction to Obtain Reduced Graphene Oxide (rGO)*," *Graphene*, vol. 06, no. 01, pp. 1–18, 2017, doi: 10.4236/GRAPHENE.2017.61001.

[237] S. Sivakumar and N. A. Mala, "Synthesis and characterization of manganese doping on NiO nanoparticles and its supercapacitor applications," *Mater. Today Proc.*, vol. 49, pp. 1469–1474, Jan. 2022, doi: 10.1016/J.MATPR.2021.07.230.

[238] M. A. Rahman *et al.*, "Titanium sulfide thin film coated titanium foil for high-performance symmetric supercapacitor," *J. Energy Storage*, vol. 99, p. 113205, Oct. 2024, doi: 10.1016/J.EST.2024.113205.

[239] S. De, J. Florentino, G. Pathiraja, B. R. Gautam, and B. P. Bastakoti, "MXene/graphitic carbon nitride-supported metal selenide for all-solid-state flexible supercapacitor and oxygen evolution reaction," *J. Mater. Chem. A*, 2025, doi: 10.1039/D4TA08907C.

[240] P. E. Lokhande, V. Kadam, C. Jagtap, U. Rednam, N. Lakal, and B. A. Al-Asbahi, "Fast synthesis of Co_3O_4-MXene nanocomposites via microwave assistance for energy storage applications," *Diam. Relat. Mater.*, p. 112191, Mar. 2025, doi: 10.1016/J.DIAMOND.2025.112191.

[241] Y. Shabangoli, A. Esfandiar, M. Torkashvand, and N. Ashari Astani, "Flexible and Free-Standing MXene/Redox-Active Dye Molecules on Nanofibers for High-Performance Symmetric Supercapacitors," *ACS Appl. Energy Mater.*, Jan. 2025, doi: 10.1021/ACSAEM.4C02138/SUPPL_FILE/AE4C02138_SI_004.PDF.

[242] I. Ashraf, S. Ahmad, D. Dastan, Z. Shi, and M. Iqbal, "Delaminated titanium carbonitride MXene (d-Ti3CN) based symmetric supercapacitor (SSC) device fabrication with excellent capacitance and cyclic stability," *Inorg. Chem. Commun.*, vol. 161, p. 112059, Mar. 2024, doi: 10.1016/J.INOCHE.2024.112059.

[243] P. Lin *et al.*, "Multilayer Ti3C2Tx MXene electrode decorated with polypyridine for efficient symmetric supercapacitors," *Sustain. Energy Fuels*, vol. 8, no. 20, pp. 4873–4881, Oct. 2024, doi: 10.1039/D4SE00892H.

[244] S. Li *et al.*, "Ultra-stable sandwich shaped flexible MXene/CNT@Ni films for high performance supercapacitor," *J. Alloys Compd.*, vol. 941, p. 168963, Apr. 2023, doi: 10.1016/J.JALLCOM.2023.168963.

[245] Y. Zhang *et al.*, "Scalable assembly of polyaniline/Ti3C2Tx MXene modified cotton yarn flexible electrode for high-performance wearable energy storage," *Chem. Eng. Sci.*, vol. 305, p. 121206, Feb. 2025, doi: 10.1016/J.CES.2025.121206.

[246] Y. Zhang *et al.*, “Intercalating PANI Nanoparticles Into Ti 3 C 2 T x MXene Fiber to Construct Open Ion Diffusion Channels for High-Performance Flexible One Dimensional Supercapacitors,” *J. Appl. Polym. Sci.*, vol. 0, p. 56892, 2025, doi: 10.1002/app.56892.

[247] Y. Zhang *et al.,* “Bacterial cellulose/Ti3C2Tx MXene hybrid fiber for high-performance flexible fiber-shaped supercapacitors,” *Mater. Lett.*, vol. 394, p. 138627, Sep. 2025, doi: 10.1016/J.MATLET.2025.138627.